CHARACTERISATION OF TWO DIMENSIONAL NANOMATERIALS PRODUCED VIA SPONTANEOUS LIQUID EXFOLIATION

Kathleen Marie Cox

A thesis submitted in accordance with the requirements of the University of London for the degree of Doctor of Philosophy

July 2018

University College London (UCL)
Department of Physics and Astronomy
Gower Street WC1E 6BT

Declaration

I, Kathleen Marie Cox confirm that the work presented in this thesis is my own. Where information has been derived from other sources, I confirm that this has been indicated in the thesis.

Signature

Acknowledgements

I would like to thank my supervisors Dr. Chris Howard and Professor Neal Skipper for providing this opportunity, as well as for their support and encouragement. I would also like to thank Professor Vasiliki Tileli who has mentored me and who made my stay at EPFL in Switzerland possible, along with the financial support of the Zeno Karl Schindler Foundation.

Thanks is deserved by those who I have worked with (Kashim, Mitch, Dave, Paddy, Nadir, Elijah), those who have been friends along the way (Anna, David, Marios, Theo), as well as those who have provided technical assistance (Dr. Steve Firth, Martin Vickers, Dr. Wu Han) and those who I have been fortunate to work with through collaboration (Dr. Loren Picco, Dr. Ollie Payton, Dr. Tom Headon).

Lastly, I would like to thank my very first teachers: my mum, my dad and my sister, who have taught me the most important lessons of all.

Abstract

Developing scalable nanomaterial production methods is necessary for realising nanomaterial commercialisation. In principle, production via Liquid Phase Exfoliation satisfies this need. However, techniques reliant on energy input damage the material via mechanical stress, yielding suspensions of multi-layer stacks, stable only for days, and necessitating centrifugation for manipulation. An alternative, emerging technique relies upon the charging of material to allow spontaneous dissolution of pristine 2d nanomaterials. Here this is explored for pnictogen chalcogenide layered materials, focusing on unanswered questions relating to the practicality of the method.

In this thesis, ion intercalated Bi_2Te_3 and Sb_2Te_3 were dissolved within the aprotic solvents: N-methyl-2-pyrrolidone (NMP) and dimethylformamide (DMF). Successful exfoliation of undamaged, hexagonal 2d nanomaterials was confirmed. A range of complementary experimental techniques were used including TEM, AFM, and SAXS.

From the analysis of thousands of nanosheets it was found that gradual diffusion of nanosheets, as a result of their spontaneous exfoliation, lead to fractionation of nanosheets of differing lateral width throughout the liquid volume without need for centrifugation. Nanosheet lateral dimension was also controlled by stoichiometry of the intercalant metal, with an optimum intercalant stoichiometry of $0.1 < x < 1.5$ for $K_x.Bi_2Te_3$ for production of pristine nanomaterial.

The chemical stability of the solution was investigated in relation to exposure to air, water, and heating, with a focus on tellurium impurities. Using SEM and TEM it was shown that tellurium impurities resulted from the presence of alkali metal polytellurides, which could be minimised by optimising the $K_x.Bi_2Te_3$ stoichiometry. However, the existence of nanosheets in a 16 month old solution demonstrates stability of these liquids when handled under inert conditions.

Together these results demonstrate that this scalable method allows material manipulation and tailoring of nanosheet dimensions, whilst also giving weight to the argument that the liquids can be described as true thermodynamic solutions.

Impact Statement

There is an urgent and undeniable need to provide sustainable energy sources to address the environmental cost of fossil fuel usage. This matter is far from trivial, countering an issue as grave as fossil fuel dependency requires an entirely novel approach. Nanomaterials present a young but rapidly expanding field of research capable of innovating the world of energy generation, as well as improving energy efficiency of electronic devices. Thermoelectric 2d nanomaterials, such as Bi_2Te_3 and Sb_2Te_3, are capable of harvesting waste heat energy and converting it into useful electrical energy via the Seebeck effect. As scalable liquid-based processing of nanomaterials is crucial to the realisation of such technology, the work within this thesis focuses on the study and manipulation of Bi_2Te_3 and Sb_2Te_3 monolayers in solution. These nanomaterials are generated and stabilised through a scalable liquid exfoliation technique. This work provides a benefit to both academia, through the advancement of understanding and manipulation of these nanomaterials, and also the greater community, by addressing the key needs of industrial commercialisation so that these materials may one day be employed in electronic devices. To bring about these benefits and increase commercial activity, research within this field must continue with increased collaboration with the related industries.

Contents

List of Figures

List of Tables

Chapter 1

Introduction

'There's plenty of room at the bottom'. In 1959 the enigmatic physicist Richard Feynman gave a speech at the annual meeting of the American Physical Society where he urged scientists to explore, expose and exploit the nanometer realm [1]. Since this speech, nanoscience has become a recognised field of research with dedicated journals and has even entered the vocabulary of popular science. Whilst Richard Fenynman may have encouraged popularisation of the field, arguably, it is scientific discoveries that truly inspire scientific development. The isolation of the 2d nanomaterial graphene in 2004 by Geim and Novoselov [2] can be considered one of these ground breaking discoveries. Whilst isolation of 2d materials contradicted previous beliefs of their instability [3], therefore justifying considerable interest, it is the display of exotic physical behaviour and characteristics that promotes graphene beyond the world of esoteric science. Appropriately, the work was recognised with the award of a Nobel prize in physics in 2011 and has undoubtedly led to an increased interest in 2d nanomaterials.

However, for the gap between laboratory experiments and industrial development to be bridged, ease of manipulation of such materials must be improved. Achieving pristine nanomaterials using low cost, quick, scalable techniques would revolutionise the development of electronic device technology. In the case of thermoelectric devices, quantum confinement present in nanomaterials has been proposed for improvements in the thermoelectric figure of merit necessary for their commercial viablility [4][5]. Of those methods of nanomaterial production which show potential for industrial application, solution processing has the advantage of enabling both the method of nanomaterial isolation as well as presenting the material in a medium suitable for manipulation.

Current solution techniques fall short of this ambition and typically produce suspensions of fragmented multi-sheet stacks which are small in lateral dimension. In contrast to other published results, work conducted within our research group has shown that isolation of nanosheets from their bulk layered material is possible via a process of alkali metal intercalation and subsequent solvation in aprotic solvents [6]. This non-destructive method generates pristine 2d nanomaterial displaying the underlying hexagonal crystallographic symmetry, with high level of sheet individualisation.

This example of spontaneous dissolution of nanomaterials extends into a wider realm of interest, relating to the thermodynamic balance of both their formation and their colloidal stability. For large entities which occupy the nanoscale in at least one dimension, their shape and scale relative to the surrounding solvent requires reconciliation of both the molecular and the microscale regimes. As a result of the lack of solvent detail present in traditional colloidal DLVO theory (a theory developed by Derjaguin and Landau, Verwey and Overbeek to describe the stability of dispersions of charged colloidal particles), the applicability of this theory to nanoparticle solution systems has been called into question [7]. This work adds to this interesting and often controversial discussion, which should ultimately enrich colloidal science.

As well optimising and exploring this liquid exfoliation technique, the aim of this body of work is to produce stable solutions of pristine 2d nanomaterials from the thermoelectric materials Bi_2Te_3 and Sb_2Te_3, by using a scalable technique.

1.1 Scope of Thesis

The early work within this thesis contributed to the first published example of spontaneous liquid exfoliation of layered materials [6]. It has been demonstrated that the intercalation of alkali metals within a wide range of layered materials (such as graphite, WS_2, MoS_2, $MoSe_2$, TiS_2, FeSe, GaTe, and V_2O_5), via metal-ammonia solutions, results in a negatively charged host structure and cationic guest species which may then be exfoliated to form monolayers in aprotic solvents. Whilst this technique avoids the issues associated with other liquid phase exfoliation techniques and despite demonstrating its applicability to numerous layered materials, key fundamental questions need to be answered, both on the practicality of the method and, more widely the nature of the liquids.

This thesis explores the scalable production of two dimensional materials from pnictogen chalcogenide layered compounds which are of particular interest due to their improved thermoelectric properties. Successful exfoliation of undamaged 2d nanomaterials (Bi_2Te_3 and Sb_2Te_3) has been confirmed through the application of multiple complementary techniques. As a result of the analysis of thousands of nanosheets, a better understanding of the morphology of the nanomaterial product has been developed. An increased appreciation of the impact of material preparation methods was developed by modifying the character of the intercalated material (specifically the Metal-Bi_2Te_3 ratio) and observing the resulting nanomaterial product.

In general, the air-sensitivity of the employed methodology raises questions about the chemical stability of the nanosheet solutions. Addressing the chemical stability of these solutions is of particular importance in this work as the chemical reactivity of pnictogen chalcogenide layered compounds differs greatly from the carbon materials upon which much of the understanding of intercalation and liquid phase exfoliation is founded. Therefore, this study includes exploration of this differing chemical stability, with particular interest in the origin and prevalence of the tellurium impurities found in these solutions. This understanding informs both the practical application of these solutions as well as contributing to the understanding of the stability of nanoparticles in liquid.

This thesis will follow a clear format and it will become apparent that the solutions of 2d nanomaterials present a novel system of scientific interest as well as the answer to some of the challenges of industrialisation. Each section will now be summarised:

Chapter 2:
Background and Motivation

The necessary contextualisation of the project is provided so that the motivation of the work can be presented and discussed. This will include an introduction to two dimensional materials, as well as a discussion of the current research and methodology employed in generation of 2d nanomaterials. Their bulk analogues, the layered materials, will be discussed, with a focus on the family of pnictogen chalcogenide layered compounds due to their desirable thermoelectric properties and potential for quantum confinement. Liquid phase exfoliation of layered materials is introduced as a potential avenue for scalable production of two dimensional nanomaterials and the theories applied to the realm of particulate matter in the liquid environment will be explored.

Chapter 3:
Experimental Techniques and Theory

The details of the multi-step material production method will be provided, with emphasis on steps taken to minimise air exposure. This will be followed by an introduction to the methods used to analyse these materials, including an overview of related theory, typical application of these methods within this field of research and the sample preparation required for these techniques.

Chapter 4: Results I

The studies reported within this chapter demonstrate the successful production of hexagonal 2d nanomaterials of Bi_2Te_3 and Sb_2Te_3 as well as addressing some of the immediate questions concerning their production. Due to their spontaneous exfoliation the nanosheet solutions develop over a matter of hours, in this chapter the temporal evolution of the solutions is documented and discussed. The influence that the intercalated material has on the quality of the nanomaterial product was determined.

Chapter 5: Results II

TEM and AFM analysis of thousands of dropcast nanosheets allows a more representative description of the nanomaterial solutions to be obtained as well as gaining insight into the factors which influence the dimensions of deposited nanosheets (liquid depth; solution age; and relative concentration of alkali metal to layered material). The characterisation of nanosheets is extended from direct measurement of the deposited nanosheets to include nanosheets within the liquid environment, employing liquid TEM and SAXS for their *in situ* measurement.

Chapter 6: Results III

The reactivity and chemical stability of the nanosheet solutions is explored, determining their reaction upon exposure to air, water and prolonged heating. The origin of tellurium impurities present in the solution deposits is determined and steps are taken towards minimising the prevalence of these contaminants, which is of fundamental importance to the application of these materials.

Chapter 7: Conclusion

The experimental work will be summarised, discussed in broader terms of the nature of the liquids themselves and conclusion will be drawn from the work. This will include the discussion of the next steps to be taken within future work.

Chapter 2

Background and Motivation

The necessary contextualisation and background for this work will be covered in the following section so that the motivation of the work may be discussed. Firstly a general overview of two dimensional materials will be given, as well as a discussion of the current research and methodology employed in generation of 2d nanomaterials. Their bulk analogues, the layered materials, will be introduced, with a focus on the family of pnictogen chalcogenide layered compounds due to their desirable thermoelectric properties and potential for quantum confinement. Liquid phase exfoliation of layered materials will be introduced as a potential avenue for scalable production of two dimensional nanomaterials, intercalation chemistry will also be explained, and necessary discussion of colloidal theory will be given. Finally, the motivation of the work will be explained.

2.1 An Overview of Two Dimensional Nanomaterials

Like nanomaterials in general, two dimensional nanomaterials are attractive as they display a variety of properties which may be unavailable within the realm of bulk materials and often unique in their combination, such as high conductivity combined with optical transparency and mechanical flexibility [8][9]. This section will include discussion of their scientific interest and the array of complex engineering problems to which they are applied. It should also be noted that the method of nanomaterial production greatly impacts the possible application of the mater-

ial and so the variety of methods used to generate these materials will also be explored.

2.1.1 Interest and Application of 2d Nanomaterials

Nanomaterials are of great interest as they provide new and unexplored material properties, allowing unprecedented technological development. By reducing one of the dimensions of a particle to that within the nanoscale regime, chemical, mechanical, optical, electronic and physical properties may be altered [10]. Much of the interest in 2d nanomaterials was ignited by the isolation of graphene [2], however the discovery of inorganic 2d nanomaterials has broadened the range of available properties and therefore possible applications.

Isolation of a monolayer from a bulk layered material impacts the material properties in two distinct ways: through quantum confinement of the electron and through the large increase of surface to volume ratio. It is this large increase in accessible surface area which has lead to application of such materials to energy generation and storage, such as the use of MoS_2 for hydrogen evolution[11] [12] and Bi_2Se_3 nanomaterial for hydrogen storage [13]. Quantum confinement of the electron impacts the electronic properties of the material. For example, the increased band gap of the 2d transition metal dichalcogenides compared to their bulk layered material has lead to their application within optoelectric devices, with examples including light emitting diodes [14] and photodiodes [15]. Whereas, exotic electronic properties of Bi_2Se_3 2d nanomaterial enables its use as a transparent electrode [16].

In the case of pnictogen chalcogenide layered compounds much of the interest in their 2d analogues derives from enhancement of the desirable properties already present in the bulk materials [17][18]. For example, it has been suggested that isolation of a single monolayer would lead to a room temperature thermoelectric figure of merit ten times greater than that of the bulk material [19]. However, modelling of the isolated Bi_2Te_3 monolayer, as well as 2, 3, 4, 5, and 6 layer stacks has revealed complex variation in the band structure for these nanomaterials with decreasing number of coupled layers. Only single layer and double layer structures exhibited a band gap [20], and only the isolated monolayer had a band gap greater than the bulk material (0.27 eV compared to 0.15 eV) [21]. Therefore there is a greater variety of accessible material properties within the realm of nanomaterials, but fine control over morphology is critical in ensuring the desired

behaviour is obtained.

Whilst in some cases the nanomaterial properties simply improve upon those of existing bulk materials, their distinctly different scale also provides the opportunity for innovative device design. Improved material production methods and handling capability will enable further exploration of these layered materials and a deeper understanding and experimental confirmation of their characteristic behaviour.

2.1.2 General Methods Used to Obtain 2d Nanomaterials

Whilst encouraging an interest in nanoscience, Richard Feynmans's speech of 1959 also described nanomaterial isolation with great clarity, dividing the methods into two groups: the 'top-down' approach and the 'bottom-up' approach [1]. These two methods can be understood, respectively, as being one where a nanomaterial is isolated from within a bulk material or one where a nanomaterial is built from atomic or molecular units. Although each approach presents its own strengths and weaknesses, due to the demands of certain material applications for a specific aspect ratio, material condition and purity, it becomes apparent that in some cases one approach may be better suited than another.

Obtaining stable 2d nanosheets is a challenge that is of interest within many different fields of research and engineering disciplines. Because of the high demand for a solution to this problem, a wide variety of methods have been developed specifically to generate 2d nanosheets. Despite great innovation, there is still much progress to be made. Discussion of both top-down and bottom-up methods will contextualise the concept of scalability whilst also exemplifying the relationship between production method and application. For a truly useful 2d nanomaterial, defined by scope of applicability as well as how desirable such applications are, the method of generation must optimise both quality of product whilst also being relevant to large industrial scale generation.

2.1.2.1 'Bottom-up' Production

Two of the most common 'bottom-up' synthesis methods applied within the field of 2d nanomaterials are chemical vapour deposition (CVD) and solvothermal synthesis. The two techniques are very different from one another and demonstrate

the unfortunate compromise found within 'bottom-up' methods between cost (in both finances and time) and the quality of resulting material.

CVD uses the slow combination and chemical reaction of selected vapour on a substrate surface to produce nanosheets, large in lateral size and relatively defect free [22][15]. Whilst this fine control over material allows for the growth of nanosheets not limited to those found in a bulk layered crystalline form [23] it also demonstrates that this technique is strictly limited in production output.

On the other hand, solvothermal synthesis, which describes liquid phase chemical reactions under high temperature or pressure conditions, allows large output of material due to the synthesis routes which require little intervention and may be scaled effectively [24]. However, solvothermal synthesis routes often produce heterogeneous products and demand multiple post synthesis processing steps to separate the desired material from the other chemicals present in solution [25]. Thus nanomaterial produced via solvothermal synthesis is rarely of high enough quality for many applications.

2.1.2.2 'Top-down' Production

Of the 'top-down' methods, micro-mechanical exfoliation and liquid phase exfoliation are most commonly used. Micromechanical exfoliation describes the use of mechanical force to remove single layers, such as that used to cleave a monolayer adhered to a piece of adhesive tape. Whilst labour intensive and strictly limited in its yield, micro-mechanical exfoliation is best known for its use by Geim and Novoselov to isolate graphene and is a technique which can provide large, defect free and uncontaminated nanosheets [2][3].

In comparison, liquid phase exfoliation encompasses a broad range of techniques all of which isolate 2d nanosheets from the bulk material whilst in a solvent environment. The scope of liquid phase exfoliation is so great that it includes techniques which encompass a wide variety of physical principles, including mechanical force (sonication) [26][27][28], chemical reaction (oxdiation) [29] and steric repulsion (surfactant and polymer wrapping) [30][31][32]. Importantly, the scalable and low cost nature of these methods make the application of these nanomaterials both plausible and commercially viable. For these reasons, liquid phase exfoliation is the chosen route for 2d nanomaterial production within this work.

2.2 Layered Materials

Much of the revived interest in layered materials is related to their ability to delaminate and produce two dimensional nanomaterials via 'top-down' production methods. Therefore, understanding and appreciation of these bulk materials is necessary as they are a key 'ingredient' in this generation of 2d nanomaterials.

Layered materials are a special category of crystalline materials which comprise of two dimensional atomic sheets repeatedly stacked to form the three dimensional bulk material. In contrast to the unit cell used to describe 3d crystalline materials, these sheets may be treated individually due to the difference in bonding character within the atomic sheets compared to the bonding coupling the sheets. The interaction between these sheets is related to their charge, some layered materials have a naturally occurring net charge present on the sheets (such as clays, layered oxides and hydroxides [33][34]), but for those materials with sheets which are naturally uncharged, the layers are coupled by van der Waals bonding. This latter group of materials, referred to as 'van der Waals gap layered materials', will be the focus of this work.

Figure 2.1 gives an overview of van der Waals gap layered materials, including the variety of characteristic electronic properties which they exhibit (metallic, semimetal, insulator or semiconductor) and atomic thickness of their monolayers (1 atom, 3 atoms, 4 atoms or 5 atoms thick). The family of pnictogen chalcogenide layered materials will be explored in further detail as it includes the materials employed within this work.

2.2.1 Pnictogen Chalcogenide Layered Materials

The materials studied within this thesis are members of the family of pnictogen chalcogenide layered materials. This group of van der Waals gap layered materials may be produced through the combination of the group V elements (Bi, Sb), also known as pnictogens, and the group VI elements (S, Se, Te), also known as chalcogenides. Therefore, such materials are referred to as the pnictogen chalcogenide layered materials or sometimes, V_2VI_3 layered materials. Whilst these inorganic materials are naturally occurring, stoichiometric compounds may be prepared through heating of the constituent elements within an evacuated container at high temperatures [35].

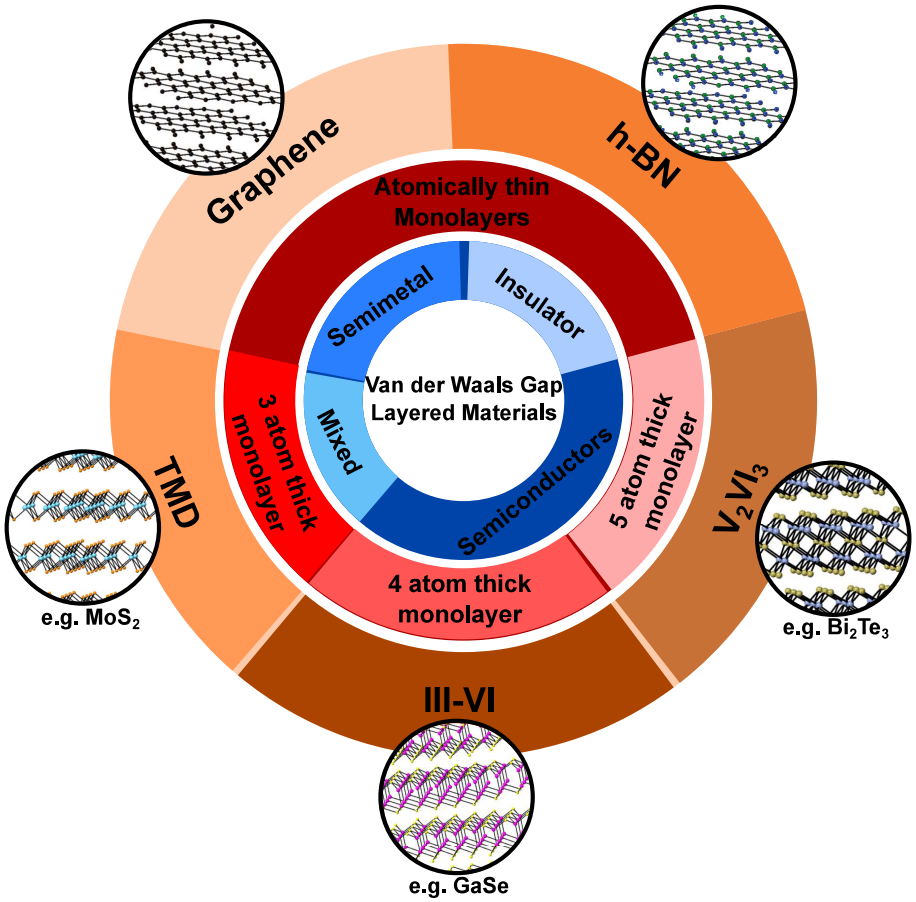

Figure 2.1: Five different van der Waals gap layered materials are given as an example and may be differentiated by the atomic thickness of their monolayers (1 atom, 3 atoms, 4 atoms or 5 atoms thick) as well as their differing electronic properties. Images shown represent the structure of each bulk layered material.

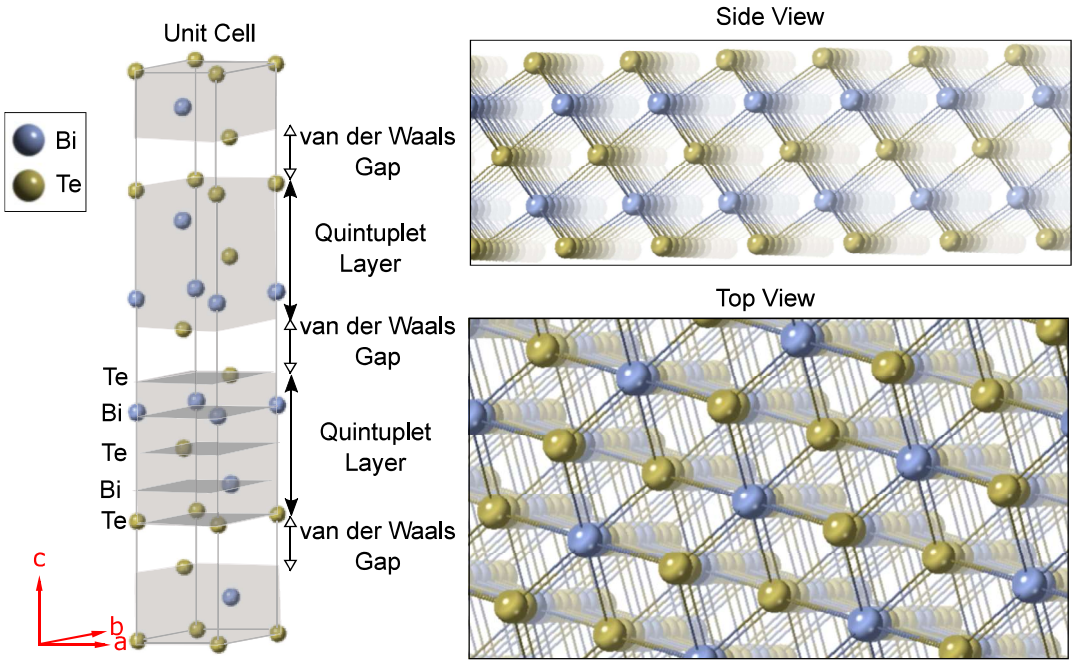

Figure 2.2: A ball and stick diagram depicting the atomic bonding found in the layered pnictogen chalcogenide compound: Bi_2Te_3. It shows the atomic arrangement in the Bi_2Te_3 unit cell, with distinct quintuplet layers separated by van der Waals gaps. The 'side view' of the quintuple layer can be seen and 'top view' of the sheet, demonstrating the symmetry of the atomic bonding within the plane.

2.2.1.1 Bulk Properties of Pnictogen Chalcogenide Layered Materials

Pnictogen chalcogenide layered materials comprise of atoms covalently bonded to form 5 atom thick sheets, known as quintuplet layers (QL), which are stacked and weakly held together by van der Waals attraction. The family of materials comprises of two isomorphic groups, those with a rhombohedral structure (Sb_2Te_3, Bi_2Se_3, Bi_2Te_3) and those with a orthorhombic structure (Sb_2S_3, Sb_2Se_3, Bi_2S_3) [36]. The nature of bonding present in the latter group creates puckered sheets which have a tendancy to break into ribbons [37] and as a result, they will not be the focus of this work.

The stacking of planar layers and atomic bonding present in the group of rhombohedral structured layered materials is further demonstrated in figure 2.2 for which Bi_2Te_3 has been selected as an example (the structure of Sb_2Te_3 is given when Bi is substituted by Sb). The unit cell in figure 2.2 is described by hexagonal axes to illustrate the layered structure with improved clarity (the volume of the primitive rhombohedral cell would be one third smaller than this hexagonal cell),

this choice of representation is possible within the rhombohedral subset of the trigonal crystal system to which these materials belong. The layered arrangement of the atoms of the pnictogen (group V) elements and chalcogenide (group VI) elements within the quintuplet layer leads to a bonding environment for the innermost chalcogenide atom, that is distinctly different in character and strength [38] from that of the outer chalcogenide atoms.

Table 2.1 provides further detail of the properties of the pnictogen chalcogenide layered materials with rhombohedral structure, space group D^5_{3d} ($R\bar{3}m$). These materials are narrow band gap semiconductors.

Material	Lattice Parameters		Band Gap / eV	Thickness of Quintuple Layer / Å
	a / Å	**c** / Å		
Sb_2Te_3	4.264	30.458 [39]	0.28 [40]	**c**/3 = 10.15
Bi_2Se_3	4.14	28.6 [41]	0.35 [41]	**c**/3 = 9.53
Bi_2Te_3	4.383	30.487 [42]	0.15 [40]	**c**/3 = 10.16

Table 2.1: A summary of the properties of the bulk pnictogen chalcogenide layered compounds with rhombohedral structure, Sb_2Te_3, Bi_2Se_3 and Bi_2Te_3. All properties were determined experimentally, references are given in square brackets.

2.2.2 Applications of Pnictogen Chalcogenide Layered Materials

Due to their desirable thermoelectric properties, one of the dominant areas of interest for pnictogen chalcogenide compounds is their application within thermoelectric devices [43]. The thermoelectric effect relates to the ability of a material to produce a potential difference from a thermal gradient and visa versa, and may be used for harvesting waste (thermal) energy or even cooling specialist equipment to prevent overheating. Such devices are particularly attractive as they lack the noise and wear associated with the moving mechanical parts common to many generators or fridges [44].

It has also been discovered that these materials are topological insulators, which means that they present a different conductivity at the material edge (metallic conductor) to that of the bulk material (insulating) due to band features, named surface states, which are present within the bulk band gap [45][46]. This property

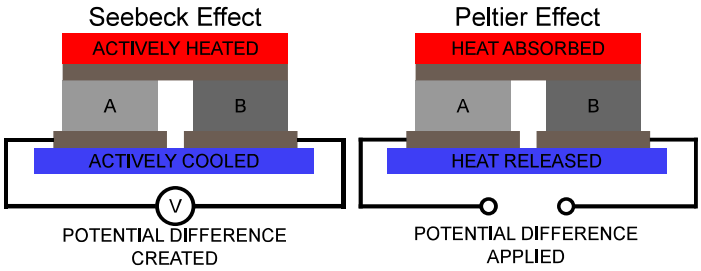

Figure 2.3: The thermoelectric phenomena: the Seebeck effect and the Peltier effect. The different materials, A and B, are connected in a circuit and are held so that they may be heated or cooled across their junctions. The seebeck effect describes the creation of a potential difference when a temperature gradient is applied across A and B. Whereas, the Peltier effect describes the temperature gradient that is created when a potential difference is applied to the circuit.

of the pnictogen chalcogenide compounds has led to their proposed usage within quantum computing [47].

The interest in the thermoelectric properties of pnictogen chalcogenide compounds, in particular Sb_2Te_3 and Bi_2Te_3, began almost 60 years ago [48]. As this property has been the driving force behind much of the research into these materials, the thermoelectric effect will be explored further.

2.2.3 The Thermoelectric Effect

The thermoelectric effect includes three phenomena: the Seebeck effect which describes the use of thermal fluctuations to generate electricity; the Peltier effect which describes the transfer of heat across two conducting materials in the presence a potential difference; and the Thomson effect which describes the resultant heating or cooling in a homogeneous conductor which has a temperature gradient existing along the direction of the current. Figure 2.3 provides further explanation of the Seebeck effect which is often used in thermoelectric generators [49] as well as thermocouples (a temperature sensor), and the Peltier effect which is used in thermoelectric cooling [50], these units can also be stacked in series to increase the ability of the generator or cooler.

When describing or comparing thermoelectric materials, it is convention to use the dimensionless quantity called the 'figure of merit'. The figure of merit, ZT, is described in equation 2.1:

$$ZT = \frac{S^2 \sigma T}{\kappa} \tag{2.1}$$

Where Z is the material coefficient, T is the absolute temperature, S is the Seebeck coefficient, κ is the thermal conductivity, and σ is the electrical conductivity specific to the material. Equation 2.2 gives the relation of the Seebeck coefficient to the change in voltage, V, and temperature, T.

$$S = -\frac{\Delta V}{\Delta T} \tag{2.2}$$

Currently, most thermoelectric materials presented in the literature have a figure of merit approximately equal to 1 at room temperature but for commercial purposes this figure of merit needs to be four times larger [5]. Considering equation 2.1 given for the figure of merit, it can be seen that for improved thermoelectric properties a material must have minimal thermal conductivity whilst maximising the electrical conductivity of the material. This task is not quite as simple as it first seems, due to the thermal conductivity having contributions from both electrical carriers and lattice vibrations (also known as phonons) [5].

2.2.4 Approaches to Improving Thermoelectric Figure of Merit

Due to the interconnectedness of the material properties which determine the thermoelectric figure of merit (ZT), increasing its value is no trivial matter, and thus multiple avenues have been explored within the literature.

Initial efforts to increase ZT of pnictogen chalcogenide layered materials included production of alloys, with n-type materials (i.e. $Bi_2Te_{3-x}Se_x$) and p-type materials (i.e. $Bi_{2-x}Sb_xTe_3$) explored [51]. Alloying is thought to decrease the thermal conductivity of the material by introducing phonon Rayleigh scattering [52] but it also increases undesirable electron scattering (to a greater effect in n-type materials than p-type materials) [48]. Whilst it may seem that alloying presents the opportunity for fine control over material properties, the reality is significantly more complex as small changes in stoichiometry can make large differences in the related thermoelectric performance leading to sometimes unpredictable and unrepeatable results.

Hope for greater improvements in ZT was ignited by a paper by Dresselhaus in 1993 [4] which hypothesised that reduction of the bulk material to the monolayer would allow for new gains in the Seebeck coefficient as well as decreasing the thermal conductivity due to phonon scattering [53][54]. In an attmept to avoid the difficulty of direct manipulation of nanomaterials, hot-pressing of milled particles

has become a popular technique. This technique is used to create nanostructured domains within bulk materials, introducing phonon scattering at the nanograin boundaries and increasing ZT to values of 1.56 at 300 K [51].

However, improved methods of nanoparticle production and manipulation have diversified the approach to accessing the benefits of quantum confinement effects in pnictogen chalcogenide layered materials. Growth of nanomaterials via solvothermal synthesis methods has been utilised, examples include Bi_2Te_3/Bi_2Se_3 heterostructure nanoflakes with $ZT = 0.71$ at 400 K [55], and Bi_2Te_3 nanosheets which had a figure of merit equal to 0.62 at 400 K [56]. 'Top-down' methods have also been employed. Examples include liquid phase exfoliation of $Bi_2Te_{2.7}Se_{0.3}$, using n-butyl lithium in hexane followed by exfoliation in water and sintering, which produced a nanostructured material with $ZT = 0.8$ at a temperature of 300 K [57]. Bi_2Te_3 nanosheets have also been exfoliated via lithium intercalation (using lithium carbonate in benzyl alcohol at 220°C), upon which researchers then grew layers of $Bi_2Te_{2.7}Se_{0.3}$ via chemical synthesis, to produce hetero-nanosheets with $ZT = 0.9$ at room temperature [58].

With these examples considered, these materials still remain far from being commercially viable as thermoelectric generators or commercially competitive as cooling devices. Vastly improved nanomaterial production methods are required before the hypothesised improvement to be made to the thermoelectric figure of merit may be realised. The scalability of these methods must also be prioritised as they also impact their possible commercial viability and application.

2.3 Liquid Phase Exfoliation of Layered Materials

Liquid Phase Exfoliation (LPE) is a 'top-down' production method applied to the delamination and isolation of 2d nanomaterials from their bulk layered materials, and with the right approach this method could be applied on the industrial scale. Many LPE techniques originate from attempts to debundle carbon nanotubes and exfoliate graphite [59], before being applied more generally to other layered materials such as transition metal dichalcogenides [26]. Such an extension is unsurprising as both nanotube bundles and certain layered materials are bound by van der Waals attraction.

Although diverse, LPE techniques have the commonality of providing both a means of overcoming van der Waals (vdW) attraction between sheets whilst also

providing a system in which the nanosheets may be stabilised. Their liquid medium also enables further manipulation of the 2d nanomaterial allowing composite generation [60][61] and novel material transfer methods such as inkjet printing and reel-to-reel production [62][63]. Although not true for every method, the scalable and low cost nature of some LPE techniques make the commercial application of these nanomaterials both plausible and viable.

Due to these reasons, liquid phase exfoliation was chosen as the nanomaterial preparation method to be applied in this work. The various LPE techniques will now be introduced (with emphasis on their differing energetics). Exfoliation methods which utilise intercalation will be explored in greater detail, before leading into the method specific to this work: spontaneous liquid phase exfolaition via alkali metal intercalation of the layered material.

2.3.1 The Energetics of LPE

A distinction may be drawn between the wide variety of liquid phase exfoliation techniques based upon energetics of exfoliation. Some methods require input of energy to overcome the van der Waals attraction between the monolayers and separate the layered material, whilst other methods modify the layered material so that exfoliation is thermodynamically favourable. Their difference in approach to exfoliation also impacts their stability against re-aggregation, as demonstrated in figure 2.4 which illustrates the main features of two LPE techniques which exhibit vastly different colloidal stability.

As a popular and dominant fixture in the LPE literature, sonication methods use ultrasound to temporarily overcome the inter-layer van der Waals (vdW) attraction and force apart layered structures [26][27][28]. Such suspensions have limited colloidal stability and require a carefully considered approach to delay the sedimentation process. Addition of surfactants to aqueous suspensions has allowed material to remain dispersed for longer (weeks), their stability dependent on steric repulsion from surfactant wrapping [31][64][65]. An alternative approach to improve colloidal stability without additional stabilisers, involves using the surface energy of the materials to inform the choice of appropriate organic solvent for these suspensions [66][67]. Whilst this ‘solvent matching’ approach increased the concentration of dispersed material, these suspensions did not exhibit a greater stability than those using surfactants and are only stable for approximately 5 days [66].

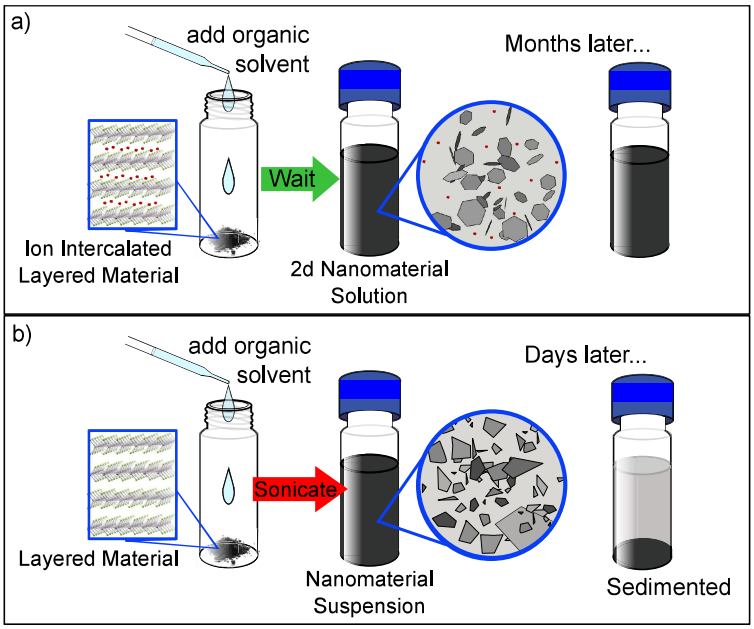

Figure 2.4: Key differences between two liquid phase exfoliation techniques. Shown in a) is the technique of exfoliating ion intercalated layered material in organic solvents, used within this work, to create solutions of pristine 2d nanomaterial which are stable for months. Shown in b) is the technique of exfoliating layered material in organic solvents using sonication to create solutions of nanomaterial (of varying size and thickness) which are stable for days.

As well exhibiting limited colloidal stability, sonication based LPE techniques damage the layered material through mechanical stress, therefore limiting the lateral size of material [68]. They also fail to provide complete sheet individualisation and instead produce a inhomogeneous, suspension of predominantly multi-layer material [64]. Although relatively straightforward to implement, this technique necessitates the use of centrifugation for material manipulation and therefore cannot be considered scalable.

Other LPE methods avoid the need of energy input by modifying the layered material to make dissolution of the layered material favourable. Typically such methods benefit from a greater degree of sheet individualisation as well as increased colloidal stability.

Graphene oxide serves as a good example of this approach. The oxidation of graphite to produce graphene oxide [69][29], not only delaminates the layered structure but changes the material properties, from hydrophobic to hydrophilic, enabling dissolution and stabilisation of the sheets in water [70] due to the introduction of new functional groups on to the sheets [71]. Whilst the chemical modification of graphene affords exfoliation and stabilisation, it also has some

undesirable effects, such as reduction in conductivity [72] and sustained defects even upon reduction [73].

Another example of this approach, involves the modification of the layered material via intercalation. This relates to the introduction of guest species between the layered sheets, with layered material remaining structurally intact. Although the nature of guest species can vary, in the case of charge transfer between guest and host, it is possible to dissolve the charged species in polar solvent, thereby exfoliating the material and stabilising against reaggregation. The technique is applicable to a wide range of layered materials [74], offers control over charging and solvation [75][76], and enables complete delamination [77]. For the specific technique applied in this work, LPE via intercalation can be both scalable and preserves the crystalline structure within the sheets [6].

2.3.2 Intercalation as an Exfoliation Route

Intercalation chemistry refers to a reaction in which a guest species inserts within a host species and can be removed in reversible way without change to the host structure. There has been extensive research into the intercalation of layered van der Waals materials [78], although these compounds present an interesting and useful field of study [79], they will be discussed here as step towards exfoliation.

Due to the capability of (charge transfer) intercalation compounds to exfoliate in polar solvents, the focus of this discussion will be on intercalation compounds with electron donor guest species. Intercalants including organic molecules [80], inorganic molecules [76], organoalkali compounds [81] and metal atoms [82] have been investigated, all of which have in common the capability of charge donation to the layered host material. However, by far the most popular choices of intercalant for the purpose of exfoliation, are organoalkali compounds and alkali metal atoms.

The organoalkali compound, n-buyllithium, acts as a Lewis base when intercalted and there are many examples of its use to produce 2d nanomaterials [81][83][84][85]. This air-sensitive technique takes days to reach completion, and requires further reaction of the intercalation compound in water to produce hydrogen, which forms between the layers and forces them apart. This suspension then undergoes ultrasonication and centrifugation to produce nanosheets. Thus this technique may not be considered a scalable method.

Whilst there is a wide variety of approaches to alkali metal intercalation, few of these methods are suited to large output production of layered materials. The use of electrochemical cell is limited to small volume production due to high resistance encountered at larger volumes [86]. The use of organic alkali salts [87], such as sodium naphthalenide, requires the use of multiple steps including the pre-expansion of the layered material using hydrazine and later sonication and centrifugation [88]. In the case of intercalation via vapour transport of alkali metal, the high temperatures restrict the method to only the most thermally stable layered materials and otherwise creates alkali chalcogenides [82][75]. Many of the aforementioned methods are followed by dispersion in water and depend on the reaction of the metal to form alkali hydroxide and H_2, forcing the material layers apart. This creates dispersions of nanosheets with limited colloidal stability and also causes damage to the sheets.

By submerging the layered material in liquid ammonia in the presence of dissolved alkali metal, known as a metal-ammonia solution, the material may be intercalated in a controlled way, whilst maintaining low temperature conditions that make it applicable for a variety of compounds [82][44]. Therefore, intercalation using metal-ammonia solutions has been chosen for the intercalation of V_2VI_3 layered compounds and it has been shown that with appropriate controls this is compatible with mass production of pristine nanosheets, with long-term stability in solution and no need for agitation [6].

2.3.3 Liquid Exfoliation of Alkali Metal Intercalation Compounds

The use of metal-ammonia solutions to intercalate a layered material so that it may be exfoliated in polar solvents, is a low-temperature and controllable technique [89][90][91][44]. As it is the method used within this thesis, it will be discussed in detail, including metal-ammonia solutions, alkali metal intercalation compounds and dissolution of these compounds in polar aprotic solvents, as each play an important role in nanomaterial production.

2.3.3.1 Metal-Ammonia Solutions

The chosen intercalation method employed within this work requires the use of metal-ammonia solutions, which depend upon the solvation of alkali ions and electrons within ammonia to create a favourable system in which ions may be ac-

cepted by the layered material. Spontaneous intercalation of alkali metal depends on the size of the ionic guest, as well as their ionisation energy (the cost of removing an electron from an atom). Intercalation occurs when the metal ionisation potential is lower than the electron affinity (the cost of adding an electron to an atom) of the host material, thus intercalation of the alkali metal involves acceptance of electron by the host material. However, the significance of ion size during intercalation is demonstrated by the difficulty in forming sodium graphite intercalation compounds, despite lithium having a larger ionisation energy than sodium, its smaller ionic radius makes its intercalation favourable (which is not true for the larger sodium ion) [92]. Metal-ammonia solutions present their own interest and complexity, further discussion of this may be found in the appendix, section 8.1.

2.3.3.2 Alkali Metal Intercalation Compounds

Although the alkali metal intercalation compounds are an intermediate product on route to the desired exfoliated nanomaterial, they deserve attention due to their strong influence on the final product [76]. The intercalated compounds present their own scientific interest, with alteration of charge carrier concentration of the layered material leading to examples of improved conductivity [93] and superconductivity [94], and as a result there is a wealth of literature concerning intercalation of layered materials.

Much of the early work within the field of layered material intercalation concerns that of graphite, with the first alkali metal graphite intercalation compound (GIC) reported in 1926 [95]. GICs have stoichiometric intercalation phases, called stages, which relate to the periodic distribution of filled and unfilled van der Waals gaps forming a superlattice structure [96][93]. The stages are assigned an index, n, which denotes the number of monolayers separating the intercalated ions. Stage 1 GIC (e.g. KC_8) are saturated and have intercalated ions present between every monolayer, so that only 1 monolayer separates the intercalants, whereas higher stages will have a greater number of unfilled graphite layers. For example, the intercalants in stage 3 GIC (e.g. KC_{36}) are distributed so that there will be three monolayers between every filled van der Waals gap. The dilation of the van der Waals gap resulting from the presence of guest species can be monitored by x-ray diffraction, with a marked difference in diffraction pattern for staged compounds [96]. The use of metal-ammonia solution to intercalate graphite leads to ternary GICs, where the intercalation of alkali metals is accompanied by the inclusion of ammonia molecules [97]. This additional guest molecule has been shown

to stabilise some of the akali metal intercalated compounds which are otherwise unachievable by other intercalation methods [98].

In contrast to the GICs, most alkali metal intercalation compounds of inorganic layered materials typically display continuous intercalation [99][74][75]. This includes transition metal dichalcogenides (TMDs), represented as A_xMX_2 (A = Li, Na, K,...; M = transition metal; X = chalcogenide), where the continuous intercalation phase with $0 \leq x \leq 1$ [100] is the principle behind application of TiS_2 as a cathode material for lithium ion batteries [101]. However, there are exceptions to this rule, with the sodium intercalation compounds of TiS_2 exhibiting staging [102], demonstrating that distinction between continuous interlcalation phase or stoichiometric phases is influenced by the host layered material as well as guest species.

Whilst there is limited published research concerning the intercalation compounds of pnictogen chalcogenide layered materials the understanding of GICs and intercalation compounds of the inorganic layered materials provides a foundation for the discussion and advancement of this field. In summary, it is important to consider that materials will present a limit to the possible intercalant concentration before reductive destruction of the layered structure occurs and intercalation may present as continuous phase or stoichiometric phase, although the factors that contribute to this distinction are complex and difficult to predict.

2.3.3.3 Dissolution of Intercalated Materials

It has been shown that charging (via metal-ammonia intercalation, as described in section 2.3.3.1) can lead to dissolution of graphite [77][89] [90] as well as fullerenes [103] and carbon nanotubes [104] in aprotic polar solvents, producing solutions of charged species which are stable against aggregation. The choice of solvent allows further control over the exfoliation process as well as resulting solution properties. The choice of solvent may be broadly separated into protic solvents, those whose molecules have labile protons (i.e. hydrogen ions), and aprotic solvents, those whose molecules do not have labile protons. By adding the intercalated material to a dry aprotic polar solvent it is possible to exfoliate individual layers and produce a solution of charged particles and alkali metal ions. Whilst this technique has been reported in the literature for production of graphene, it has not been applied without the use of sonication or stirring. We have recently demonstrated the applicability of this method to the spontaneous

exfoliation of inorganic layered materials (such as graphite, WS_2, $MoSe_2$, TiS_2, MoS_2, FeSe, Bi_2Te_3, Sb_2Te_3, GaTe and V_2O_5) [6]. However, many fundamental questions remain unanswered. As a result, this body of work is dedicated to the further investigation of these nanosheet solutions.

2.4 Particles Present in the Liquid Phase

Traditionally nanoparticles present in the liquid phase are treated like any other colloidal systems, governed by interactions as described in DLVO theory [105], and referred to as colloidal *suspensions* or *dispersions*. However, it has been argued that the assumptions present in DLVO theory, in particular the additive approach to particle interactions, are unsuitable when considering nanoparticles with a dimension which is <20 nm [7].

This body of work focuses on the presence of two dimensional nanomaterial in a solvent medium, prepared via spontaneous liquid phase exfoliation, and refers to these as *solutions*. However, this choice of nomenclature should not be taken as a statement of the complete rejection of colloidal theory. As will become evident in section 2.4.1.1, these liquids do satisfy the definition of a colloidal dispersion, but like other similar examples [106][107], they are considered thermodynamic solutions [6] unlike the meta-stable suspensions created via sonication [26]. Due to their extreme aspect ratio, these 2d particles are defined by their nanoscale dimension as well as their macroscopic dimension and therefore require an awareness of interactions on both these length scales. This is something which cannot be adequately achieved with the approach of DLVO theory alone but is a topic of considerable debate which will undoubtedly enrich colloidal science and quite possibly invigorate the field of molecular simulation. Both colloidal theory and the molecular theory of solutions are important to this work and will now be introduced.

2.4.1 Colloidal Theory

The term colloid is used to describe one phase dispersed within another and encompasses well known materials such as foams (gas dispersed in liquid), emulsions (liquid dispersed in liquid), and aerosols (liquid dispersed in gas). Of particular interest to this work is the description of colloidal dispersions, typically solid

or liquid dispersed in the liquid phase.

2.4.1.1 Defining Colloids

When defining a colloidal it is typical to define the size regime of the dispersed particles. Surprisingly even this is a contentious issue, with some defining colloidal particle dimensions within the range of 1 nm to 1 μm [108][105], whilst others are non-committal in defining the upper bound of the definition [109][110] or increase the range up to 10 μm [111]. Some colloid definitions also stipulate certain behaviours, such as Tyndall scattering or Brownian motion [108].

2.4.1.2 Describing Colloids: DLVO Theory

This introduction to colloidal theory will concentrate on the colloidal description of charged species in liquid due to the relevance it has for the work described in this thesis.

Much of the current understanding and discussion of colloids is based upon DLVO theory which was developed between the years of 1941 and 1948 by two scientific duos: Boris Derjaguin and Lev Landau, and Evert Verwey and Theodoor Overbeek [112]. This theory describes the instability of charged particles in solutions by building upon the understanding of the interactions present in these systems, as developed by Debye and Hückel [113], and Levine and Dube [114].

Figure 2.5 depicts the core concepts of DLVO theory, including the models used to describe co-ion and counter ion distribution throughout solution and the addition of repulsive and attractive interactions to describe the potential energy profile between two charged particles in solution.

The DLVO description of the ion distribution is based upon the interaction of the charged colloidal particle with the dilute electrolyte solution. The model rests upon the intuitive understanding that there will be a higher concentration of counter-ions local to the charged surface, and a lower concentration of co-ions. The distribution of ions local to the colloid causes the electrical potential to vary within the liquid medium, which is modelled using the charged double layer. The double layer contains two distinct regions referred to as the Stern layer (containing absorbed ions) and the Diffuse layer, where ion concentrations are related to the charge-dependent electrostatic interaction with the charged surface, as well

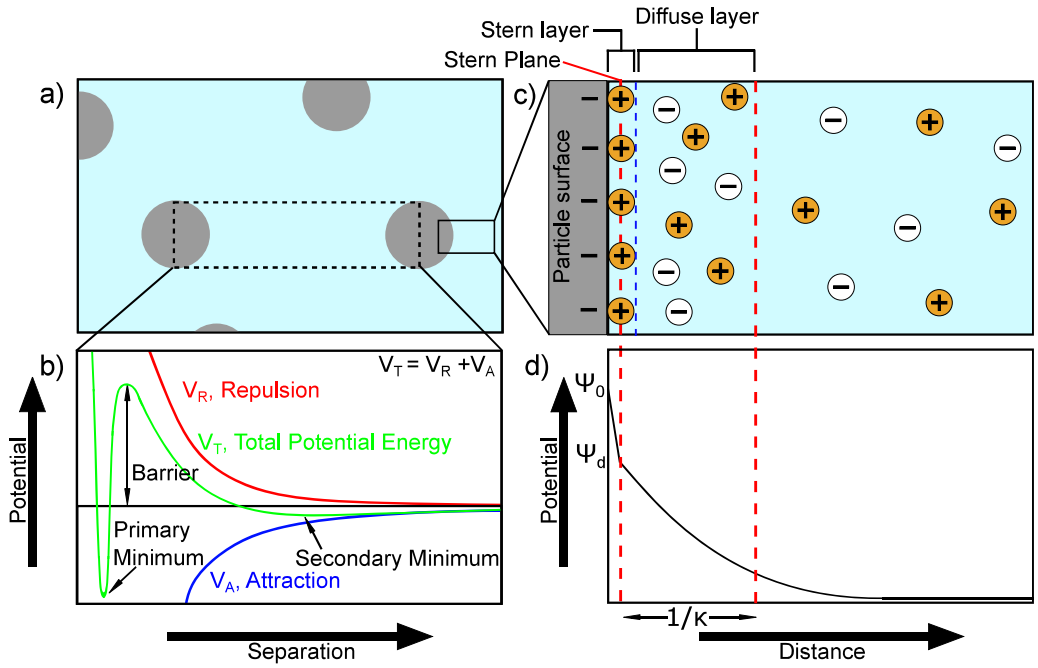

Figure 2.5: Key concepts in DLVO theory. DLVO theory describes charged particles in a colloidal suspension, as pictured in image a). Image b) is a plot of the potential energy profile between two charged particles, with the repulsive (electrostatic) potential energy, V_R, and attractive (van der Waals) potential energy, V_A, which add to give the total potential energy profile, V_T. Image c) is a diagramatic representation of the distribution of counter-ions and co-ions within the vicintiy of a charged surface in solution, which may be partitioned into the Stern layer and the Diffuse layer. Image d) plots the electric potential with increasing distance from the charged surface, Ψ_0 is the electric potential at the charged surface and Ψ_d is approximately equal to the zeta potential, ζ. The Debye length, $1/\kappa$, characterises the length scale of the diffuse layer.

as random thermal motion. DLVO theory concludes that the electrical potential is maximum at the infinite charged surface and decreases with distance from the charged surface, initially monotonically and then following an exponential decay.

The theory considers the interactions between charged colloidal particles to result from a balance between this repulsive electrostatic potential and attractive van der Waals potential [112]. The addition of the repulsive and attractive potentials give the total potential energy profile, so that the model may be used to describe the stability of a charged colloidal suspension, including phenomena such as flocculation and aggregation.

Whilst many colloidal systems are consistent with DLVO theory [115], it is unable to describe certain phenomena, such as observed colloidal stability greater than that predicted [116], and unusual nanoparticle self-assembly [117]. Like any theory, DLVO has been adapted since it was first developed [118]. However, even with the inclusion and treatment of interactions not considered in DLVO theory (hydrogen bonding, hydrophobic effect, hydration pressure, steric interactions) [119], it remains increasingly apparent that due to discreteness of nanoparticles these effects cannot always be treated separately and simply added on [7].

2.4.2 (Molecular) Theory of Solutions

Whilst is is useful to examine the reasons for which particles may be stablised or destabilised within the liquid environment it is also crucial to examine the reason for their initial dissolution. The molecular theory of solutions may be applied to describe the energetics of solvation and provides foundation for discussion of solvent detail (which is otherwise neglected in colloidal theory by treating the solvent as a continuum).

2.4.2.1 Defining Solutions

A solution is often defined as a stable single phase system, comprising of a homogeneous mixture of solute dissolved within a solvent [120]. Characteristic behaviours of solutions include the demonstration of colligative properties (such as boiling point elevation) under dilute conditions [121].

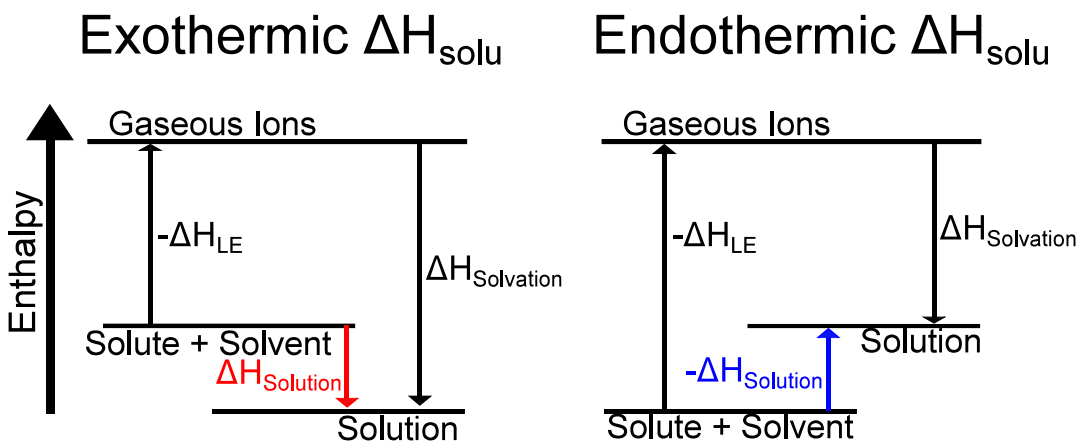

Figure 2.6: The balance of enthalpies contributing to the enthalpy of solution of an ionic species, with the distinction made between an exothermic enthalpy of solution and an endothermic enthalpy of solution. The change in enthalpy during solvation of an ionic compound depends on the interaction between the solute and solvent molecules, $\Delta H_{solvation}$ and the energetic cost of separating the ionic compound, ΔH_{LE}, known as the lattice enthalpy.

2.4.2.2 Describing Solutions: Energetics of Solvation

The energetics of solvation may be described by application of Gibbs free energy, a thermodynamic expression used to predict whether a reaction is spontaneous or not based upon the balance between two terms. As described in equation 2.3, the Gibbs free energy of solvation, G, relates to the change in enthalpy of the system, ΔH, and a second term which is comprised of the change in entropy of the system, ΔS multiplied by the temperature, T.

$$\triangle G = \Delta H - T\Delta S \tag{2.3}$$

The change in enthalpy during solvation of an ionic compound depends on whether the interaction between the solute and solvent molecules, $\Delta H_{solvation}$ (or $\Delta H_{hydration}$ for aqueous conditions), is larger or smaller in magnitude than the energetic cost of separating the ionic compound, ΔH_{LE}, known as the lattice enthalpy. Solvation is favourable enthalpically if $\Delta H_{solvation} > \Delta H_{LE}$, producing a negative value for enthalpy change (exothermic) and therefore a release of energy. Figure 2.6 demonstrates how these contributions to the enthalpy of solution, ΔH_{solu}, determine whether solution formation is an exothermic or endothermic process.

In accordance with the second law of thermodynamics, the total entropy (otherwise understood as disorder) of the universe (system and surroundings) cannot

decrease over time but when considering a system alone it is possible for a process to result in a positive or negative change in entropy. It is apparent from equation (2.3) that a reaction may still be spontaneous in the case of an endothermic reaction if the second term ($T\Delta S$) is both positive and greater in magnitude than the first term, or alternatively, a spontaneous reaction is possible despite a decrease in entropy if the reaction is also largely exothermic. The entropic change during solvation will depend upon the increase in disorder from the separation of the ordered crystalline ionic compound, but also the complex contribution relating to solvent ordering in the vicinity of the ionic species. Depending on the nature of solvent ordering around the ionic species and the ordering inherent within the bulk solvent, the introduction of the ionic species may increase or decrease the disorder of the system [122].

This understanding of thermodynamics may be applied to the spontaneous solvation of intercalated layered materials. Determining the true mechanism of dissolution in this case is difficult and controversial. In the case of the arguably more simplistic method of sonication of layered materials within aprotic solvents, attempts have been made to describe the thermodynamics of the system by discussion of surface energy of the materials in context of the Hansen solubility parameters [66]. However, this approach fails to provide much insight into the solubilty of such materials in the chosen solvents and is likely to be a result of the neglect of many other important factors.

2.4.3 Description of Low Dimensional Materials in Liquid

Despite attempts to adapt DLVO theory there are many examples of its inability to predict and explain the phenomena present for nanoparticle dispersions [116][117]. Thus it has become increasingly important to reconsider the assumptions and generalisations of colloidal theory, of which the difference in size relation between solvent molecules, ions and dispersed particles is increasingly important.

Although the same interactions are present in the case of microparticle (μP) and nanoparticle (NP) dispersions, the principle held by DLVO theory that these interactions may be treated independently and added to give the mean potential force (MPF) is appropriate in the case of μP but is often insufficient for NP dispersions. This is referred to as the additivity assumption, and the discussion and consequences of this argument have been treated within literature [7]. The

argument may be condensed to four key points (for nanoparticles <20 nm):

- solvent molecule and nanoparticle size similarity becomes significant;
- interactions cannot be treated independently (non-additivity);
- the details of the nanoparticle-solvent interface becomes significant, the solvent cannot be treated as a background continuum;
- the nanoparticle shape can be considered dynamic (with possible changes in ionic atmosphere, adsorbed molecules and dense solvation shell) and so deserves careful treatment.

Although the thorough evaluation of the applicability of colloidal theory is beyond the scope of this work, it is interesting to note experimentally observed examples supporting these key points. Of particular relevance to this study are examples of systems with regions of highly ordered solvent surrounding charged nanoparticles [103] and charged surfaces [123], espcially as in some cases these ordered regions are similar in size to the particle [124]. These suggest that stability and energetics for such nanoparticles may differ from that described in colloidal theory and demands an open minded approach to discussion of the material in this work.

2.5 Motivation

There exist numerous families of inorganic, van der Waals gap layered materials for which isolation of the monolayer may be achieved. Whilst the interest in exfoliation of such materials was stimulated by the discovery of graphene and its accompanying exotic properties, many of the 2d nanomaterials produced from inorganic layered materials exhibit vastly different properties to that of graphene and have thus greatly diversified the possible applications of 2d nanomaterials.

Although it has been known for many years that the family of pnictogen chalcogenide layered compounds, in particular Bi_2Te_3 and Sb_2Te_3, display a large thermoelectric figure of merit these materials have yet to be employed in a commercially viable thermoelectric device. The development of thermoelectric devices, for thermoelectric generation or thermoelectric cooling, has been revitalised by

the acknowledgement that nanostructures may provide new gains in the thermoelectric figure of merit. This family of layered materials still remain a focus of the efforts within this field but advancement requires mastery of methods used to obtain nanomaterials, in particular 2d nanomaterials.

Within this new wave of thermoelectric device design, strict control over morphology and purity are of particular importance as they greatly impact device efficacy. As a result the ideal method of nanomaterial generation would allow selectivity and manipulation of the nanomaterial product to meet these specific requirements. It should be noted that efficient device manufacture requires nanomaterial to be produced on an industrial scale, this scalability relies on capability to produce large volumes of material at a low cost and excludes the use of size limited techniques (such as centrifugation).

Considering these needs, the motivation of this work is the production of pristine, two dimensional thermoelectric nanomaterials through a scalable technique. The liquid phase exfoliation method utilised within this work has been chosen for its ability to generate 2d nanomaterials in a scalable way, whilst also incorporating the possibility of nanomaterial manipulation. Emphasis will be placed on the optimisation of this technique, understanding of the behaviour of the solutions produced, and exploring the limits of their chemical stability. This understanding will inform the applicability of this method to industrial scale production.

Chapter 3

Experimental Techniques and Theory

The methodology employed in this work has been be separated into material synthesis and material analysis. Firstly, the multi-step procedure used to produce the 2d nanomaterials is presented. The techniques used to analyse the material products are then introduced in context of their underlying theory and general application in the field of nanoscience, with some example data from related literature to provide context. Although these topics may be treated separately, of relevance to both aspects is the air-sensitivity of the materials being studied and attention should be paid to handling of such materials. Manipulation and storage under air-free conditions were achieved by the use of a glovebox filled with an inert argon atmosphere.

3.1 Material Synthesis Methods

The method used within this work to produce solutions of charged nanomaterials is a multi-step procedure. Each step will be described in full, including the outgassing of the purchased layered material, intercalation of the layered material and dissolution of this material, with attention given to steps taken to exclude air exposure. Figure 3.1 provides an overview of the synthesis method employed within this work, which also shows the order of the following sections.

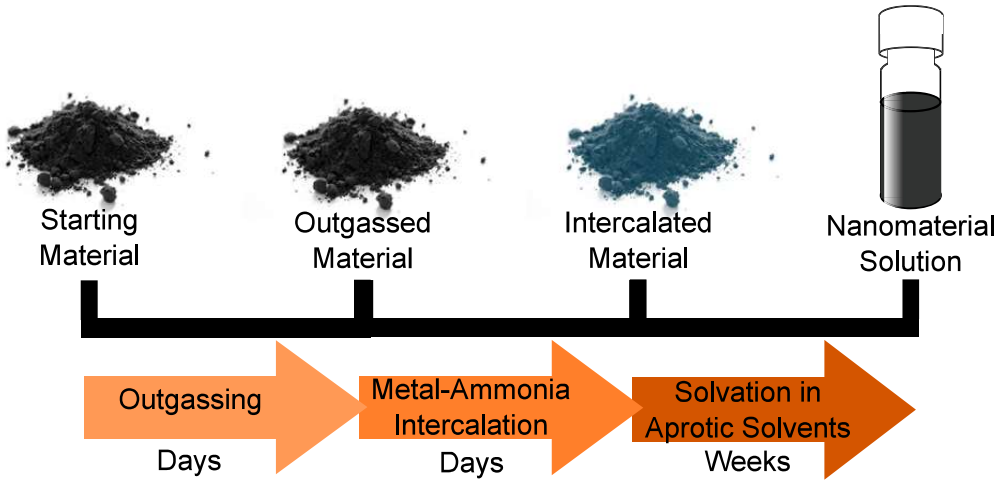

Figure 3.1: The multi-step procedure used within this work to create a nanomaterial solution from a powdered layered material, the approximate time taken for each step is shown.

3.1.1 Outgassing Layered Materials

Outgassing is a technique used to remove absorbed molecules, such as oxygen and water, from solids. In the case of this work, the technique is applied to bulk layered materials so that they are free of absorbed molecules which may lead to undesirable reactions during the intercalation process. By placing the material under a vacuum and then heating, absorbed contaminant molecules may be removed. However, it is important that temperatures do not exceed the decomposition temperature of the chosen material when under vacuum [125].

It should be noted that the layered materials were sourced commercially and their respective details listed in the table 3.1.

Name of Layered Material	Source	Product Number	Mesh Size	Purity
Bi_2Te_3	Sigma Aldrich	733482	325 mesh	99.99 %
Sb_2Te_3	Sigma Aldrich	733490	325 mesh	99.96 %

Table 3.1: The commercially sourced layered materials, their purity (based on trace metals analysis) and mesh size (for powder size exclusion) is listed as given by the supplier.

The material to be outgassed was placed within a glass sample tube with metal transition (purchased from MDC Vacuum) and then taken to a vacuum of $<10^{-6}$ mbar using a Swagelok assembly connected to a turbo vacuum pump. Whilst connected to the turbo pump, the contained sample was then placed within a tube furnace and heated steadily from room temperature to 80°C, over a period

of one hour, and then was left to outgas over a period of 48 hours (during which the pressure would stabilise at its lowest, $<10^{-6}$ mbar).

3.1.2 Intercalation Using Metal-Ammonia Solution

Liquid ammonia is able to dissolve alkali metals, producing solvated metal ions[126] and electrons which may in turn be used to intercalate layered materials[93]. However, this intercalation process must be conducted in air-free conditions with fine control over the phase behaviour of ammonia. A purpose-built apparatus was used so that gaseous, liquid and solid ammonia could be obtained whilst also maintaining a contaminant free environment by using a turbo vacuum pump to evacuate the system and then sealing. By first explaining the apparatus set-up, the processes involved in intercalation (evacuation, ammonia liquefaction, and cryo-pumping) may be understood.

A schematic representation of the purpose-built apparatus used for metal-ammonia intercalation is presented in figure 3.2. This diagram shows the canister in which ammonia is stored, the turbo vacuum pump, the sample tube with glass to metal junction and the swagelok valve assembly connecting these features. The diagram also shows the dewars in which the ammonia canister and sample tube are held, the latter of which contains an immersion cooler with immersion probe for temperature control. It should be noted that there are other necessary technical features such as a pressure transducer, pressure-release valve, ammonia source bottle and buffer canister which have been omitted from this diagram for clarity.

3.1.2.1 Ammonia Cleaning Process Prior to Intercalation

Using ammonia of high purity is crucial to obtaining a desired intercalation product of high purity. Therefore cleaning of the ammonia should be completed before embarking on the intercalation process. Cleaning of the ammonia involves creating a metal-ammonia solution and leaving the solution for 48 hours before returning the ammonia to the storage container via cryo-pumping.

Water is a common contaminant and reacts to form metal nitrites in a metal-ammonia solution. Due to the fact that the potassium nitrates are insoluble in ammonia, potassium is chosen for use in the cleaning process so that contamin-

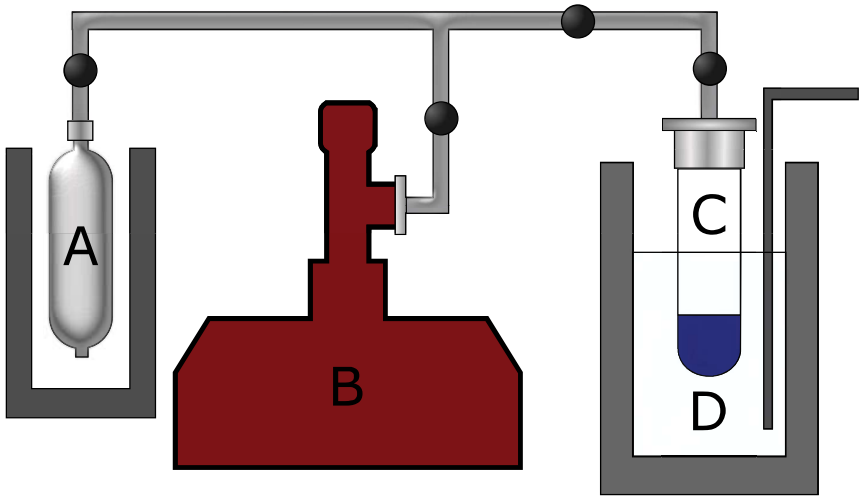

Figure 3.2: Schematic of the purpose-built apparatus used for intercalation using metal-ammonia solutions. The diagram has been labelled to show A) the ammonia cannister which is held within in a dewar, B) the turbo vacuum pump used to evacuate the system, C) the glass sample tube containing the blue metal-ammonia solution, and D) the isopropanol bath with immersion cooler used to regulate solution temperature.

ants precipitate and are removed from ammonia, thus cleaning it. Volatile gases such as hydrogen may also be produced and will be removed using a vacuum pump.

3.1.2.2 Creating a Metal-Ammonia Solution for Intercalation

Before starting the intercalation process, the layered material must be weighed and placed in the glass sample tube followed by the appropriate mass of alkali metal determined by the desired material to metal molar ratio. If the molar ratio is too low exfoliation may not occur, whereas if the molar ratio is too high then the layered material may be destroyed through reductive processes. This sample tube must be sealed using a swagelok valve assembly before being transferred from a glovebox to the apparatus and attached securely.

The sample tube is then submerged within a dewar filled with isopropanol which has been cooled to a temperature of -60°C. The main body of the apparatus is then evacuated to a pressure of $< 10^{-6}$ mbar, using the turbo pump, so that the sample is never exposed to air. Once this low pressure has been achieved the sample tube may be slowly evacuated to this pressure through opening the

sample to the system. The turbo pump may then be isolated from the system and the ammonia cannister opened slowly so that the pressure and temperature difference leads to collecting of liquid ammonia in the sample tube.

At lower concentrations, alkali metal will dissolve to give a solution of alkali metal ions and electrons in liquid ammonia, appearing deep blue in colour (as is characteristic of solvated electrons [126]). The progress of the intercalation process may be followed by the colour of the solution, with the blue colour indicating free electrons, whereas a clear and colourless solution indicates the absence of free electrons, suggesting acceptance of electrons by the layered material. Powdered samples were left to intercalate within the metal-ammonia solution until the blue colour of the electron solution was no longer visible (when intercalating a powdered sample it would take between 24 and 48 hours for the solution to appear colourless, for consistency the intercalation time was fixed at 48 hours for all samples).

Once the intercalation reaction is complete the ammonia is removed from the sample tube. The ammonia canister is submerged in a dewar filled with liquid nitrogen whilst the sample tube is removed from the cooled isopropanol bath, causing movement of ammonia to the ammonia cannister where it freezes. The sample tube containing the dried intercalated material may then be isolated, removed and returned to a glovebox. Any remaining gaseous pressure in the main system is assumed to be the result of the competing ammonia decomposition reaction which forms hydrogen. This volatile gas may be evacuated by opening the system to the turbo pump and then closing the valve to the solid ammonia. The system may then be left under these conditions with the turbo pump maintaining the contaminant free conditions.

3.1.3 Preparation of Nanomaterial Solutions

The intercalated material may then be added to a range of aprotic polar solvents, including 1-Methyl-2-pyrrolidinone (NMP), dimethylformamide (DMF), and tetrahydrofuran (THF) and left to dissolve without the need for agitation, such as sonication or stirring. Figure 3.3 includes the skeletal formula of the chosen aprotic solvents and as well as their respective product number and supplier details. Attention should be given to ensuring that the solvents used are free from water and oxygen, and that any glasswear used is clean.

Solvent Name	Solvent Structure	Supplier and Product Number
1-Methyl-2-pyrrolidinone (NMP)	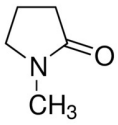	Sigma Aldrich 328634-1L
N,N-Dimethylformamide (DMF)	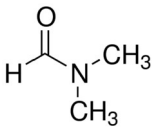	Sigma Aldrich 227056-1L
Tetrahydrofuran (THF)		Sigma Aldrich 401757-1L

Figure 3.3: The three different aprotic solvents used within this work, including their skeletal formula and supplier details.

3.1.3.1 Drying the Solvents

The commercially bought solvents (supplier details in figure 3.3) are described as anhydrous but were found by Karl Fischer titration to have a water content >60 ppm which is not dry enough for the purposes of this work. Further drying was achieved by adding zeolites (3 Å molecular sieves, Sigma Aldrich, 208582-5KG) to the solvents in mass ratio of 1:5, zeolite to solvent. The zeolites absorb the water within channels which exist in their crystalline structure but they must first have any initial water content removed, referred to as re-generation of the zeolites. The zeolites are placed in a sample tube and evacuated using a rotary oil pump, fitted with a solvent trap, whilst being heated to a temperature of 300°C for 5 days. Following this the zeolites are heated to 350°C for another two days whilst still being evacuated by the pump. Addition of the re-generated zeolites to the solvents lowers the water content of the solvents to <20 ppm over a period of 3 months. To eliminate any zeolite particulates from the solvent before use, the solvent may be passed through PTFE syringe filters (Whatman Puradisc) of pore size 0.1 μm and diameter 13 mm.

3.1.3.2 Cleaning of Glasswear

All glasswear used for preparation of the nanomaterial solutions was soaked in a nitric acid bath (7:3 volume ratio of water to 60 % nitric acid) for 3 hours, followed

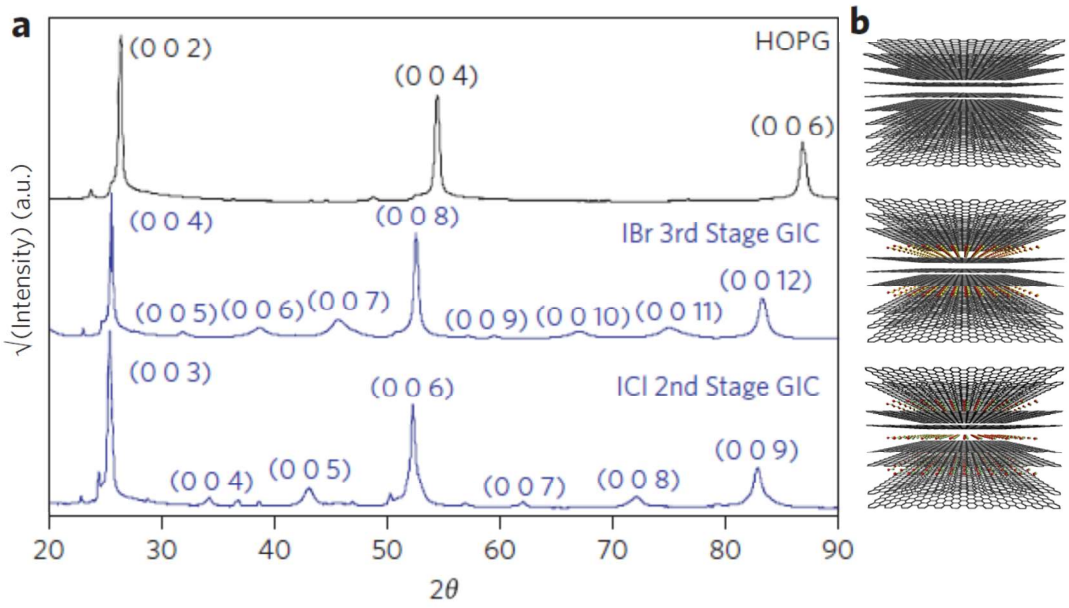

Figure 3.4: The influence of intercalation on the x-ray diffraction patterns collected from graphite intercalation compounds. The XRD patterns in a) have been collected from HOPG (highly oriented pyrolytic graphite), and two different GIC compounds: IBr Stage 3 GIC and ICl Stage 2 GIC. Molecular models are given in b), showing HOPG (top), IBr Stage 3 GIC with distinctive intercalant layer between every three graphite layers (middle), and ICl Stage 2 GIC with distinctive intercalant layer between every two graphite layers (bottom). Images modified from [76].

by a distilled water bath for 14 hours. Glasswear was then rinsed with acetone and then ethanol before being dried under a nitrogen flow.

3.2 Material Analysis Methods

A number of analytical techniques have been employed within this work to investigate the chemical character and properties of the materials used. Some methods have been used to analyse the product as well as the intermediary material. In each case, methods had to be developed to protect against air exposure of the product. Each technique will be explained, along with mention of their general application in the field of nanoscience, with some example data taken from related literature.

3.2.1 Powder X-ray Diffraction (PXRD)

The ability of the powders used within this work to accept guest molecules (i.e. intercalants such as alkali metals) and delaminate into 2d nanomaterials is related to their layered crystalline nature. Therefore understanding of a material's structural properties is critical to this work and powder x-ray diffraction (PXRD) is just one method employed in this analysis.

The importance of the technique is demonstrated by the study of graphite and graphite intercalation compounds (GIC), where their intercalation may be monitored and confirmed by XRD [96][93]. Figure 3.4 provides example of this, with the GIC x-ray diffraction patterns demonstrating the (00l) peak shifts caused by increase of interlayer spacing caused by the presence of intercalant molecules.

3.2.1.1 Underlying Theory of PXRD

Due to its short wavelength, of the order of 1 Å, x-rays are frequently used to probe the physical structure of materials. When x-rays are incident upon a material their path through the material will be determined by their interaction with the electrons within the material. Crystalline materials inherently have a periodic repetition of electron density which will create a discernible diffraction pattern, created through constructive and destructive interference of x-rays. Thus, the collected diffraction pattern contains information about the arrangement of electron density within the material.

Due to their highly ordered structure, it is useful to first consider the example of the crystalline material when understanding x-ray diffraction. Crystalline materials may be described by a unit cell, which is the smallest possible repeat unit within the crystalline structure. The unit cell contains the template for chemical composition as well as atomic placement throughout the bulk material, which in three dimensions may be described by three unit vectors, **a**, **b** and **c**. A unit cell representation may be seen in figure 3.5. Rather than describing the interaction of x-rays with each and every individual atom within the bulk material it is useful to consider scattering of radiation from diffraction planes - a construction relating to the repeat pattern defined by the unit cell. The infinite number of possible diffraction planes may be uniquely described using Miller indices, a notation written as (h k l) where their intersection of the axes within the unit cell is given by $\frac{a}{h}$, $\frac{b}{k}$ and $\frac{c}{l}$. The distance between each Miller plane is given as d_{hkl}.

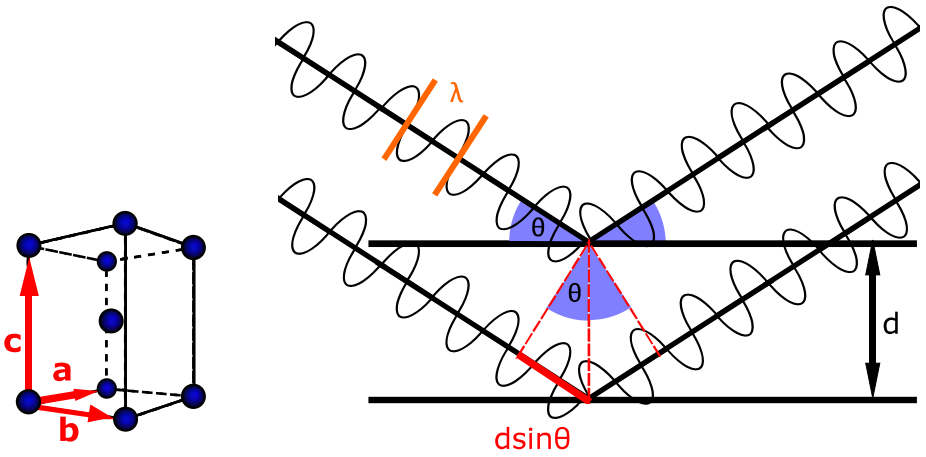

Figure 3.5: an examplar crystallographic unit cell with relating unit vectors **a**, **b** and **c** and the ray optics described by Bragg's equation. λ is the wavelength of incident light, θ is the angle of incident light upon the diffraction plane, *d* represents the spacing between diffraction planes.

Braggs Law, presented in equation 3.1, relates the observable diffraction pattern to the diffraction planes, thus allowing interpretation of experimental results and determination of material structure. λ is the wavelength of incident light, θ is the angle of incident light upon the diffraction plane, d_{hkl} represents the spacing between diffraction planes, and *n* is an integer number in the case of constructive interference.

$$n\lambda = 2d_{hkl}\sin\theta \tag{3.1}$$

The relation may be derived by using the principles of ray optics to describe the geometrical requirements for constructive interference at the detector surface, necessary for obtaining a diffraction pattern. This relationship is shown in figure 3.5. It should be noted that the experimentally collected diffraction pattern will also contain information about deviation from perfect crystallinity, such as asymmetric peak broadening as a result of stacking disorder [127].

In the case of monochromatic radiation, the observable points of constructive interference, also known as Bragg peaks, are limited by the scattering angle θ determined by the experimental set-up. To collect a useful scattering pattern a range of scattering angles must be explored. This problem can be easily solved by using powder samples. Powder samples are made of large numbers of randomly orientated crystallites, which through statistical averaging allow all crystallite ori-

entations to be explored. A common experimental set-up combines this effect with rotation of the sample during measurement.

3.2.1.2 PXRD Sample Preparation and Measurement

Due to their air-sensitive nature, sample preparation and sealing was conducted in the inert atmosphere of a glovebox. The powders were placed within borosilicate glass capillaries, O.D. 3 mm (purchased: Capillary Tube Suppliers Ltd.) and sealed with capillary wax (purchased: Hampton Research, product: HR4-328). Measurements were conducted using a Stoe Stadi-P Capillary Power XRD in transmission mode with pure $K\alpha_1$ radiation. Depending on the material, either copper or molybdenum radiation was employed to produce a scattering pattern with appreciable intensity.

3.2.2 Small Angle X-ray Scattering (SAXS)

SAXS is a x-ray technique whereby specific arrangement of the apparatus enables structures to be probed across length scales greater than the atomic crystallographic unit cell. This technique is often applied to the study of liquid phase systems, with examples including insight into the arrangement of particles in liquid crystal phases and soft matter [128].

Figure 3.6 shows a scattering profile collected from an aqueous solution of nanosheets produced from the inorganic layered material, niobate. This demonstrates the ability of scattering techniques, such as SAXS, to provide information on the structure of an individual nanosheet, stacks of nanosheets and spatial arrangement of nanosheet stacks in solution.

3.2.2.1 Underlying Theory of SAXS

X-ray scattering depends upon differences in electron density as well as the spatial arrangement of scattering objects. During SAXS only x-rays scattered at small angles ($\leq 10^{\circ}$) are collected (detector distance of 1-3 m), so that structural details on lengths scales between 1 nm and 200 nm can be probed [128].

A schematic of a typical SAXS apparatus can be seen in figure 3.7. The figure shows the direction of the incident beam, wave vector **k**, and the direction of the

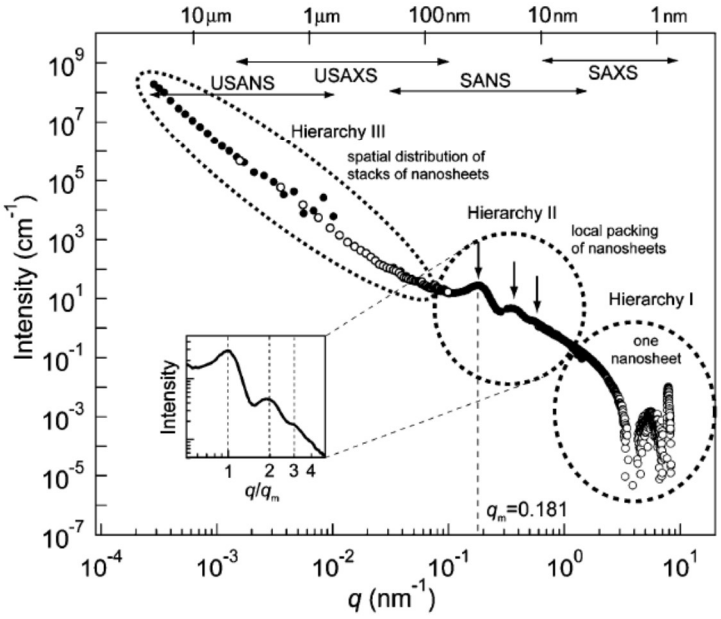

Figure 3.6: An example of a combined scattering profile of an aqueous dispersion of niobate nanohseets, reproduced from [129]. The scattering shows information for three different hierarchies: the single nanosheet, the stacked nanosheets and the arrangemnt of stacks of nanosheets within space.

scattered beam, wave vector **k'**, related by the scattering angle, 2θ, and their relationship to the scattering vector, **Q**. It is reasonable to assume that at small scattering angles all detected scattering is elastic and that incoherent scattering is negligible[130]. This allows **Q** to be described in terms of the wavelength of incident radiation, λ and and the angle of incidence between the light and the scattering plane, θ, as given in equation 3.2:

$$Q = k' - k = \frac{4\pi\sin\theta}{\lambda} \tag{3.2}$$

The intensity pattern, *I(Q)*, formed at the detector surface is related to the sample properties, as given in equation 3.4. The relationship includes the following variables: the number of particles, N_P, volume of each particle, V_P, scattering length density of the particles and the solvent, ρ_P and ρ_S, the form factor relating to particle shape, *F(Q)*, the structure factor which is dependent upon the interactions between particles and their resultant arrangement, *S(Q)*, and background scattering, *B*.

$$I(Q) = N_P V_P^2 (\rho_P - \rho_S)^2 F(Q) S(Q) + B \tag{3.3}$$

Due to the numerous contributions to the intensity of scattered radiation, mod-

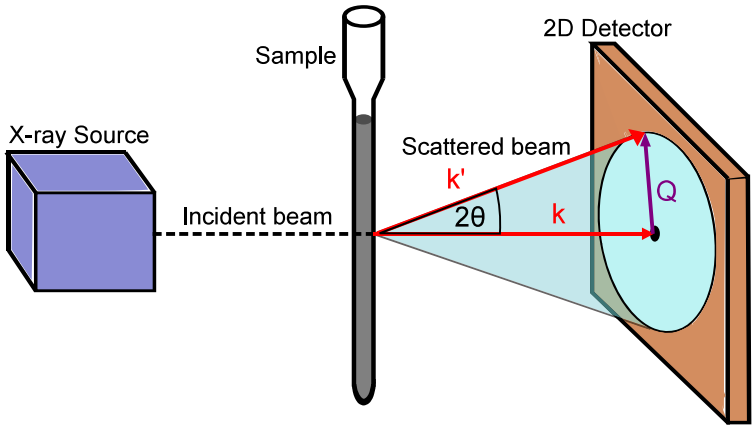

Figure 3.7: The basic principles of small angle scattering techniques. The incident beam, k, is created at the X-ray source and directed at the sample. The 2D detector then intercepts the scattered beam, k', with the relation of the incident and scattered beam describing the scattering vector, Q, and the scattering angle, 2θ.

elling of SAXS intensity data is a complex task and it is useful to have a another method of assessing the scattering data before undertaking modelling. It is possible to obtain an approximate description of the scattering particles and their arrangement in space by evaluating the gradient of the scattering data in a log[I(Q)] vs. log(Q) plot. For low to mid-range *Q* values *I(Q)* is dominated by structure factor, *S(Q)*, which can be approximated by a power law decay, as shown in equation 3.4, with an exponent given by the fractal dimension, D_f [131].

$$S(Q) \sim Q^{-D_f} \tag{3.4}$$

The gradient of the line in a log-log plot will be equal to the fractal dimension which may be used as an approximate indication of different scattering systems, as listed in table 3.2. This technique is useful for rapid assessment of the scattering data and may be used to inform adjustment whilst conducting a SAXS experiment as well as gaining a superficial idea of the scattering data before completing modelling.

3.2.2.2 SAXS Sample Preparation and Measurement

Due to their air-sensitive nature, sample preparation was conducted in the inert atmosphere of a glovebox. Samples were prepared by placing a weighed mass of intercalated powder, followed by addition of solvent using a glass syringe and metal needle, into borosilicate glass capillaries, O.D. 1.0 mm (purchased:

System	D_f
Rod-like chains, filaments	1.00
2d networks	1.90
Lamellae, platelets, discs	2.00
Weakly segregated 3d networks	2.50
Volume fractals	3.00
Bodies with rough interfaces	3.00 - 4.00
Surface fractals, bodies with sharp interfaces, spheres, strongly segregated networks	4.00

Table 3.2: Relating the fractal dimension, D_f, to the system of scatterers. Reproduced from [132].

Capillary Tube Suppliers Ltd.). The capillaries were lightly tapped to encourage the flow of solvent to the bottom of the capillary. For each intercalated powder, two different samples were prepared, a high concentration (0.0040 g intercalated powder, 0.06 mL NMP) sample and a low concentration (0.0015 g intercalated powder, 0.06 mL NMP) sample. The capillaries were sealed with capillary wax (purchased: Hampton Research, product: HR4-328) and samples were left for 5 days before SAXS measurement.

Scattering measurements were completed on the Xenocs Nano-inXider, with Cu - Kα radiation. Unlike typical SAXS apparatus, the incident beam runs in the vertical with capillary samples held in a horizontal position. Scattering measurements were conducted across the Q range of 0.005-0.5 $Å^{-1}$ for a duration of 1800 s, with 5 repeat measurements per sample. Removal of background scattering was completed by subtracting the scattering measured for the pure solvent sample. Scattering data was modelled using SasView 4.2.1 which is a freely available software made for this purpose, containing preprogrammed model systems.

3.2.3 Transmission Electron Microscopy (TEM)

There are many types of electron microscopes, each with different capabilities, sample preparation and suitable application. The transmission electron microscope enables visualisation of nanometre sized structures but requires that samples are thin enough for sufficient transmission of the incident electrons. TEM is ubiquitous in the analysis of nanoparticle suspensions, figure 3.8 presents TEM images typical of those found in literature related to liquid phase exfoliation.

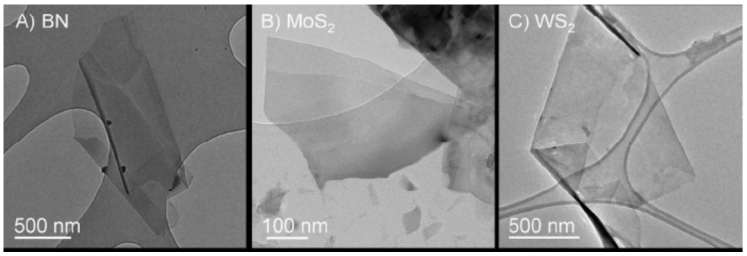

Figure 3.8: Example TEM images of single BN, MoS_2 and WS_2 nanosheets produced via a sonication based method of liquid phase exfoliation of bulk layered materials, reproduced from [133].

3.2.3.1 Underlying Theory of TEM

As with many technological advances, the development of the transmission electron microscope (TEM) in 1938 by Ernst Ruska [134] was the response to the limitations of the technology of the time, namely the optical microscope. Whilst an optical microscope may resolve features on the micrometer scale, the TEM has a far greater resolving power, with most machines achieving nanometer resolution and more complex designs achieving picometer resolution [135].

The de Broglie wavelength equation, equation 3.5, demonstrates that physical matter, such as electrons, may be used as the radiation within a microscope and presents a solution to the wavelength dependent resolution limit of the optical microscope. As shown, the associated wavelength, λ, may be be calculated for a particle with momentum, p, by application of planks constant, h.

$$\lambda = \frac{h}{p} \tag{3.5}$$

TEM is a form of electron microscope that operates in transmission mode and may be considered analogous to the compound optical microscope. This similarity in operational design is demonstrated in figure 3.9 which shows that both microscopes comprise of an illumination source, a lens arrangement to collimate the beam (condenser), a lens arrangement to magnify the beam and a final lens arrangement to project the image onto a screen. In contrast to the optical lens which relies on refraction due to differences in refractive index, the lenses within the TEM are electromagnetic lenses which create an electromagnetic field to influence the path of the electrons. The design of the lens is such that the field generated is present across a small area and therefore acts as a converging lens with a strength which can be adjusted by varying the current. There are also

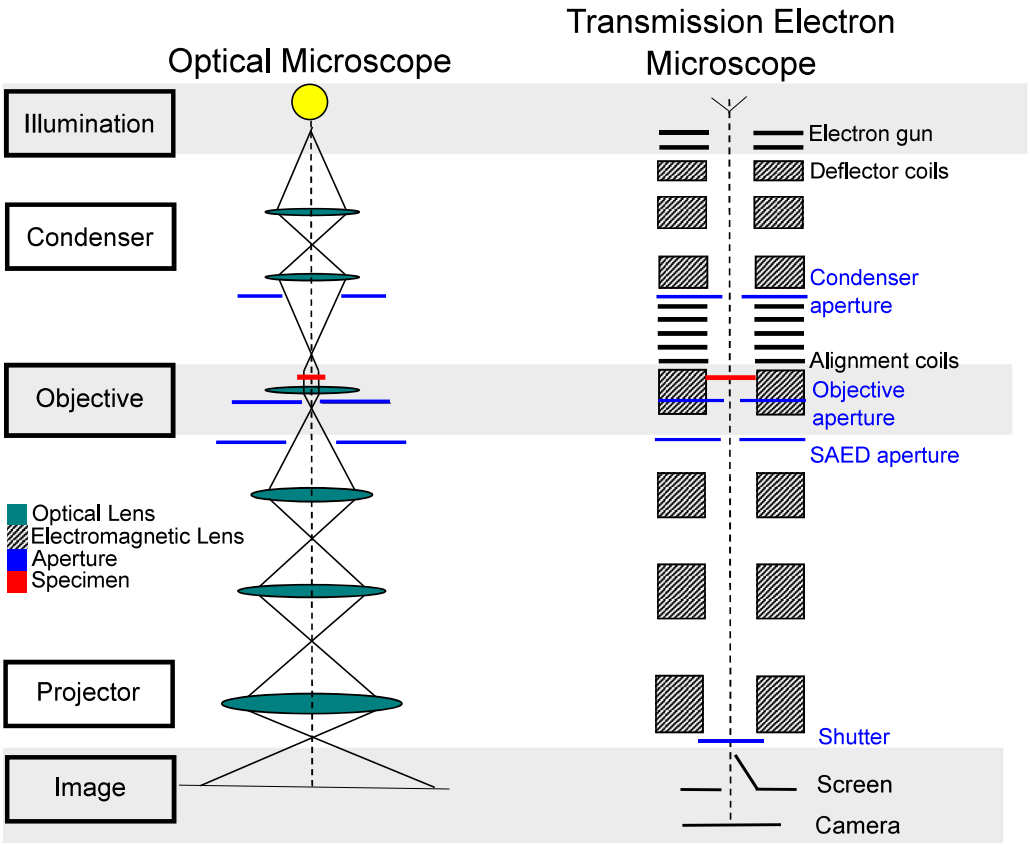

Figure 3.9: Comparing the transmission electron microscope (TEM) with the compound optical microscope. Although a TEM comprises of electromagnetic lenses, both microscopes consist of an illumination source, condesnser lens system, objective lens system, and projector system which creates the final image.

systems within the TEM which act to aid beam alignment and image focusing, including electromagnetic coils and apertures.

In TEM the sample composition determines how the electron beam is scattered, with the atomic mass (equivalent to chemical composition), thickness and crystallinity impacting the scattering behaviour. As well as imaging mode, the TEM may be used to collect an electron diffraction pattern from a selected area of the sample (SAED, selected area electron diffraction) and it is common for modern microscopes to have additional detectors built-in, such as EDX (energy dispersive x-ray spectroscopy) which allows elemental analysis. In the event of ejection of core electrons from a sample due to incident high energy electron beam, the characteristic x-rays emitted following the relaxation of outer shell electrons may be detected and used to chemically identify the sample. This is the underlying principle of EDX.

3.2.3.2 Liquid TEM

Development of the TEM has seen sample preparation, at first limited to dropcast particles on carbon films or < 1 μm thick slices of bulk samples, expanded to include imaging of liquid samples. This mode of TEM operation to include liquid samples is called Liquid TEM. Liquid samples must be encapsulated in microfabricated cells with an electron transparent, silicon nitride window because of the necessity of maintaining high vacuum for the performance of the TEM [136].

This type of liquid TEM cell has been applied to *in situ* observation and investigation of biological matter, whereby biological cells remain alive even in the presence of the electron beam [137]. Although atomic resolution has been achieved for liquid TEM study of platinum nanocrystals [138] this requires strict operation conditions and in general the image resolution achieved within liquid TEM is lower than that of conventional TEM.

The main contributing factor to the resolution limit of the liquid TEM is chromatic aberration [139], which, although present in all TEMs, is greatly affected by the presence of the liquid which broadens the energy range of transmitted electrons and leads to a 'blurry' image. Microscope operation is also complicated by interaction between the liquid medium and the electron beam leading to unknown heating, charging effects and possible sample damage, as well as Brownian motion. Thus it is critical to minimise the beam current during liquid TEM experiments, which in turn leads to the limitation of the image resolution.

3.2.3.3 TEM Sample Preparation and Measurement

TEM samples were prepared by dropcasting 0.8 μL of the solution sample onto 400 mesh, gold grids covered with holey carbon film or complete carbon film (purchased from Agar Scientific or EM Resolutions). These samples were then dried at 80 °C for 10 minutes, whilst held on a glass slide above a hot plate , with all preparation conducted within the inert atmosphere of an argon filled glovebox.

Measurements were conducted using a Jeol JEM-2100 equipped with a LaB_6 source operated at 200 kV. Although the measurement is conducted within a vacuum system, the samples were exposed to air for a number of minutes when being transferred to the TEM (although this was limited as much as possible).

In the case of liquid TEM studies, 100 μL of the prepared solution was intro-

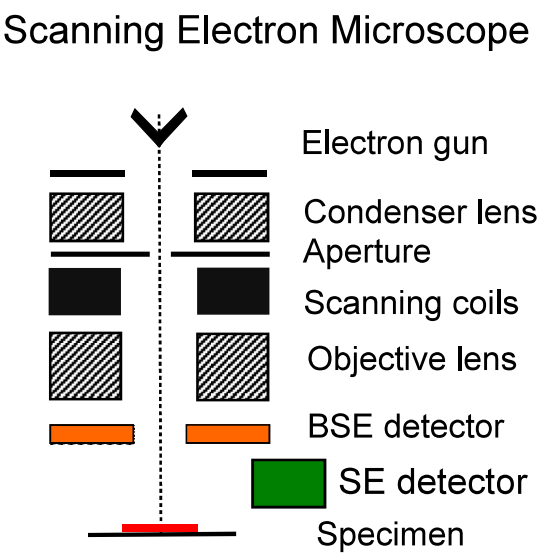

Figure 3.10: The scanning electron microscope (SEM) comprises of an illumination source (electron gun), electromagnetic condesnser lens system, objective lens system, and two detector systems: back scattered electron (BSE) detector and secondary electron (SE) detector which allows the surface of the sample specimen to be imaged.

duced into the liquid flow TEM holder (Hummingbird Scientific) via plastic tubes, and a hand-operated syringe. Studies were conducted using a JEOL JEM-2200FS.

3.2.4 Scanning Electron Microscopy (SEM)

Another form of Electron Microscope, the scanning electron microscope (SEM) uses a focused electron beam (in vacuum) which is scanned over the area of interest to build an image of the surface topography of conductive materials. Figure 3.10 shows a schematic of the main components found within an SEM. In the case of non-conducting materials, gold may be layered onto the surface of the material sample via plasma sputter coating.

Unlike the transmission electron microscope, only the electrons reflected from the sample surface are collected and so only the exposed surface of the material may be studied using this technique. Thus SEM is typically employed in the study of material roughness, topography and particle size and shape. It is a popular technique in the development of microscale semiconductor electronic devices, with typical resolution of 1 nm.

Although there are multiple possible SEM imaging modes (and detectors) this work will focus on secondary electron imaging (SEI). Secondary electrons are

produced from inelastic scattering following irradiation of the sample with the electron beam. The exit depth of secondary electrons is small and so only information about the surface or near-surface regions is given by SEI, with image contrast relating primarily to the surface topography. For example, fewer electrons can escape to the point of detection from flat surfaces compared to rough areas, so that ridges appear brighter in an SEI SEM image, this is referred to as the edge-effect.

3.2.4.1 SEM Sample Preparation and Measurement

To prepare an SEM sample a (1 cm x 1 cm) aluminium sheet square was heated to 120°C and coated with a layer of specialist thermoplastic adhesive, TEMPFIX (produced by: Plano GMBH). After cooling, the sheet with TEMPFIX coating was heated to 40°C and the powder of interest was dusted onto the tacky embedding medium. The fixative, designed for the purpose of SEM sample preparation, had the benefit of adhesion at the low temperature of 40°C and was a favourable alternative to solvent based glues, which were avoided due to possible reaction with the intercalated materials. Before measurement the samples were given a thin conductive coating by using a Au plasma coating technique for 1 min 30 s. All samples were prepared in the inert atmosphere of an argon glovebox.

Measurements were conducted using a Jeol JSM-6701F SEM (field emission) operated at 10kV probe voltage, with secondary electron imaging. Although the measurement is conducted within a vacuum system, the samples were exposed to air for a number of minutes when being transferred to the SEM (although this was limited as much as possible).

3.2.5 Atomic Force Microscopy (AFM)

Atomic Force microscopy (AFM) is another technique, ubiquitous within nanoscience, which surpasses the imaging resolution of the traditional optical microscope. AFM is a specific type of scanning probe microscope, invented by Binnig, Gerber and Quate in 1986 [140]. AFM has since developed into a technique which may be used to image surfaces with subnanometer resolution, manipulate surface features via nanolithography [141] and measure interactions between probe and surface in ambient conditions. Crucially, AFM is able to image the physical surface topology of a sample enabling the determination of sample dimensions, the necessary defining feature of nanomaterials. Figure 3.11 presents AFM images

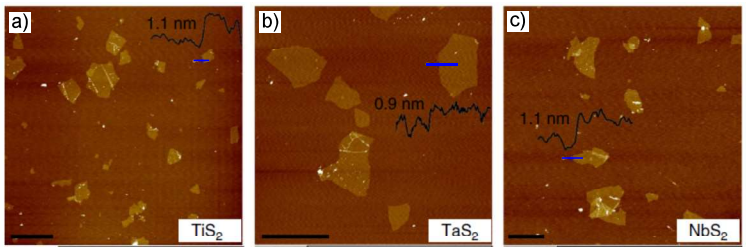

Figure 3.11: Example AFM height images of single a) TiS_2, b) TaS_2 and c) NbS_2 nanosheets produced via a sodium naphthalenide method of liquid phase exfoliation of bulk layered materials, reproduced from [88].

typical of those found in literature related to liquid phase exfoliation.

3.2.5.1 Underlying Theory of AFM

The function and capabilities of an AFM may be understood by first considering its constituent components: probe, movement system and detection system.

The probe which contacts the sample surface consists of a flexible cantilever with atomically sharp tip, which is able to apply force to the surface as well as alter its movement in response to the surface environment. The system controlling movement of the probe relative to the sample consists of piezoelectric motors which allow for fine control and fast response. There are also different modes of probe movement, contact mode or intermittent contact mode (tapping mode), the latter is commonly used for imaging nanomaterials and samples in ambient or liquid conditions.

The movement of the cantilever in response to contact with the sample surface may be detected by reflecting a laser off the cantilever surface. This reflected light is collected and converted to an electrical signal using a segmented photodiode detector. The combination of these components enable the formation of a topographical image of the material surface. However, the operation of the AFM also relies upon a feedback loop, monitoring the detected signal to adjust the input signal, which allows fast scanning of the surface whilst minimising catastrophic tip-sample collision.

Within this work, AFM measurements were conducted in tapping mode where cantilevers are designed to oscillate at near their resonant frequency. The intermittent contact of the tip with the sample surface affects the frequency of oscillation of the cantilever and its phase shift relative to driving oscillator. These

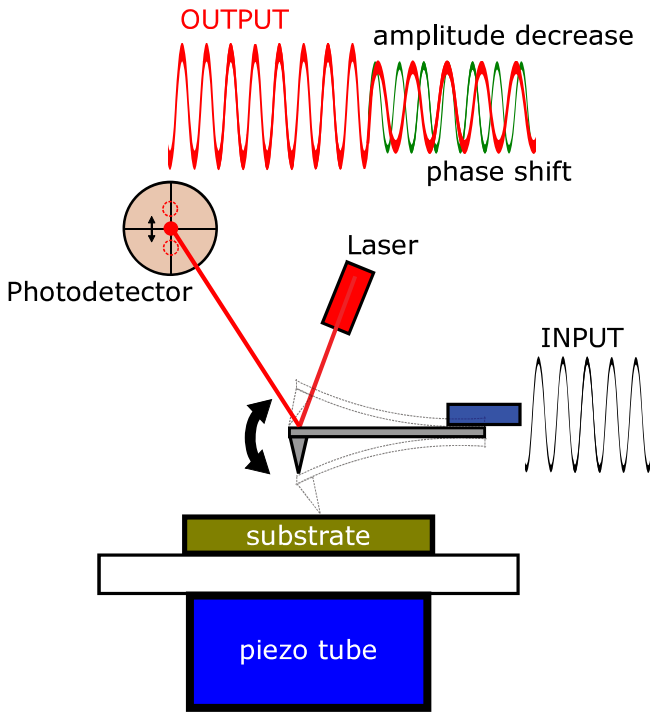

Figure 3.12: The principles of tapping mode AFM. During measurment the AFM tip rasters across the sample surface. Laser light is reflected off the oscillating AFM cantilever and collected at the segmented photodiode detector. This output signal, with any change in amplitude or phase shift, is related to the topography and viscoelastic properties of the features present on the substrate.

measurable changes allow both a height image (topographical representation of the surface) and a phase image (map of approximate chemical composition of the surface) to be constructed during the raster scan across the surface. Figure 3.12 provides a simplified representation of the features of tapping mode AFM.

3.2.5.2 AFM Sample Preparation and Measurement

The AFM samples were prepared by applying a 1.5 µL droplet of the chosen solution to a recently cleaved mica square (1 cm x 1 cm area, purchased from Agar Scientific), which was then dried on a hotplate at 80°C for 10 minutes. All sample preparation, including cleaving the mica, was conducted in the inert atmosphere of an argon filled glovebox. However, it should be noted that measurements were conducted under ambient conditions. Air exposure was minimised by ensuring all samples were prepared on the morning of the experiment and only removed from the glovebox immediately before measurement.

Measurements were conducted on a Bruker Dimension 3100 AFM, in tapping

mode, using PPP-NHC tapping mode cantilevers. Image analysis was completed using Nanoscope software (Bruker) and Gwyddion software (which is freely available).

3.2.6 Ultraviolet-Visible Absorption Spectroscopy (UV-Vis)

Ultraviolet-Visible Absorption Spectroscopy (UV-Vis) is an analytical technique used to characterise molecules in solution. During normal operation, the sample is irradiated with light within the ultraviolet (380 - 100 nm) and visible (750 - 380 nm) region, the light transmitted through the sample is then collected and an absorption spectra created. The absorption spectra is determined by the absorption of photons which promote electronic transitions within the chemical species present within the sample (although vibrational and rotational energy levels may also influence the spectra to a lesser degree).

UV-Vis spectroscopy can be described mathematically by considering the difference in intensity of radiation entering the sample and the radiation leaving the sample. The intensity of the incident radiation, I_0, is altered by its path of travel, of length L, through the sample and results in emergent light of intensity, I. As given in equation 3.6, the change in light intensity after passing through the sample can be described by the absorbance, A:

$$A = \log(\frac{I_0}{I}) \tag{3.6}$$

Absorbance increases linearly with the increase in path length, as described by the Beer-Lambert law given in equation 3.7, where C is the concentration of absorbing species and ε is the molar absorptivity (a material specific value, with units: mol dm^{-3}).

$$A = \varepsilon CL \tag{3.7}$$

Absorptivity is empirically determined through creation of a calibration curve from samples of known concentration. However, there is deviation from non-linearity experienced at higher sample concentrations [142] and the interpretation of spectra is complicated by sample polydispersity [143]. Whilst information has been derived from the UV-Vis absorption spectra of sonication exfoliated layered materials [144][145], this required special apparatus (an adapted integrating sphere) to record and remove the significant contribution from particle scattering, as well particle size selection via centrifugation, before quantitative interpretation could

be achieved.

3.2.6.1 UV-Vis Sample Preparation and Measurement

Measurements were conducted using the Perkin Elmer Lambda 950 UV-Vis Spectrophotometer (fitted with a tungsten-halogen lamp and a deuterium lamp). Solutions were decanted into square quartz cuvettes with screw top lids (Hellma Analytics, Product number: 117-100-10-40) with path length 10 mm. All sample preparation was conducted in the inert atmosphere of the glovebox, cuvette lids were wrapped with parafilm to minimise air-exposure during measurement and were transported to the apparatus in sealed plastic boxes. Prior to use, all cuvettes were cleaned using decon90, (an alkaline surfactant solution available from decon), followed by washings with deionised water, ethanol, and acetone. The absorption spectra of a cuvette containing pure solvent (NMP or DMF) was recorded and used for background subtraction during analysis of collected spectra.

3.2.7 Dynamic Light Scattering (DLS) and Zeta Potential Measurement

The movement of colloidal particles within liquid is linked to their size, and in the case where an electric field is applied, their movement will also be impacted by particle charge. By determining particle velocity, which may be achieved by observing the interaction between the particles and incident light, both the particle size and zeta potential may be measured.

Dynamic Light Scattering (DLS) is used to measure the size distribution of particles within the liquid environment. Whereas the zeta potential is a description of the charged nature of a solution and is typically employed to describe colloidal dispersions and their colloidal stability. The discussion of the two techniques has been combined due to the determination of particle velocity being necessary to both measurements and measurement being completed using the same machine.

3.2.7.1 Underlying Theory of DLS

Colloidal particles within a solution will exhibit Brownian motion, where their path within a liquid is affected by their random collision with surrounding molecules.

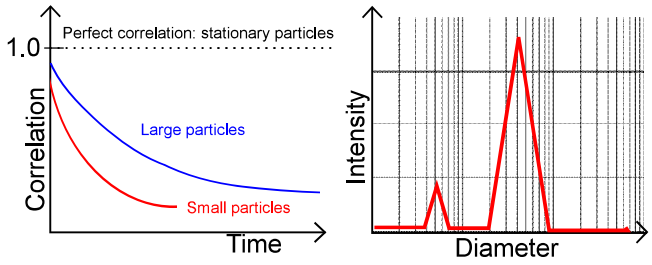

Figure 3.13: The first plot in the figure shows the correlation of light, scattered from moving particles, as a function of time. The correlation function decays quickly for small particles and slowly for larger particles, which is the basis of size determination in DLS (dynamic light scattering). An example plot of a size distribution by intensity generated by DLS demonstrates how larger particles scatter more light and thus produce a greater signal, although this does not represent the true particle numbers.

The velocity of particle movement is inversely related to their size as given by the Stokes-Einstein relation [110], so that larger particles move slower than smaller particles. By illuminating a colloidal suspension with laser light and monitoring the scattering of the light, the movement of particles may be indirectly studied and the size distribution of the particles calculated.

Dynamic Light Scattering (DLS) depends upon monitoring the fluctuation in intensity of scattered light over time. Sequentially recorded scattering patterns will be dissimilar if the particles are moving quickly, evaluating this, known as the correlation, gives an indirect measure of particle velocity. Figure 3.13 shows how the correlation of scattering as a function of time depends upon particle size and allows the particle size distribution to be calculated from the intensity of scattered light. DLS coupled software will typically provide calculation of particle volume distribution by applying Mie theory to the size distribution as well as generating a number distribution. Particle number distributions are of interest as they remove the bias originating from the intense scattering caused by larger particles, however, it should be noted that small measurement errors become significant in the calculation of the number distribution.

3.2.7.2 Underlying Theory of Zeta Potential Measurement

The method for measurement of zeta potential employed in this work is electrophoresis. Electrophoresis is the movement of charged particles under an applied electrical field.

As discussed in section 2.4.1.2, DLVO theory describes the distribution of ions

and variation of electric potential within a solution of charged particles. If the electric potential at the surface of a charged particle is ψ_0 then the adsorbed counter-ions cause the potential to decrease to the value of ψ_d at the Stern plane, after which the potential decays exponentially from the diffuse layer to the main body of the solution.

It is the edge of the Stern layer that is considered the surface of hydrodynamic shear, also known as the slipping plane. This is the exterior surface of the entity which moves through the liquid during electrophoresis. Thus the potential measured using electrophoresis (and other hydrodynamic methods), is not the true surface potential but is the electric potential found at the edge of the slipping plane, ψ_d, referred to as the zeta potential, ζ.

The movement of particles during electrophoresis is known as electrophoretic mobility and can be measured by the phase change of the light scattered by moving particles (Phase Analysis Light Scattering). The charged particles moving under the influence of the electric field will maintain a constant velocity when equilibration is achieved between the force of electrostatic attraction and the viscous drag which opposes it. The Henry formula, equation 3.8, is used to determine the zeta potential, ζ, from the measured electrophoretic mobility, μ_e. This calculation also requires the dielectric constant of the medium, ε, and viscosity of the medium, η to to be known.

$$\mu_e = \left[\frac{2\varepsilon\zeta}{3\eta}\right] f_1(\kappa a) \tag{3.8}$$

The function, $f_1(\kappa a)$, is dependent upon the solution's characteristic Debye length, κ, the particle radius, *a*, and varies in value between 1 (the Hückel approximation) and 1.5 (the Smoluchowski approximation). Fortunately, incorrect or uninformed assignment of $f_1(\kappa a)$ introduces only a small multiplication error.

As is the case of determining a particle size distribution from DLS, zeta potential calculation requires many assumptions to be made about the system of study. Whilst a zeta potential of magnitude greater than $\pm$ 25 mV may be used to indicate the stability of a solution against aggregation [111], the sign provides an indication of character of the ions absorbed at the Stern layer.

3.2.7.3 DLS and Zeta Potential
Sample Preparation and Measurement

Measurements were conducted using the Malvern ZetaSizer Nano Series ZEN 3600 (fitted with 633 nm laser). Solutions were decanted into square glass cuvettes (Malvern, Product number: PCS1115) for DLS measurement, with the additional inclusion of the specialist dip cell for zeta measurements in non-aqueous solvents (Malvern, Product number: ZEN1002). All sample preparation was conducted in the inert atmosphere of the glovebox and cuvettes were sealed to the lid or dip cell (depending on the measurement) with heated wax (purchased: Hampton Research, product: HR4-328) to minimise air exposure during measurement.

Chapter 4

Results I: Production of Two Dimensional Bi_2Te_3 and Sb_2Te_3 Nanosheets

The purpose of this chapter is to provide a broad introduction to the materials of interest by discussing the results of initial explorative experiments. It became evident early on in this work that the insights gained from successful dissolution of charged graphene [77], carbon nanotubes [146] and fullerenes [103] had limited transferability to the dissolution of intercalated pnictogen chalcogenide layered compounds. Whilst desired nanosheets of Sb_2Te_3 and Bi_2Te_3 could be produced, a number of other species were observed in the solution deposits and small changes in solution preparation could greatly impact the observed results. This chapter therefore focuses on establishing best experimental practice for the preparation and handling of these solutions by addressing the questions that remain unanswered and were not evident from the dissolution of carbon based materials.

The work aims to address the most pertinent questions, these are the 'what', 'when', and 'how':

- **What?** - What (nano)material is present in solution?
- **When?** - When does this (nano)material appear in solution?

- **How?** - How does the altering the intercalation compound impact the (nano)material that is produced?

These questions will be addressed in this order. By creating dropcast samples from prepared solutions, the material present will be characterised using TEM and each solvent will be evaluated with regards to their ability to produce 2d nanomaterials of Sb_2Te_3 and Bi_2Te_3. TEM will also be used to investigate the temporal evolution of the spontaneous exfoliation and diffusion process, focusing on the question of when this nanomaterial appears in solution. Finally, a range of intercalation compound stoichiometries are explored to determine the optimum concentration of metal to be used during intercalation for the production of pristine nanosheets. The work within this chapter is important as it establishes a foundation for the work described in following chapters, by informing the best experimental practice and experimental design, as well as introducing areas of special interest.

4.1 Preliminary Characterisation of Nanosheet Solutions

The production of 2d nanomaterials via spontaneous liquid phase exfoliation is of critical importance to this work. This work was inspired by previous studies of graphene production using solutions of graphite intercalated compounds (GIC) in aprotic solvents [77][90] and therefore this work began by following much of the same experimental methods to assess whether the exfoliation method was transferable to other layered compounds. Thus the initial experiments were chiefly concerned with testing the applicability of this exfoliation method to pnictogen chalcogenide layered compounds. Upon achieving successful exfoliation, verified by positive identification of 2d material, further optimisation of the experimental methodology and conditions to better suit the pnictogen chalcogenide layered compounds was necessary. The following experiments demonstrate the applicability of these methods to exfoliate both Sb_2Te_3 and Bi_2Te_3 intercalated compounds, and also explores the suitability of the aprotic solvents (NMP, DMF and THF) which are commonly involved in the exfoliation of GICs.

4.1.1 Experimental Details

Four intercalated powders were produced following the described metal-ammonia intercalation method (see section 3.1), with an alkali metal to layered material molar ratio of 0.8:1. For the purposes of the initial investigation both potassium and lithium intercalation compounds were created for both Sb_2Te_3 and Bi_2Te_3, so that the four intercalated compounds were $Li_{0.8}.Sb_2Te_3$, $K_{0.8}.Sb_2Te_3$, $Li_{0.8}.Bi_2Te_3$, and $K_{0.8}.Bi_2Te_3$.

The solutions were prepared by addition of 5 mL of dried solvent (NMP, DMF, or THF) to 0.0080 g of intercalated powder within a glass vial, 12 solutions were produced in total. The solutions were left to dissolve, with no agitation, for a period of two weeks before any liquid was removed for testing. Over a period of two weeks the solutions turn from clear and colourless to dark and opaque. After two weeks had passed, TEM samples were prepared from each solution following the typical dropcast method (described in section 3.2.3). All sample preparation was completed in the air-free environment of an argon filled glovebox. The TEM samples were each analysed using TEM, characterising any material found using EDX and by recording SAED patterns for any crystalline material, with care taken to minimise air-exposure of the TEM grids during their transfer to the microscope.

4.1.2 Positive Identification of Nanomaterial

Nanosheets were found in the case of all the intercalation compounds and it was concluded that the chosen LPE method is suitable for exfoliation of Sb_2Te_3 and Bi_2Te_3. However, the observed results varied greatly between the solutions prepared using the three different solvents.

Figure 4.1 shows the nanomaterial collected for the nanosheet solutions, created using NMP as a solvent, for the intercalated materials: $Li_{0.8}.Sb_2Te_3$, $K_{0.8}.Sb_2Te_3$, $Li_{0.8}.Bi_2Te_3$, and $K_{0.8}.Bi_2Te_3$. All nanosheets displayed the expected diffraction pattern relating to their bulk material, thus demonstrating the preservation of chemical identity and crystallinity during dissolution.

Although nanosheets were produced from both Sb_2Te_3 and Bi_2Te_3 intercalation compounds, it was found that solutions of Bi_2Te_3 compounds, specifically $K_{0.8}.Bi_2Te_3$ solutions, appeared to have a greater number of pristine hexagonal nanosheets present. It is unclear what the predominant cause of this difference

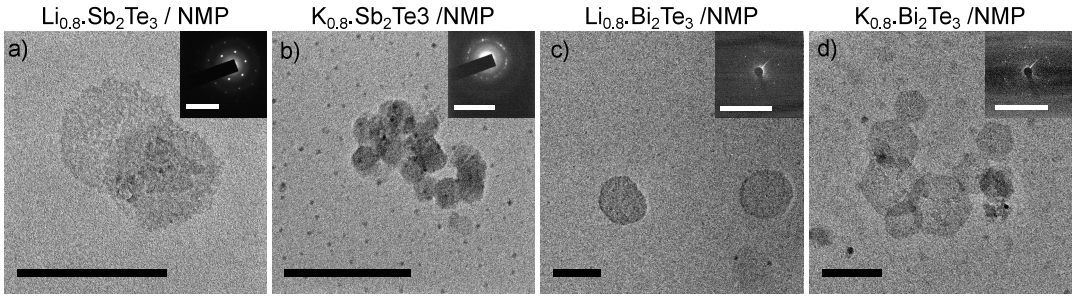

Figure 4.1: Nanosheets found within solutions prepared using NMP as a solvent. The TEM images show nanosheets found within the NMP solutions of a) $Li_{0.8}.Sb_2Te_3$, b) $K_{0.8}.Sb_2Te_3$, c) $Li_{0.8}.Bi_2Te_3$, and d)$K_{0.8}.Bi_2Te_3$. The SAED patterns are in agreement with the expected [001] diffraction for Sb_2Te_3 (insets a) and b)) and [001] diffraction for Bi_2Te_3 (insets c) and d)). The scale bar in each TEM image represents 200 nm and for SAED images the scale bar represents 10 1/nm.

is, but possible explanations include: i) the increased reactivity of Sb_2Te_3 compared to Bi_2Te_3 [147] resulting in fewer pristine Sb_2Te_3 nanosheets; ii) differences in layered materials and intercalant metals impacting the exfoliation of material; and iii) material dependant drying artefacts within TEM sample preparation.Thus, solutions of $K_{0.8}.Bi_2Te_3$ in NMP were chosen as the focus of many later experiments.

4.1.2.1 Choice of Solvent

In the case of each intercalated material solution it was found that flake-like particles, identified as either Sb_2Te_3 and Bi_2Te_3 depending on the solution, were present in the NMP and DMF solutions. However, no nanomaterial relating to the layered material was found in the THF solutions and unlike the NMP or DMF solutions which were dark brown/black in colour, the THF solutions remained clear/colourless. TEM images collected from $Li_{0.8}.Sb_2Te_3$ nanosheet solutions in NMP, DMF and THF are shown in figure 4.2 and are representative of the trends found for all the intercalated compounds.

In all solutions, rod-like nanoparticles were found and were identified as tellurium nanoparticles using SAED and EDX analysis, further discussion of telluruim nanoparticles can be found in section 6.2. Tellurium nanorods were the only nanomaterial apparent in THF solvent solutions and even solution agitation (bath sonication of the THF solutions for 30 minutes) did not change this result nor did it produce any evidence of flake-like material relating to the layered com-

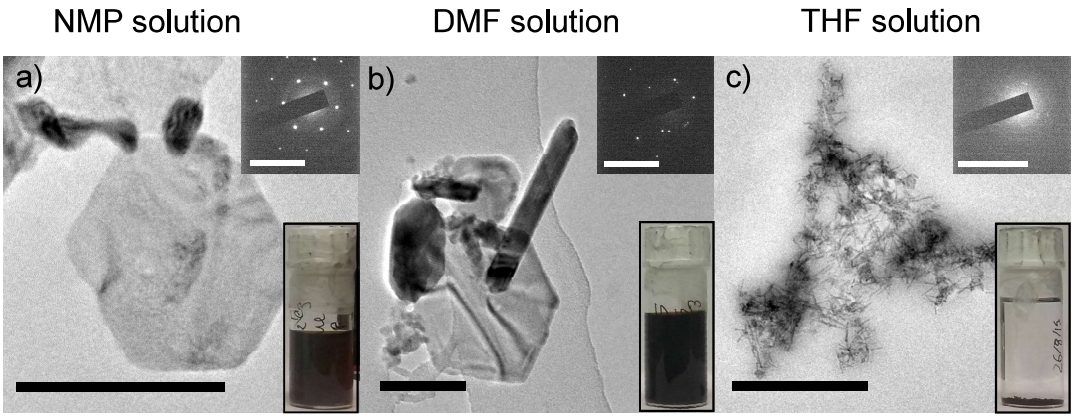

Figure 4.2: Nanosheet solutions produced with different aprotic solvents, a) NMP (N-Methyl-2-pyrrolidone), b) DMF (Dimethylformamide) and c) THF (Tetrahydrofuran). Photographs of the prepared $Li_{0.8}.Sb_2Te_3$ nanosheet solutions are shown alongside the TEM images, as well as the SAED of material shown. The scale bar in each TEM image represents 100 nm, except for TEM image c) where the scale bar represents 500 nm, and for all SAED images the scale bar represents 10 1/nm.

pounds. This initial investigation suggests that THF is an inappropriate solvent for spontaneous exfoliation of the intercalated pnictogen chalcogenide layered compounds and so the THF solutions were explored no further.

Although tellurium nanorods were present in both the NMP and DMF solutions, they were far more prevalent in the TEM analysis of the DMF solutions. Whilst DMF solutions were often explored, NMP was the preferred solvent for most later experimental work due to fewer observed impurities.

4.2 Temporal Evolution of Nanosheet Solutions

During the initial study of the nanomaterial solutions it was noted that the solutions created from NMP or DMF would gradually darken over a period of hours, whereas THF solutions would remain clear and colourless throughout their lifetime. It was proposed that this darkening of the solution was related to the gradual movement of the exfoliated nanomaterial throughout the solvent, with the lack of this colour-change relating to the lack of detected nanosheets in the THF solutions. To investigate the development of the solutions over time an experiment was conducted whereby a $K_{0.8}.Bi_2Te_3$ in NMP solution was sampled during the first hours following solution creation.

4.2.1 Experimental Details

The nanosheet solution sample was prepared by addition of 5 mL of NMP solvent to 0.0079 g of $K_{0.8}.Bi_2Te_3$, the solution was left to dissolve spontaneously, with no agitation. Aliquots were removed from the upper liquid level (near the liquid meniscus) of the prepared solution at timed intervals (t = 0, 1 hour, 4 hours, 8 hours, 24 hours and 2 weeks) and TEM samples were prepared using the aliquots following the typical dropcast method (described in section 3.2.3). Photographs were taken of the liquids immediately before droplet removal and TEM sample preparation.

4.2.2 Experimental Results

As observed during the preparation of all other NMP and DMF nanosheet solutions, the diffusion of material from the $K_{0.8}.Bi_2Te_3$ powder present at the base of the sample vial occurred over a period 24 hours, and coloured the NMP solution a dark brown/black. The energetically driven upward movement of this material correlated with the delayed detection of nanomaterial at the upper liquid level. Control solutions were also created but no there was no visible colour change or any nanomaterial found in solutions of unintercalation powder in solvent, thus suggesting that intercalation and charging of the materials is vital to the dissolution process.

The results of the TEM investigation of the solution over a period of two weeks is summarised in figure 4.3. Only rod-shaped particles, possessing a confirmed tellurium signal in EDX but unidentified crystalline diffraction, were found at the upper liquid level during the initial 8 hours. Crystalline flake-like particles, confirmed as Bi_2Te_3 using EDX and SAED, were found after 24 hours had elapsed, although they were small in size (~200 nm wide) and densely decorated with even smaller particles. Larger (~500 nm wide), pristine nanosheets, which were distinctly hexagonal in shape, were found in the solution after it was aged for 2 weeks.

Two additional TEM images, (f) and (g), may be seen in figure 4.3 and whilst these were not collected from the same solution they were taken from solutions of $K_{0.8}.Bi_2Te_3$ in NMP which were created from the same batch of intercalated powder using the same mass to solvent volume ratio. The images show that pristine hexagonal nanosheets were found after only four days, providing useful

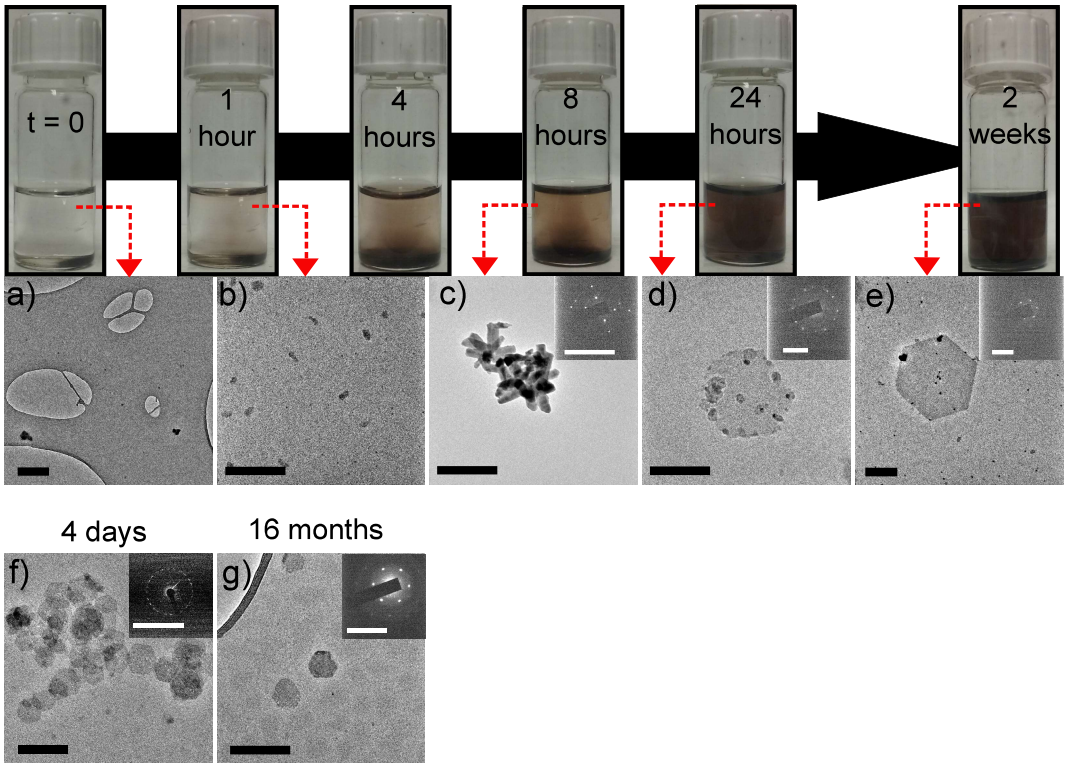

Figure 4.3: The dissolution of $K_{0.8}.Bi_2Te_3$ in NMP over a period of 2 weeks, through photographic observation of the liquid sample and characterisation of the solution using TEM. TEM images are representative of particles found in solution at a) initial creation (time zero), b) after 1 hour elapsed, c) after 8 hours elapsed, d) after 24 hours elapsed, and e) after 2 weeks since the addition of solvent to intercalated powder. Solutions created from the same intercalated powder were also sampled and TEM image f) represents hexagonal nanosheets found in a solution aged 4 days, whilst TEM image g) shows nanosheets found in a solution aged 16 months. In the case of the crystalline features, the associated SAED is shown. The inset SAED are in agreement with [001] Bi_2Te_3 for images d), e) f) and g), but the pattern remains unidentified for image c).The scale bar for all TEM images is 200 nm and for SAED the scale bar represents 10 1/nm.

information about the solution development between 24 hours and two weeks. Alongside this, the observation of hexagonal, crystalline nanohseets in a solution of $K_{0.8}.Bi_2Te_3$ in NMP which was 16 months old demonstrates the long-term stability of these solutions.

This investigation shows that the appearance of nanosheets is dependent on the diffusion of nanomaterial throughout the liquid volume, with days taken for the nanomaterial to be detectable at the upper liquid level. These results have also informed appropriate experimental design, deciding that at least 4 days should be given for solution equilibration before testing.

4.3 Modification of the Intercalated Material

The idea that solution conditions may be modified to influence the nanomaterial exfoliation has already been introduced. However, the intercalated material is the precursor to the nanosheet solutions and therefore it plays a critical role in determining the character (morphology, charge, crystallinity, reactivity) of the resultant nanomaterial. This section will focus on the intercalated materials, which are first characterised using PXRD, after which a range of intercalation compounds are evaluated with respect to their ability to produce pristine nanosheets. Specifically, a range of potassium Bi_2Te_3 intercalation materials were created and used to produce solutions which were then characterised using TEM and AFM.

4.3.1 Characterisation of the Intercalated Material

As mentioned previously, this work has been greatly influenced by the wealth of research surrounding graphite intercalation compounds. The characterisation of GICs using XRD shows that they display a range of intercalation stoichiometry and the acceptance of the alkali metal cations is marked in their diffraction pattern by the measurable increase in interlayer separation [96]. This shift in GIC (00l) peaks to lower Q values provides confirmation of successful material intercalation and reveals the different organisation of the intercalants throughout the layered structure, known as staging. With this knowledge being utilised for selective liquid phase exfoliation of bilayer and trilayer graphene nanosheets [76]. The powder x-ray diffraction (PXRD) patterns of the Sb_2Te_3 and Bi_2Te_3 intercalation compounds were collected and compared to their initial starting materials, as well

as outgassed material, to assess the impact of intercalation on their crystallintiy and possible presence of contaminants.

4.3.1.1 Experimental Details

The powder x-ray diffraction (PXRD) patterns were collected for the commercially sourced powders (Sb_2Te_3 and Bi_2Te_3), before and after outgassing, as well as their intercalation compounds ($Li_{0.8}.Sb_2Te_3$, $K_{0.8}.Sb_2Te_3$, $Li_{0.8}.Bi_2Te_3$, and $K_{0.8}.Bi_2Te_3$). PXRD samples were prepared and measured following the details given in section 3.2.1. To maximise intensity of the diffraction patterns a molybdenum source was used for the Sb_2Te_3 and its related compounds, and a copper source was used for the Bi_2Te_3 and its related compounds.

4.3.1.2 PXRD Study of Bi_2Te_3 Materials

The XRD patterns for the commercially sourced Bi_2Te_3 powder (purchased from Sigma Aldrich) and the outgassed Bi_2Te_3 powder are in agreement with the expected Bi_2Te_3 diffraction pattern (ICSD-184631) [148]. It was found that outgassing caused no detectable decomposition or change in the crystallinity of the powder. Following intercalation, the x-ray diffraction pattern was collected for both $Li_{0.8}.Bi_2Te_3$ and $K_{0.8}.Bi_2Te_3$ powders and these patterns are shown following the removal of low-level amorphous background, alongside the diffraction pattern collected for the commercially sourced Bi_2Te_3, in figure 4.4.

Whilst $Li_{0.8}.Bi_2Te_3$ and $K_{0.8}.Bi_2Te_3$ both exhibit the diffraction peaks expected of Bi_2Te_3, there are additional diffraction peaks (marked with an asterisk) present in the diffraction pattern of the potassium intercalated material. The crystalline material responsible for these additional diffraction peaks has been identified as potassium polytelluride and its presence will be discussed in more detail in section 6.2. Despite the presence of additional peaks, the XRD patterns show that the crystallinity of Bi_2Te_3 is preserved in the intercalated powder. Unlike the XRD of GIC materials [96], there is no detectable (00l) peak shift in the Bi_2Te_3 interclation powders. However, similar results have been found for $Li.Bi_2Te_3$ [149] and the related intercalation material, $Cu.Bi_2Te_3$, where intercalants where held between the quintuplet layers and intercalation was found to produce no detectable change in monolayer separation [150].

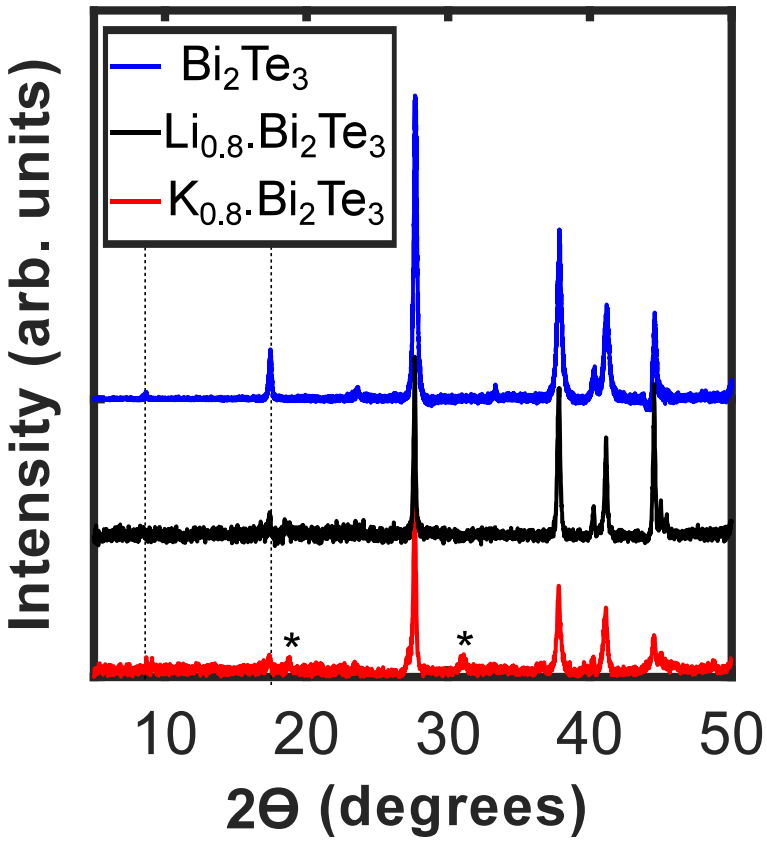

Figure 4.4: Combined plot of PXRD pattern collected for $Li_{0.8}.Bi_2Te_3$, $K_{0.8}.Bi_2Te_3$ and the commercially sourced Bi_2Te_3. All patterns were found to be in agreemenet with reference Bi_2Te_3 pattern (ICSD-184631) [148]. Although no shift was detected, the dotted lines indicate peaks expected to shift if intercalation were to cause an increase in van der Waals gap spacing. The additional peaks present in the $K_{0.8}.Bi_2Te_3$ diffraction pattern have been marked with an asterisk.

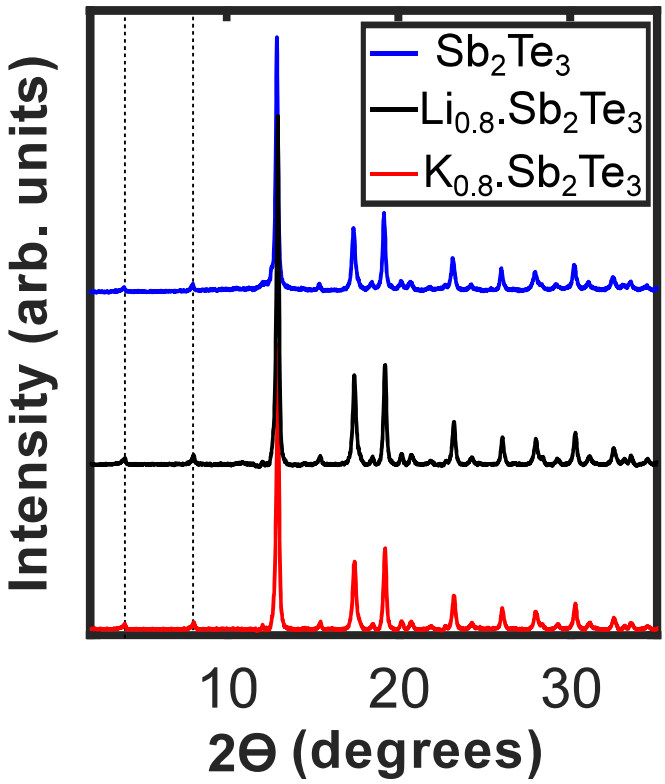

Figure 4.5: Combined plot of PXRD pattern collected for $Li_{0.8}.Sb_2Te_3$, $K_{0.8}.Sb_2Te_3$ and the commercially sourced Sb_2Te_3. All patterns were found to be in agreemenet with the reference Sb_2Te_3 pattern (ICSD-193344) [151]. Although no shift was detected, the dotted lines indicate peaks expected to shift if intercalation were to cause an increase in van der Waals gap spacing.

4.3.1.3 PXRD study of Sb_2Te_3 Materials

The XRD patterns for the commercially sourced Sb_2Te_3 powder (purchased from Sigma Aldrich) and the outgassed Sb_2Te_3 powder were in agreement with the expected Sb_2Te_3 diffraction pattern (ICSD-193344) [151]. Following intercalation, the x-ray diffraction pattern was collected for both $Li_{0.8}.Sb_2Te_3$ and $K_{0.8}.Sb_2Te_3$; both were found to match that of the starting powder, showing no detectable decomposition or additional diffraction peaks. There is a lack of detectable change in diffraction pattern as a result of intercalation, however, this was also true of the Bi_2Te_3 intercalation materials produced in this work, and smiliar work [149][150]. Figure 4.5 is a plot of the XRD patterns collected for the potassium and lithium intercalated Sb_2Te_3 powders following the removal of low-level amorphous background, alongside the diffraction pattern collected for the commercially sourced

Sb_2Te_3.

4.3.2 Influencing Nanomaterial Exfoliation by Variation of Intercalation Stoichiometry

The influence of metal intercalant ratio on the exfoliation and stabilisation of the nanosheet solutions was investigated. For this purpose, five potassium intercalated Bi_2Te_3 compounds, each with differing alkali metal ratio, were added to NMP solvent and the material present was characterised using TEM and AFM.

It should be noted that whilst the intercalation compounds are described and discussed as $K_x.Bi_2Te_3$, where *x* may represent any number, it is probable that this is not always the true stoichiometry of the compounds. In the case of high alkali metal concentration, the alkali metal may not intercalate to produce the higher metal ratio compounds but may instead reduce the layered material. Even in the case of the low metal concentrations, the given stoichiometry will not be a true representation of the intercalated metal as a small fraction of alkali metal in the metal ammonia solution will be consumed by undesirable side reaction (to produce metal amines, as discussed in section 8.1). However, for the purpose of this work $K_x.Bi_2Te_3$, will be used to represent the relative concentration of alkali metal used during the metal-ammonia intercalation procedure.

4.3.2.1 Experimental Details

Five potassium intercalated Bi_2Te_3 compounds, each with differing alkali metal ratio, were created following the normal metal-ammonia intercalation method (described in section 3.1). The different intercalation compounds were created by altering the mass of alkali metal present in the metal ammonia solution, the mass of powdered layered material used and volume of ammonia added did not vary. In order of increasing alkali metal content, the prepared intercalated compounds are as follows: $K_{0.1}.Bi_2Te_3$, $K_{0.2}.Bi_2Te_3$, $K_{0.8}.Bi_2Te_3$, $K_{1.5}.Bi_2Te_3$, $K_4.Bi_2Te_3$, $K_5.Bi_2Te_3$.

Solutions were created for each intercalated powder by adding 5 mL of NMP to 0.0080 g of the intercalated powder. The solutions were left, undisturbed, for 2 weeks before any analysis was completed. TEM samples were prepared for each solution following the typical dropcast method (described in section 3.2.3). AFM samples were prepared for select solutions (specifically the solutions of

$K_{0.2}.Bi_2Te_3$, $K_{0.8}.Bi_2Te_3$ and $K_{1.5}.Bi_2Te_3$) following the typical dropcast method (described in section 3.2.5). All sample preparation was carried out in the inert atmosphere of an argon filled glovebox.

4.3.2.2 Experimental Results

The influence that alkali metal concentration has upon the production of nanosheets in NMP solution is summarised in figure 4.6. The data presented in the figure suggests that there is a small range of alkali metal concentrations which produce the desired, pristine hexagonal nanosheets. For the intercalation compounds considered, there is an optimal alkali metal ratio ($K_x.Bi_2Te_3$) where $0.1 < x < 1.5$ for the production of nanosheets.

No nanomaterial was found within TEM or AFM study of the solution of the low metal intercalation compound $K_{0.1}.Bi_2Te_3$, suggesting that this metal ratio was too low for favourable exfoliation. Whereas, for the higher metal ratio compounds ($K_4.Bi_2Te_3$, $K_5.Bi_2Te_3$) only impurities were found. These impurities were identified (using EDX) as containing potassium and tellurium, suggesting possible chemical attack or decomposition of the layered material in these solutions.

The NMP solutions produced using the intercalation compounds of intermediate metal concentration ($K_{0.2}.Bi_2Te_3$, $K_{0.8}.Bi_2Te_3$, $K_{1.5}.Bi_2Te_3$) were found to produce flake-like particles and they were further characterised with AFM, although in the case of $K_{1.5}.Bi_2Te_3$ solution these sheets appeared to be damaged. The features found within the AFM studies were in agreement with the trends found when using TEM to study the samples.

The areas highlighted in the AFM height images of figure 4.6 may be seen in more detail in figure 4.7 where representative height profiles are also shown for the dropcast nanosheets. The AFM images and height profiles show that collections of hexagonal nanosheets were found for the $K_{0.2}.Bi_2Te_3$ and $K_{0.8}.Bi_2Te_3$ NMP solutions but only features with rough-edges and appreciable surface roughness could be found in the $K_{1.5}.Bi_2Te_3$ NMP solution. It is interesting to note that height profile corresponding to the overlapping nanosheets seen in plot aii) of figure 4.6, is not equal to the sum of the measured height of the nanosheets. This measurement, was one of many similar examples of overlapping nanosheets found during extensive AFM studies, and it suggests that the measured nanosheet height may be an overestimate due to an additional height contribution, related to remaining solvent residue and reaction of the sample in air.

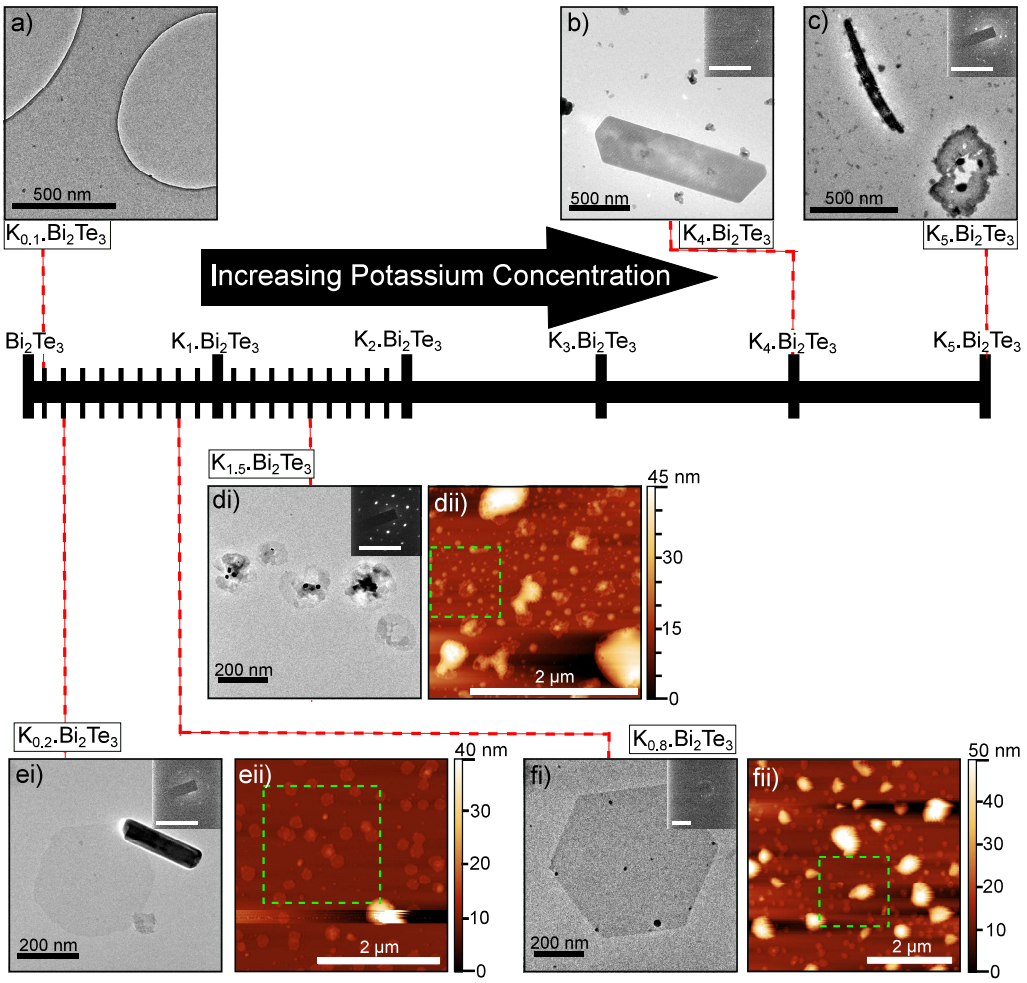

Figure 4.6: Material deposited from NMP solutions of Bi_2Te_3 potassium intercalation compounds with varied stoichiometry. TEM images collected of deposited NMP solutions of a) $K_{0.1}.Bi_2Te_3$, b) $K_4.Bi_2Te_3$ and c) $K_5.Bi_2Te_3$ show the lack of nanosheets found in these solutions. Images b) and c) include the inset SAED of the impurities shown, although crystalline, the patterns could not be identified. The TEM images (with SAED inset) and AFM (tapping mode) images are shown for the NMP solutions of d) $K_{1.5}.Bi_2Te_3$, e) $K_{0.2}.Bi_2Te_3$ and f) $K_{0.8}Bi_2Te_3$ which show that nanohseets were produced in these solutions. The highlighted boxes within AFM images dii), eii) and fii) relate to areas of further investigation, as presented in figure 4.7. Scale bars differ for each image and have been labelled accordingly.

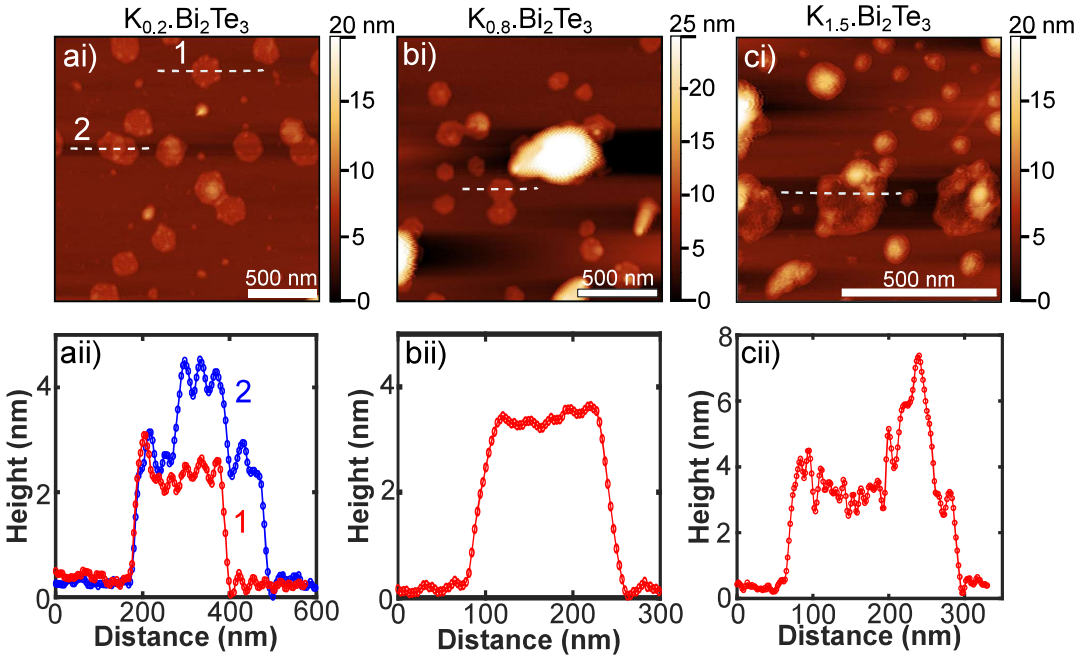

Figure 4.7: Tapping mode AFM images of Bi_2Te_3 nanosheets and the associated height profiles of the selected trace. AFM images ai), bi) and ci) represent nanosheets found in NMP solutions of $K_{0.2}.Bi_2Te_3$, $K_{0.8}.Bi_2Te_3$ and $K_{1.5}.Bi_2Te_3$, respectively, and are related to the highlighted areas of interest as seen in figure 4.6. The height profiles in aii) give an average nanosheet thickness of 2.1 nm for particle 1, and average thickness of 2.3 nm (for individual nanosheets) and an additional height of 1.6 nm for the overlapping region. The height profile in bii) gives an average thickness of 3.3 nm, the average thickness of the particle in cii) has been undefined due to surface roughness.

4.4 Conclusions

The work within this chapter shows that pristine, crystalline, hexagon-shaped nanosheets of Sb_2Te_3 and Bi_2Te_3 may be produced within solution without the need for agitation or high temperatures, using a method relying upon intercalation of the layered material. The spontaneous exfoliation of material is accompanied by a diffusion process so that it takes days for the nanomaterial to become detectable at higher liquid levels. The collection of pristine nanosheets from a 16 month old solution, demonstrates the incredibly desirable property of extensive solution stability. It was found that THF is an unsuitable solvent for the spontaneous exfoliation of intercalated pnictogen chalcogenide layered compounds: $Li_{0.8}.Sb_2Te_3$, $K_{0.8}.Sb_2Te_3$, $Li_{0.8}.Bi_2Te_3$, and $K_{0.8}.Bi_2Te_3$. However, both NMP and DMF were found to be suitable solvents for these intercalation compounds, although the results suggest that NMP produces fewer tellurium-based impurities.

Although impact of intercalation was not detected in the XRD patterns of the layered materials as is the case in GIC (graphite intercalation compounds), it was found that metal concentration during intercalation has a great impact on the material present in solution. It was shown that there is an optimum range of concentration of alkali metal ($K_x.Bi_2Te_3$, where $0.1 < x < 1.5$) which should be observed if undamaged nanosheets are to be produced, without increasing the yield of other impurities and contaminants.

The concise summary of the experimental results within this chapter does little to reflect the significance or importance of the demonstration of exfoliation of Sb_2Te_3 and Bi_2Te_3. It should not be underestimated how much time was dedicated to the development and adaptation of experimental techniques to incorporate the use of air-sensitive materials. This chapter has shown that the materials are worth pursuing, the results give important information on the materials and also inform the design of future experiments to minimise experimental artefacts and to aid fruitful exploration. The experiments have also highlighted areas of interest which will form the basis of the following results chapters.

Chapter 5

Results II: Determining the Nanosheet Size Distribution

It has been demonstrated that 2d nanosheets of Sb_2Te_3 and Bi_2Te_3 may be produced using the chosen spontaneous liquid phase exfoliation method. Such nanomaterials are of interest for use within thermoelectric devices, however, such applications require very specific size and morphology of nanomaterial [4][20]. Thus it is crucial that the size and morphology of the produced nanomaterial is understood and that a more extensive description of the material within solution is obtained. The work presented in this chapter demonstrates the great volume of nanomaterial present in solution, with thousands of nanosheets being sampled, to provide a statistical description of the material and to demonstrate the ability of this method to meet the demands of mass production.

Solutions of potassium intercalated Bi_2Te_3 in NMP have been chosen as the focus of this chapter due to the high frequency of pristine nanosheets observed in the deposits of these solutions. Both direct (TEM, AFM, liquid TEM) and indirect (SAXS) methods have been used to measure and characterise the Bi_2Te_3 nanosheet dimensions. TEM was used in conjunction with SAED and EDX to confirm nanosheet crystallinity and chemical identity whilst also allowing the nanosheet diameter to be determined. Following this fundamental characterisation, AFM was used to provide further information on both nanosheet diameter and nanosheet thickness. A limitation of these direct methods is that they may not provide a true

representation of the nanomaterial sample as a whole, this was mitigated by the sampling of thousands of nanosheets. SAXS measurements were completed to provide the complementary, average sample description of these solutions (indirect). Preliminary liquid TEM experiments provide a balance between *in situ* and direct measurement of the nanosheet solutions.

5.1 Preliminary Investigation of Nanosheet Diameter Using TEM

The ability of TEM, in conjunction with SAED and EDX, to characterise and resolve individual nanoparticles has already been demonstrated within the previous chapter. However, the technical strengths of TEM are sometimes undermined by a weakness in experimental technique that leads to general conclusions being made from the observation of a limited number of nanoparticles. To avoid this issue, a series of TEM samples were created from aliquots removed throughout the liquid volume and from these samples hundreds of nanosheets were imaged and identified. By measuring the lateral width of each individual hexagonal nanosheet and then applying statistical analysis to gain further insight, a description of the nanosheets, which includes their variation in size, has been obtained.

5.1.1 Experimental Details

TEM was employed to complete a preliminary investigation into the size distribution of $K_{0.8}.Bi_2Te_3$ nanosheets deposited from solution. These three samples were taken to gain a representation of the nanosheets present in solution and to investigate whether the distribution of their lateral sizes relates to their relative liquid depth.

5.1.1.1 Preparation of Solutions and TEM Samples

3 mL of anhydrous dried NMP was added to 0.0045 g of $K_{0.8}.Bi_2Te_3$ and was left to dissolve, unperturbed. After 5 days, three TEM samples were prepared following the typical dropcast method (described in section 3.2.3) using aliquots taken from different liquid depths. Two of the three liquid samples were taken from

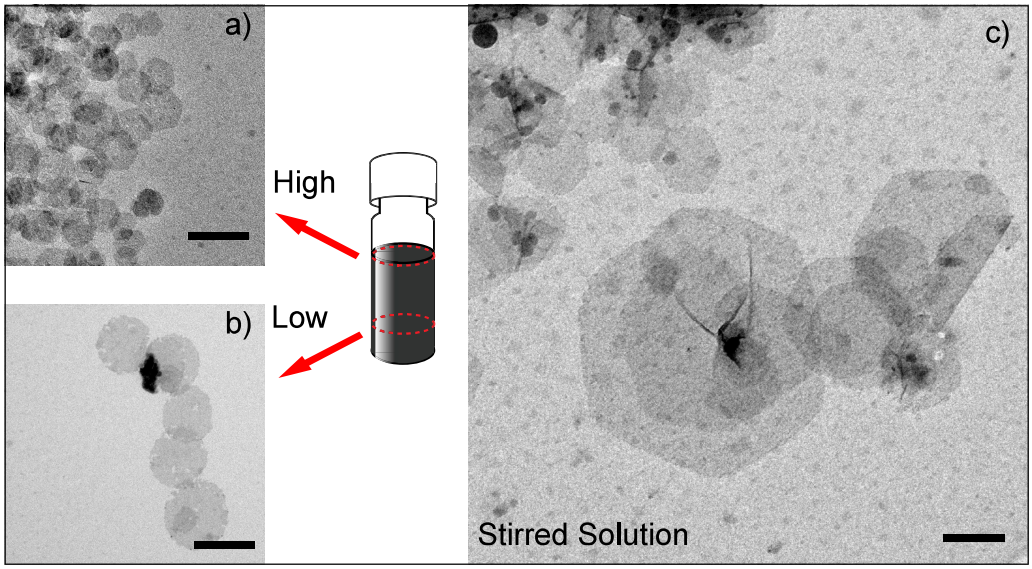

Figure 5.1: The distribution of hexagonal Bi_2Te_3 nanosheets with differing sizes throughout solution. Image a) is a TEM image of smaller nanosheets found within the high liquid level, image b) is a TEM image of wider nanosheets found within the low liquid level, and image c) is a TEM image of small and large nanosheets found within the stirred liquid. All scale bars represent 200 nm, it should be noted that image c) has been enlarged so that the length scale in each image is equal, as demonstrated by the agreement of the scale bars.

distinctly different depths in the liquid, one from the upper liquid level, just below liquid meniscus level, and the other sample was removed from the lower liquid level, just above the undissolved powder found at the base of the vial. The third sample was taken from the mid-level liquid depth following stirring of the liquid for 2 minutes using a glass pipette.

5.1.1.2 TEM Data Collection

The deposited nanosheets were imaged using TEM and figure 5.1 provides a diagram of the liquid depth dependent sampling method as well as presenting TEM images that are representative of each of the distinct aliquots. Each TEM image has been presented so that their length scales are equal so that sample differences may be easily appreciated. The nanosheets collected from the high liquid depth were found to have a smaller lateral width than those found within the lower liquid depth. As might be expected, the stirred liquid sample presents nanosheets with a range of lateral dimension.

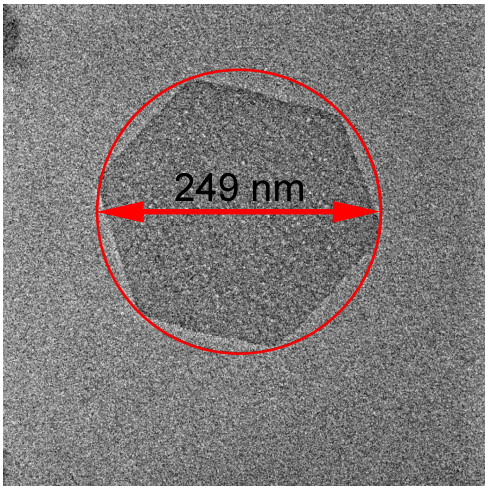

Figure 5.2: The chosen measurement method of the lateral dimension of the nanosheets. The TEM image of a nanosheet deposited from a $K_{0.2}.Bi_2Te_3$ / NMP solution has been encircled and the diameter of the circle, 249 nm, is taken as the lateral dimension of the nanosheet.

5.1.1.3 TEM Micrograph Analysis

From TEM images the Bi_2Te_3 nanosheets were identified and individually analysed. An ability to reliably identify the nanosheets was developed from the experience of carefully analysing numerous nanoparticle samples, so that as well as using diffraction methods and EDX to characterise the nanosheets, nanosheets could be identified by: their hexagonal shape (distinct from the shape of common contaminants); their stability in the electron beam (distinct from the damage caused by the beam to common contaminants); and their image contrast with the carbon film (related to particle thickness and chemical character).

Each nanosheet diameter was measured using tools found within the commercially available microscope software (Gatan Digital Micrograph), with no reduction in the image resolution. As some hexagonal nanosheets were found to be irregular in shape it was decided that the lateral dimension of the nanosheets should be measured by encircling the nanosheets and recording the diameter of the circle. Thus providing more confidence than a single point-to-point measurement. This choice of measurement method is demonstrated in figure 5.2. It should be noted that the diameter of this circle, equal to the vertex-to-vertex length is twice the value of the dimension used in the common geometric definition of a regular hexagon (the side length).

5.1.1.4 Error Consideration

The challenges related to nanosheet measurement should be mentioned and experimental error considered. Assuming the appropriate choice of magnification for the nanosheet size, the image resolution and microscope alignment do not contribute significant error in the measurement. Instead the major error in this measurement will be related to the encircling of the hexagon. Although this measurement may be considered a random error, the approximate value given to this error is ± 10 nm.

It should also be noted that as well as the presence of isolated nanosheets, large collections of nanosheets were formed on the TEM carbon film. Figure 5.3 is a composite image created from a number of TEM images, showing a collection of nanosheets dropcast from a $K_{0.8}.Bi_2Te_3$ /NMP solution. This figure demonstrates the large volume of nanosheets present, as well as the difficulty of distinguishing the individual nanosheets in the densely crowded areas. As a result, such densely populated areas were not included in the nanosheet counting and measurement. The nanosheets most likely to be omitted from measurement are the smaller particles, as larger particles have a greater area of coverage and clearer edge definition, and thus have a higher probability of positive identification.

Although rare, the presence of contaminant particles, as seen in the stitched image in figure 5.3, can also act to obscure the nanosheets. It is also interesting to note that nanosheets, especially those with a larger diameter, are sometimes folded.

5.1.2 Analysis of Nanosheet Lateral Dimension Data

The collection of nanosheet diameters measured for each deposited aliquot were analysed further by creating a histogram for each dataset and then finding an appropriate fit for the data, which enabled further description, insight and comparison of the data sets.

5.1.2.1 Creating Histograms

The measured nanosheet diameters were binned to create a histogram of the frequency of nanosheet diameter for each of the three samples. Whilst the con-

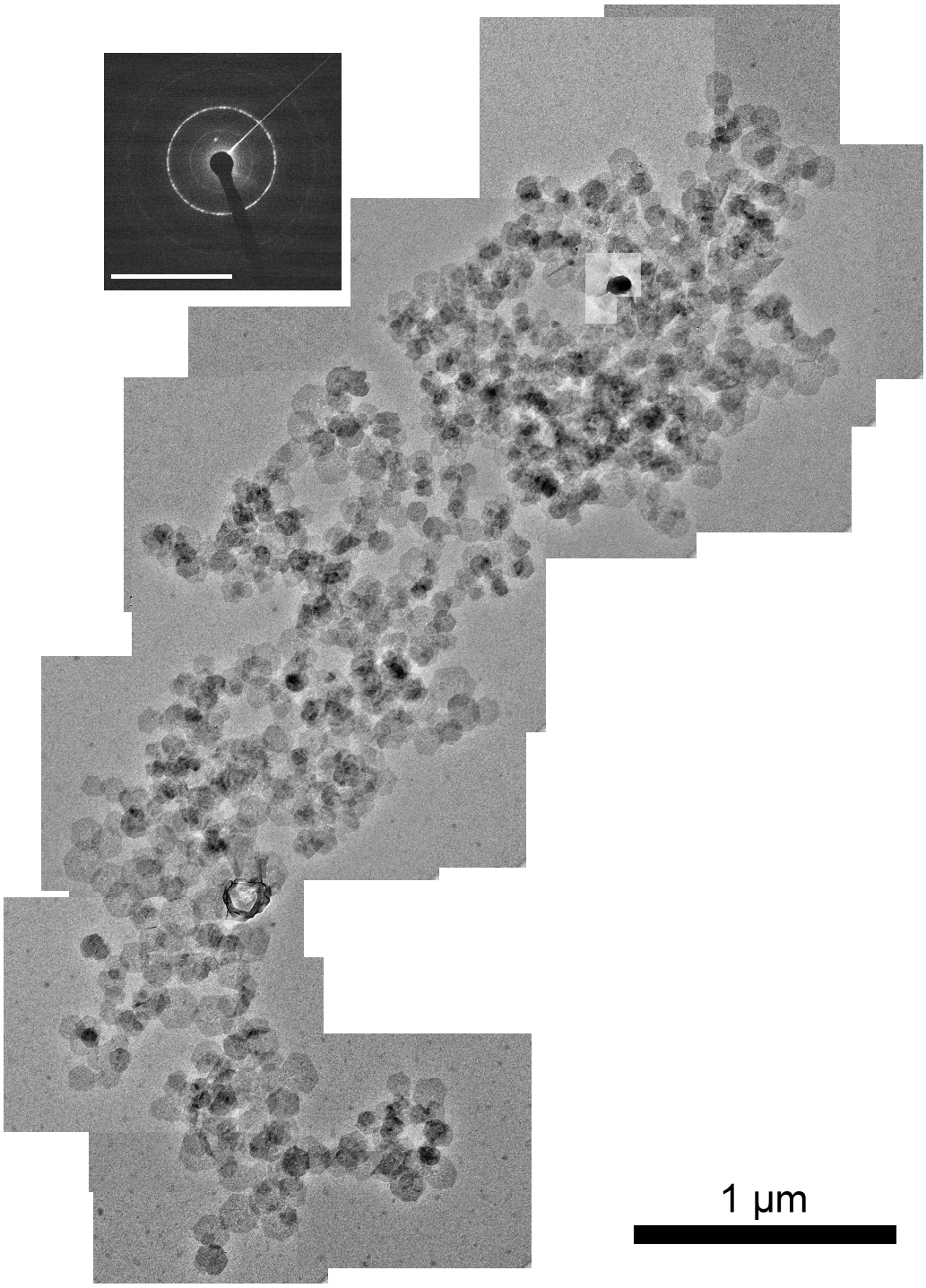

Figure 5.3: An image constructed from a collection of TEM images that show a large collection of hexagonal Bi_2Te_3 nanosheets deposited from the high liquid level of a 4 day old $K_{0.8}.Bi_2Te_3$/ NMP solution. The inset SAED is agreement with [001] Bi_2Te_3, with concentric rings due to turbostratic layering of deposited nanosheets. The scale bar represents 1 µm for the TEM image and for SAED the scale bar is 10 1/nm.

struction of a histogram can provide a means of intuitive data analysis as well as a way of discriminating outliners and other noise in the data this is all greatly dependent on the choice of bin width. Therefore a rule was constructed for the choice of histogram bin width. The rule is grounded in experimental understanding as well as statistical theory.

The bin width for each histogram was determined by Scott's normal reference rule [152], which is given in equation 5.1 and relates the bin width, *h*, to the standard deviation, σ and the number of data points collected *n*.

$$h = \frac{3.5\sigma}{n^{1/3}} \tag{5.1}$$

It was decided that the minimum possible bin width should be informed by the experimental data and fixed as the estimated error in the measurement (± 10 nm). Therefore the minimum allowed bin width was 20 nm.

From inspection of the histograms created using this rule for bin width choice, it was decided that this was an appropriate and useful rule, producing histograms with minimal distortion resulting from limited sample size and any experimental noise.

5.1.2.2 Choice of Fitting Model

The histograms were then fitted with a probability density function (PDF) to provide further description of the data. It is common convention to apply a log-normal PDF to the particle size distribution, as is done to particles produced by ball milling as well as sonication of layered materials in the liquid phase [153]. However, on first inspection of the histogram distributions it was noted that they did not have a pronounced positive skewness and so it was not obvious that log-normal distribution would be the best choice of fit.

Each dataset was fitted with both a normal distribution and a log-normal distribution to determine the distribution which best represented the data. This was evaluated using chi-squared, χ^2, analysis and the fit was considered good if the χ^2/υ value was near in value to 1. Further details of the chi-squared test may be found in the appendix, section 8.3. Further details of the two different probability density functions can be found in the appendix, section 8.2.

Figure 5.4 shows the data points, taken from each histogram, fitted with a

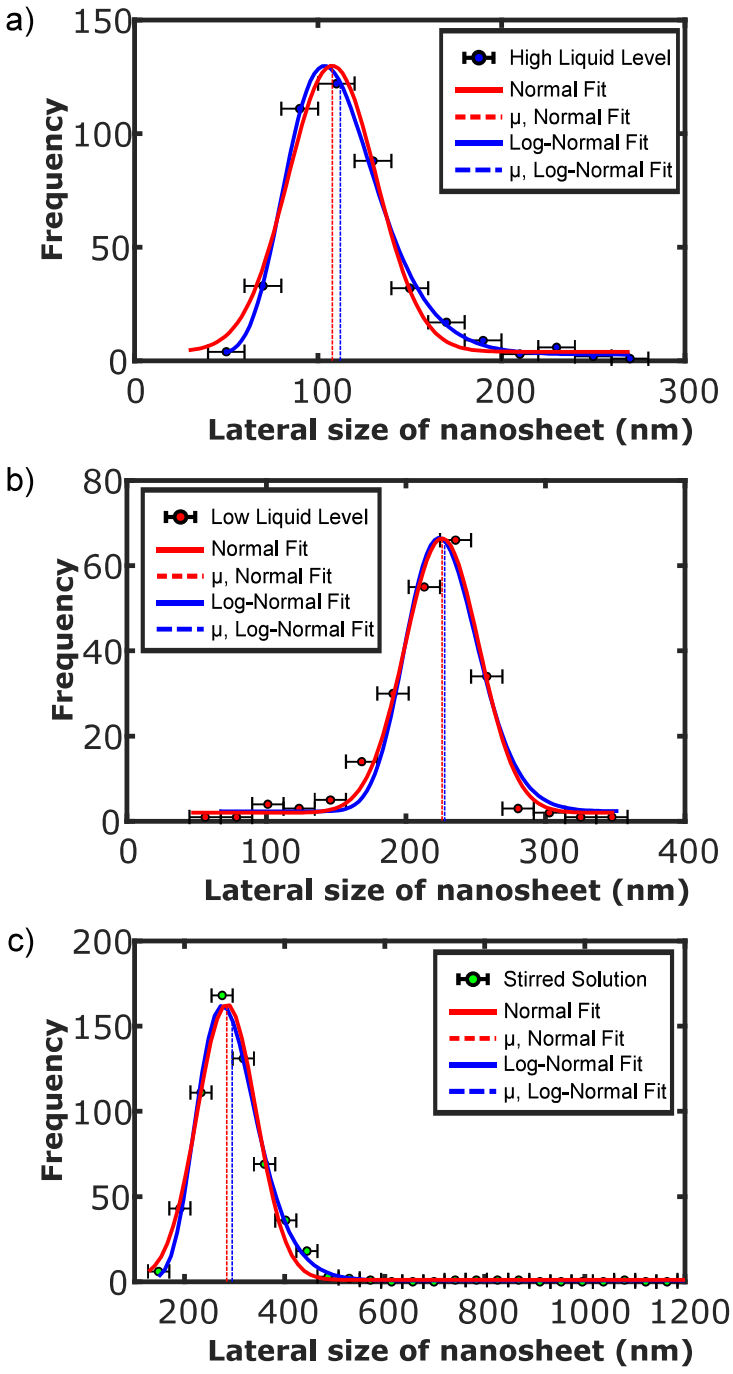

Figure 5.4: Comparing the result of fitting a normal and a log-normal distribution to a histogram of lateral width of nanosheets. The three data sets were collected from TEM micrograph analysis of the Bi_2Te_3 nanosheets deposited from aliquots taken from the a) high liquid level, b) low liquid level and c) following stirring of a $K_{0.8}.Bi_2Te_3$ /NMP solution.

normal and log-normal distribution. From the figure it can be seen that the fits are similar in shape due to the limited skewness of the data, and therefore they result in similar mean values, μ. Table 5.1 lists the fitting parameters (μ and σ), and quality of fit (χ^2/υ) for these fits. It should be noted that for the log-normal distribution the given mean, μ, and standard deviation, σ have been calculated to represent the measured data and are not μ and σ of the underlying normal distribution in log space. This distinction is further explained in the appendix (section 8.2).

High Liquid Level, Number of nanosheets measured: 428				
Chosen Fit	Mean, μ / nm	Median /nm	Standard Deviation, σ /nm	χ^2/υ
Normal	108	108	24	2.845
Log-Normal	112	109	26	0.494
Low Liquid Level, Number of nanosheets measured: 220				
Chosen Fit	Mean, μ / nm	Median / nm	Standard Deviation, σ / nm	χ^2/υ
Normal	226	226	27	2.512
Log-Normal	228	227	26	5.529
Stirred Solution, Number of nanosheets measured: 595				
Chosen Fit	Mean, μ / nm	Median / nm	Standard Deviation, σ / nm	χ^2/υ
Normal	284	284	59	8.060
Log-Normal	295	288	63.4	1.749

Table 5.1: The results of fitting nanosheet lateral width data with both a normal and a log-normal fit. These fitting parameters correspond to the plots shown in figure 5.4. The fits relate to data sets which were collected from TEM micrograph analysis of the Bi_2Te_3 nanosheets deposited from aliquots taken from the high liquid level, low liquid level and following stirring of a $K_{0.8}Bi_2Te_3$ /NMP solution.

The differences between the normal and log-normal fitting parameters for each dataset are considered insignificant as they are either smaller or approximately equal to the estimated error in the lateral width measurement ($\pm$ 10 nm). The χ^2/υ values provide no consistent preference for a particular fit, with χ^2/υ values for each fit similarly small except for the 'stirred solution' dataset which shows a greater improvement in fit for the log-normal distribution.

It was concluded that the datasets would be fitted with a normal distribution as there was minimal skewness of the data, such that the difference found between

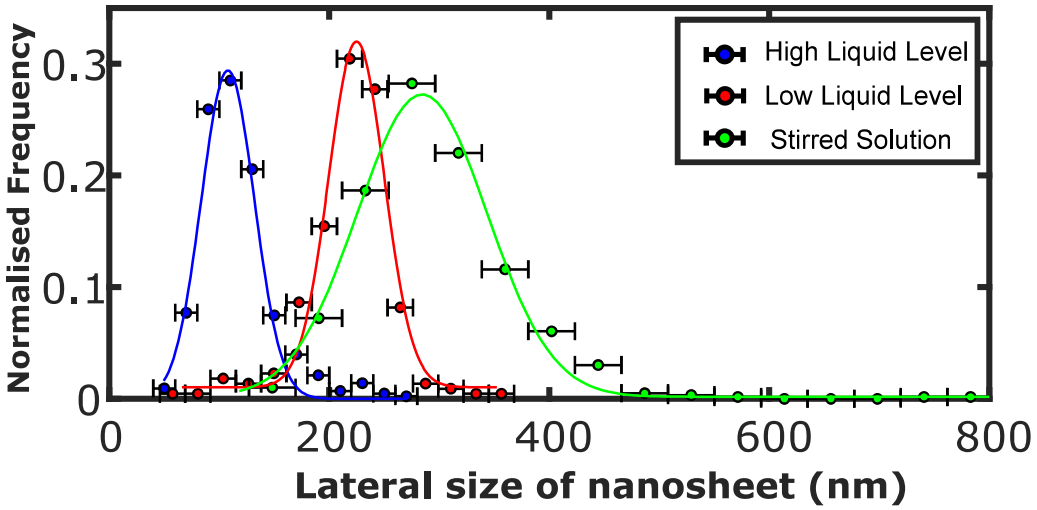

Figure 5.5: The datasets collected during the TEM study of nanosheets deposited from aliquots removed from the high liquid level, low liquid level and following stirring for a $K_{0.8}.Bi_2Te_3$ NMP solution, aged 5 days. The binned data, which has been normalised to sample size, is plotted with with error bars representing histogram bin width and has been fitted with a normal distribution for each sample.

the mean values of each fit was not significant enough to justify use of the log-normal distribution. It should also be noted that the normal distribution allows intuitive and unambiguous description of the data, whilst there is the added complexity of defining the data with a log-normal distribution with either the mean, mode or median.

5.1.3 Experimental Results

The three datasets can be seen in figure 5.5, which shows the frequency size distribution of the measured lateral width of Bi_2Te_3 nanosheets dropcast from solution and imaged using TEM (the data has been normalised to sample size). Each dataset has been fitted with a normal distribution. Details of the resulting fitting parameters, along with the measure of goodness of fit, χ^2/υ, are displayed in table 5.1.

As seen in figure 5.5, there is a range of nanosheet diameters present in solution dependent on liquid depth. Nanosheets with smaller lateral dimension were found at higher liquid depths and nanosheets with larger lateral dimension were found at lower liquid depth. From the stirred liquid sample data it can be seen that, as expected, nanosheets with a wide range of sizes were collected.

It is interesting to note that the standard deviation, σ, for the lower liquid sample and higher liquid sample are similar.

Whilst the stirred liquid sample data overlaps that of the higher and lower liquid fractions, it also extends beyond the lower liquid sample into greater sheet sizes (the largest measured sheet width was 1390 nm). This is likely to be a result of the low liquid aliquot not being removed from the lowest depth possible, in an attempt to avoid disturbing undissolved solid at the base of the vial which would obscure imaging, therefore not capturing the largest, low-lying sheets. However, it is also possible that the action of stirring may provide the required energy to aid the exfoliation of the larger sheets that had yet to exfoliate during the relatively short solution lifetime (5 days).

5.2 Investigating Nanosheet Dimensions with AFM

AFM was used to support and extend the investigation to include the measurement of nanosheet thickness, as well as lateral width, and to profile a more diverse range of samples. A range of nanosheet solutions were sampled to study the influence of certain factors on the nanosheet dimension, the chosen variables were: liquid depth; solution age; and relative concentration of alkali metal to layered material.

5.2.1 Experimental Details

AFM was employed to investigate the lateral width and thickness of deposited Bi_2Te_3 nanosheets. Solutions were created using potassium intercalated Bi_2Te_3 powders with varying metal intercalant stoichiometries and numerous AFM samples were created by drop casting an aliquot removed from either the high liquid level or the lower liquid level at timed intervals.

5.2.1.1 Preparation of Solutions and AFM Samples

The solutions were prepared by addition of 5 mL of dried NMP solvent to 0.0080 g of the chosen intercalated powder within a glass vial. For the more extensive AFM investigation larger volume samples required as multiple samples would be taken

over the age of the sample. The chosen powders were $K_{0.1}.Bi_2Te_3$, $K_{0.2}.Bi_2Te_3$, $K_{0.8}.Bi_2Te_3$, and $K_{1.5}.Bi_2Te_3$, therefore 5 solutions were produced in total. The solutions were left unperturbed in an argon filled glovebox until the chosen time for AFM sample preparation.

AFM samples were prepared following the typical dropcast method (described in section 3.2.5) using aliquots taken from different liquid depths (from either the higher liquid depth or lower liquid depth) across a number of weeks following the initial creation date of each solution. All sample preparation was carried out in the inert atmosphere of an argon filled glovebox. Although the AFM was conducted in air, the effects were minimised by ensuring all samples were prepared on the morning of the experiment and only removed from the inert atmosphere of the glovebox immediately before measurement.

5.2.1.2 AFM Data Collection

Once prepared on the mica substrates, the AFM samples were measured using tapping mode AFM. Despite the lack of coupled techniques present during AFM measurement (unlike the coupling of TEM with EDX and SAED), nanosheets were easily and reliably identified using their distinctive characteristics, as understood from extensive TEM studies prior to this experiment.

In tapping mode AFM, as well as recording the amplitude of tip oscillation, the phase of the resonating tip is also recorded. Whilst there was no chemical characterisation of the nanosheet during AFM measurement this tip phase information can provide useful insight into the AFM sample, as the phase shift of the oscillating tip is influenced by the chemical character of the material beneath the tip, therefore enabling material surfaces to be differentiated.

Although numerous AFM samples were prepared and characterised, only samples datasets with a minimum count of 90 nanosheets will be presented. Table 5.2 details the AFM samples for which a sufficiently large dataset was collected. The datasets have been grouped by the variable of interest within each investigation (variation of intercalant stoichiometry, solution age or liquid depth). The discussion of experimental results will follow the same grouping.

Variable	Details of AFM Sample		
	Intercalated Powder	Solution Age / weeks	Liquid Depth of Aliquot Removal
Intercalant Stoichiometry	$K_{0.2}.Bi_2Te_3$	6	High
	$K_{0.8}.Bi_2Te_3$	6	High
	$K_{1.5}.Bi_2Te_3$	6	High
Solution Age	$K_{0.2}.Bi_2Te_3$	1	High
	$K_{0.2}.Bi_2Te_3$	1.5	High
	$K_{0.2}.Bi_2Te_3$	6	High
	$K_{0.2}.Bi_2Te_3$	12	High
	$K_{0.8}.Bi_2Te_3$	2	High
	$K_{0.8}.Bi_2Te_3$	6	High
	$K_{0.8}.Bi_2Te_3$	18	High
Liquid Depth	$K_{0.2}.Bi_2Te_3$	6	Low
	$K_{0.2}.Bi_2Te_3$	6	High
	$K_{0.8}.Bi_2Te_3$	2	Low
	$K_{0.8}.Bi_2Te_3$	2	High

Table 5.2: Details of AFM samples from which large datasets (more than 90 nanosheets counted) were successfully collected. The datasets have been grouped by the variable of interest within the investigation: variation of intercalant stoichiometry, solution age and liquid depth.

5.2.1.3 AFM Micrograph Analysis

When examining the collected AFM data, thousands of nanosheets were identified and the lateral width and average height above the substrate surface was recorded for each individual nanosheet. The AFM micrographs were processed and analysed using the commercially available software (Gwyddion).

The identification of nanosheets based on their distinct morphology as well as interpretation of the phase information of the resonating tip is demonstrated in figure 5.6. The figure shows a typical AFM height image where features may be reliably identified as Bi_2Te_3 nanosheets as they are hexagonal in shape and relatively flat. It is interesting to note that the dried particles exhibit self-assembly, displaying collective patterns unique to tessellating hexagonal sheets.

Whilst the nanosheets are apparent it can also be seen that there is material collected at the sheet edges and sheet centres at a greater height above the substrate surface. It is suggested that this material is related to the residual, possibly polymerised [154], solvent which is brushed to the sheet edges by the action of the rastering tip. Such residual solvent and other possible contaminant

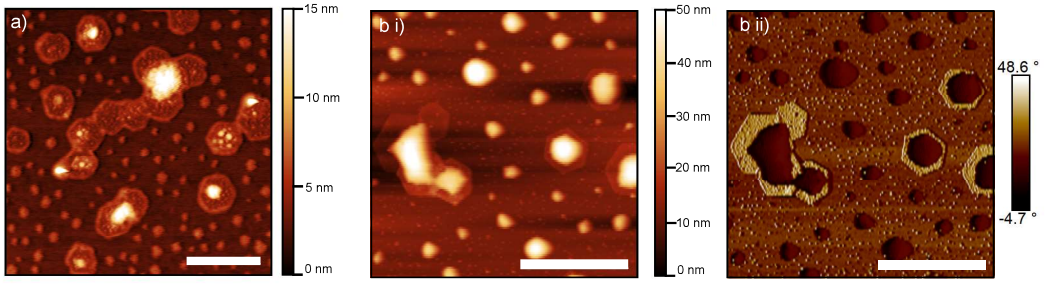

Figure 5.6: The identification of nanosheets and information collected in tapping mode AFM. Image a) shows self-assembled hexagonal nanosheets deposited from a $K_{0.2}.Bi_2Te_3$/ NMP solution (scale bar equal to 500 nm). Images bi) and bii) were collected from a $K_{0.8}.Bi_2Te_3$ /NMP solution and show the height and phase information which were collected simultaneously for the same sample area (scale bars equal to 2 µm).

particles can make nanosheet identification, in particular edge definition, difficult.

Fortunately, the comparison of the height images and phase shift images provides enough information to identify nanosheets and distinguish their edge. This principle is demonstrated in figure 5.6, whilst contrast in the height image is distorted by the tall contaminant features, in the phase image the nanosheets are clearly defined. With this in mind, both the height image and phase information were used when identifying the nanosheets and defining their edges.

The nanosheet measurement technique is demonstrated in figure 5.7. The lateral width of the nanosheets was defined and measured in the same way as was applied to the TEM images: by encircling the sheets and then recording the diameter of the circle. The following protocol was used to ascertain nanosheet thickness:

- flatten the image to give an approximately flat, equal background level for the mica substrate;
- select a line of data points that intersect the nanosheet;
- plot the height profile from the selected data points;
- fit a horizontal line, by eye, to the background (substrate) level of height profile;
- fit a horizontal line, by eye, to the average height of the nanosheet;

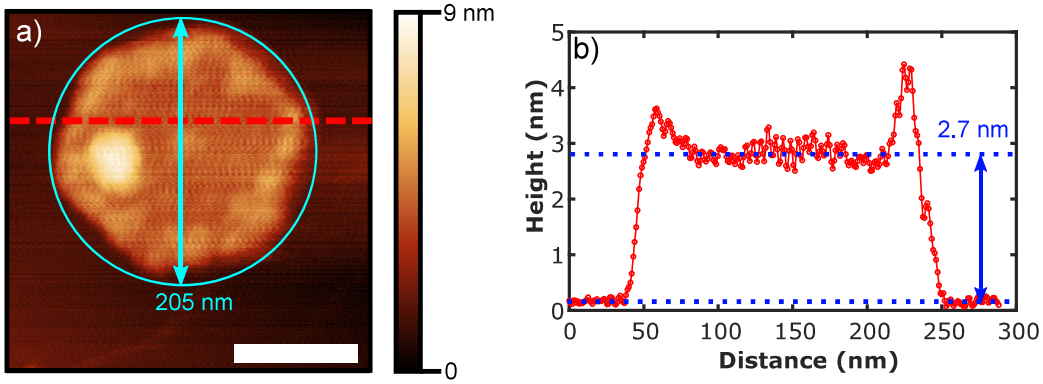

Figure 5.7: The method of measuring the lateral width and height of each nanosheet from height images collected during tapping mode AFM. Image a) is a height image of a nanosheet deposited from a 1 week old $K_{0.2}.Bi_2Te_3$ / NMP solution with scale bar equal to 100 nm, the nanosheet has been encircled to give a lateral width meausrment of 205 nm. Plot b) shows the height profile from the line of selected data points, with the average nanosheet height of 2.7 nm.

- calculate particle height by finding the difference between the two horizontal line fits.

5.2.1.4 Error Consideration

As with TEM, the main source of error in the determination of nanosheet lateral width from AFM images is related to the encircling of the hexagon, the approximate value given to this error is ± 10 nm. This assumes the error minimisation by appropriate choice of 'image resolution' (density of sample points within scan area, given by number of raster lines and samples per line scan).

The main source of error in the sample height measurement is the determination of the substrate level and nanosheet height in the height profile by eye. This process is complicated by the nanosheet surface roughness, presence of solvent residue and contaminant particles layered on the deposited nanosheets, but it is also distorted by artefacts introduced by image flattening in the AFM software.

Conducting the AFM experiment in ambient conditions also introduces errors related to the degradation of the deposited nanosheets in air. Figure 5.8 demonstrates the result of exposing a prepared AFM sample to air for an extended period of time. AFM height image a) was collected from a $K_{0.8}.Bi_2Te_3$ /NMP sample during normal sample measurement (AFM samples are exposed to air for the duration of mesurement, in this example: 3 hours of air exposure). AFM height image b) was collected from an AFM sample prepared from the same solution but was

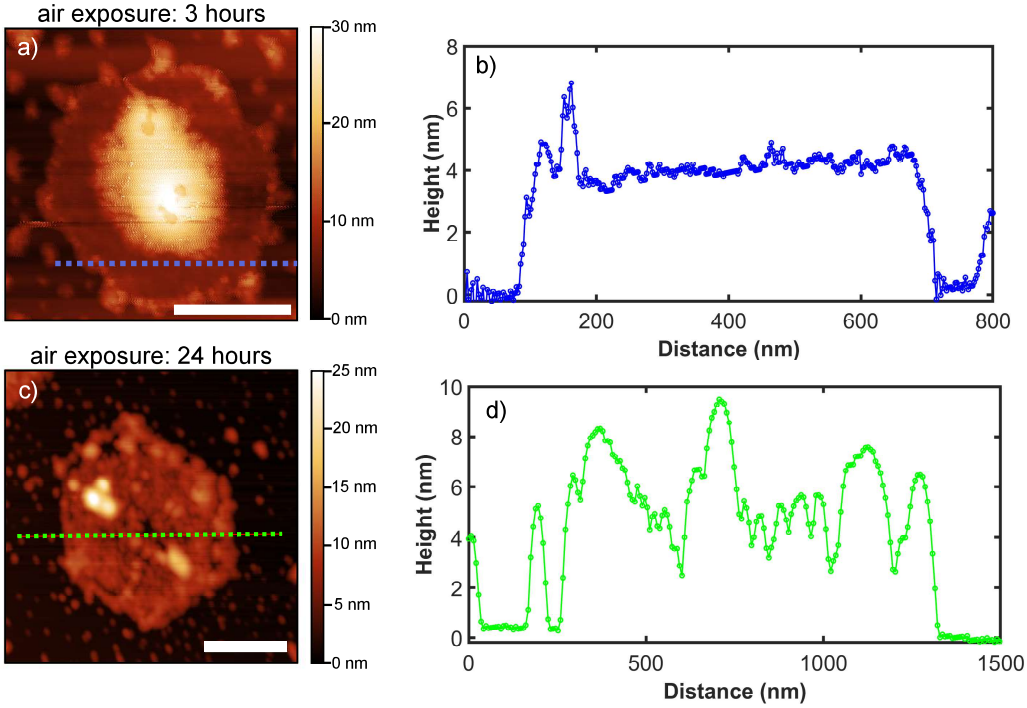

Figure 5.8: The influence of air exposure on the deposited nanosheets when observed using tapping mode AFM in ambient conditions. AFM height image a) shows a nanosheet which has been exposed to air for 3 hours and height profile b) from the selected line of data points. AFM height image c) shows a nanosheet which has been exposed to air for 24 hours and height profile d) from the selected line of data points shows increased roughness. Samples were prepared using a 6 week old $K_{0.8}.Bi_2Te_3$ /NMP solution. Scale bars represent 500 nm.

subjected to 24 hours of air exposure before measurement. Whilst the air exposed nanosheet still has the distinctive hexagonal shape, it has an increased surface roughness, this is likely to be a result of chemical reaction of the nanosheet in air, leading to significant destruction of the sheet surface.

Despite the evident negative impact of measuring AFM samples in ambient conditions, it was confirmed that there was no measurable increase in the nanosheet height or roughness due to air exposure over the time period of AFM sample measurement (typically 5 hours duration).

Numerous locations across the area of the 1 cm x 1 cm mica substrate were imaged for each sample and no correlation was found between the imaging location and the nanosheet dimensions. However, it should be noted that some locations, in particular those nearest to the solvent drying rings which were visible on the mica surface, were disregarded due to their large amount of solvent residue or very thick particles which risked the integrity of the tip, this may lead to distortion of the reported data.

All factors considered, the estimated error introduced by the height determination method is $\pm$ 0.1 nm. It is believed that the measured height is an overestimate of the true nanosheet thickness.

5.2.2 Analysis of Nanosheet Dimensions Data

The nanosheet dimensions extracted from the AFM micrographs were analysed further by creating a histogram for both the measured lateral widths and measured nanosheet heights of each AFM sample. The choice of an appropriate fit for the datasets was considered, and fitting allowed further description, insight and comparison of the datasets.

5.2.2.1 Creating Histograms

A histogram was constructed for each AFM sample dataset (both nanosheet lateral width and thickness). The bin width applied in each histogram was based upon Scott's normal reference rule [152] and the estimated error in the measurement. This method of calculating the bin width is described in the analysis of TEM data given in section 5.1.2. In the case of the AFM data analysis, a fixed minimum bin width of 20 nm was applied to the nanosheet lateral dimension data, and a

fixed minimum bin width of 0.2 nm was applied to the nanosheet thickness data.

5.2.2.2 Choice of Statistical Model

Due to the volume of data collected during the more extensive AFM investigation the choice of statistical model for fitting the histograms was revisited. This was tested by fitting the histograms to both normal and log-normal distributions and comparing the resulting fitting parameters, as well as the goodness of fit. These two distributions are discussed in more detail in the appendix, section 8.2.

The goodness of the fit was evaluated using chi-squared, χ^2, analysis. Details of the chi-squared test may be found in the appendix, section 8.3. The fit is considered good if the χ^2/υ value is equal to 1 and the fit is considered unacceptable if $\chi^2/\upsilon \gg 1$ or $\chi^2/\upsilon \ll 1$. For this work a χ^2/υ value less than 10 was considered an acceptable fit and all fits were found to satisfy this criteria.

Similar results were achieved for the fitting parameters (μ and σ) when fitting the data using the log-normal distribution and the normal distribution, and the goodness of fit, χ^2/υ, did not indicate a preference for either fit. Whilst the mean of the normal distribution is easy to interpret and serves as an intuitive representation of the data, along with the standard deviation, it is not quite as simple to find two analogous parameters for the log-normal distribution that provide an intuitive representation of the data. This is because the log-normal distribution is skewed, so that the majority of the data is less than the mean value of the distribution. With these points considered, it was decided that the datasets would be fitted using a normal distribution.

5.2.3 Experimental Results

Experimental Results may be considered in relation to the three main areas of investigation: variation of intercalation stoichiometry, solution age, and liquid depth. The results for the AFM study of dimensions of deposited nanosheets will be discussed in relation to these variables and then the results considered collectively across all the samples studied. The influence of air exposure on the prepared AFM sample will also be discussed further.

5.2.3.1 Variation of Intercalation Stoichiometry

The results of the investigation into nanosheets deposited from solutions prepared from intercalated powders with differing metal concentration are summarised in figure 5.9. AFM samples were prepared using NMP solutions of $K_{0.1}.Bi_2Te_3$, $K_{0.2}.Bi_2Te_3$, $K_{0.8}.Bi_2Te_3$, and $K_{1.5}.Bi_2Te_3$, after ageing for six weeks. It should be noted that no nanosheets were found in the AFM sample created from the $K_{0.1}.Bi_2Te_3$ solution, as in agreement with the lack of nanosheets found in the TEM study of this sample (data presented in section 4.3.2).

Each dataset has been fitted with a normal distribution. The resulting fitting parameters, along with the measure of goodness of fit, χ^2/υ, are displayed in table 5.3.

The study shows that the nanosheets deposited from solution of $K_{0.8}.Bi_2Te_3$ had a greater distribution of lateral widths, greater average width and greater average thickness than the nanosheets deposited from solution of $K_{0.2}.Bi_2Te_3$. Whilst the nanosheets deposited from $K_{1.5}.Bi_2Te_3$ solution were found to have similar average thickness to the nanosheets deposited from $K_{0.8}.Bi_2Te_3$ solution they were found to have a lower average lateral width which is likely to be related to the material damage as a result of the higher metal concentration during intercalation. This result agrees with the damage evident in the TEM characterisation of nanosheets deposited from the $K_{1.5}.Bi_2Te_3$ solution, as shown in section 4.3.2.

Sample Properties		Normal Fit Properties					
		Nanosheet Lateral Width			Nanosheet Thickness		
Intercalated Powder	Number of nanosheets measured	Mean (μ) / nm	Std. Dev (σ) / nm	χ^2/υ	Mean (μ) / nm	Std. Dev (σ) / nm	χ^2/υ
$K_{0.2}.Bi_2Te_3$	596	236	32.9	7.850	2.42	0.33	8.133
$K_{0.8}.Bi_2Te_3$	91	907	250	0.778	4.24	0.56	4.677
$K_{1.5}.Bi_2Te_3$	319	269	71	2.576	3.95	1.15	8.047

Table 5.3: AFM study of nanosheets deposited from high liquid level aliquots of solutions of $K_{0.2}.Bi_2Te_3$, $K_{0.8}.Bi_2Te_3$, and $K_{1.5}.Bi_2Te_3$ in NMP. This table provides the fitting parameters resulting from the fitting the nanosheet thickness and nanosheet lateral width with a normal distribution, as presented in figure 5.9.

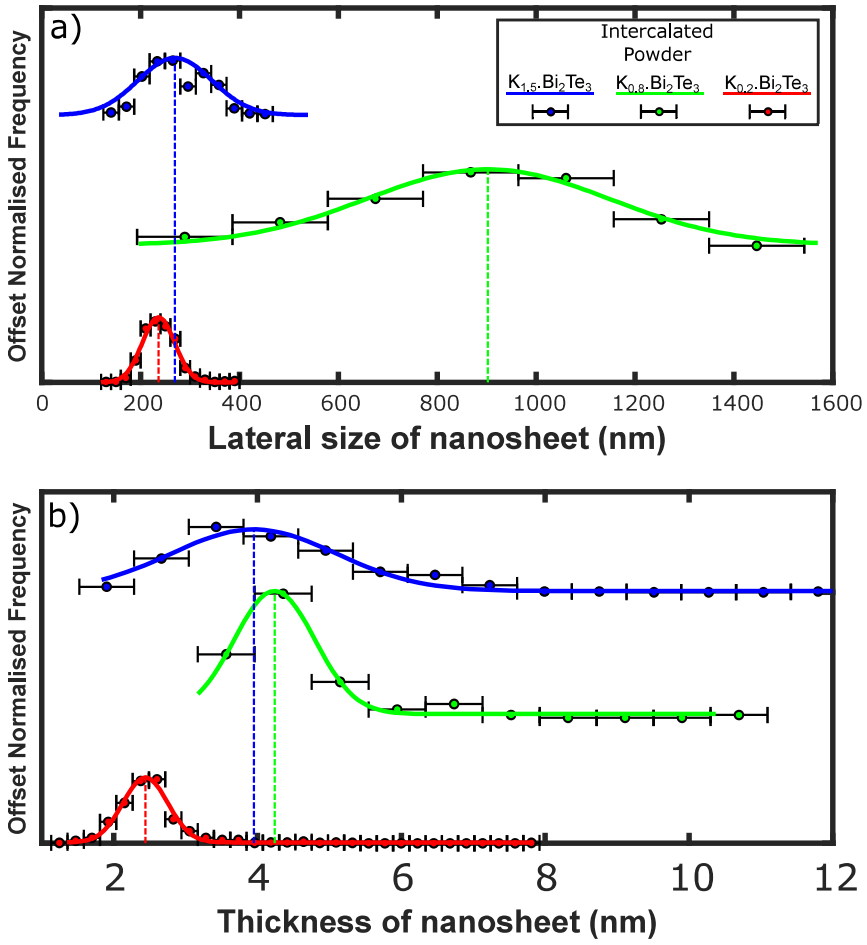

Figure 5.9: atasets collected during the AFM study of the nanosheets deposited from high liquid level aliquots of $K_{0.2}.Bi_2Te_3$, $K_{0.8}.Bi_2Te_3$, and $K_{1.5}.Bi_2Te_3$ NMP solutions. The binned data, both thickness of nanosheet and lateral width of nanosheet, have been fitted with a normal distribution and their mean values, μ, are marked by a broken line.

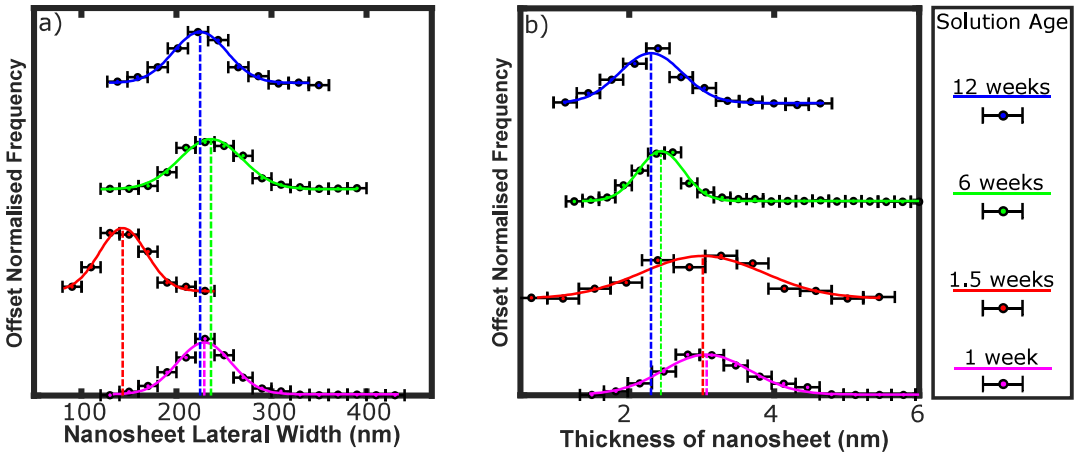

Figure 5.10: Datasets collected during the AFM study of the nanosheets deposited from high liquid level aliquots removed from a $K_{0.2}.Bi_2Te_3$ NMP solution at timed intervals over a 12 week period. The binned data, both thickness of nanosheet and lateral width of nanosheet, have been fitted with a normal distribution and their mean values, μ, are marked by a broken line.

5.2.3.2 Solution Age: $K_{0.2}.Bi_2Te_3$ Solutions

The results of the investigation into nanosheets deposited from aliquots removed from a $K_{0.2}.Bi_2Te_3$ NMP solution at timed intervals over a 12 week period are summarised in figure 5.10. Aliquots were removed from the high liquid level 1 week, 1.5 weeks, 6 weeks, and 12 weeks after initial solution preparation. Each dataset has been fitted with a normal distribution and the resulting fitting parameters, along with the measure of goodness of fit, χ^2/υ, are displayed in table 5.4. From the data collected there is a general trend for the average thickness

Sample Properties		Normal Fit Properties					
		Nanosheet Lateral Width			Nanosheet Thickness		
Solution Age / weeks	Number of nanosheets measured	Mean (μ) / nm	Std. Dev (σ) / nm	χ^2/υ	Mean (μ) / nm	Std. Dev (σ) / nm	χ^2/υ
1	433	229	28.5	1.609	3.05	0.56	5.334
1.5	253	143	24.9	1.165	3.01	0.83	2.317
6	596	236	32.9	7.850	2.42	0.33	8.133
12	229	225	28.3	0.562	2.31	0.45	0.443

Table 5.4: AFM study of nanosheets deposited from high liquid level aliquots removed from a $K_{0.2}.Bi_2Te_3$ NMP solution at timed intervals over a 12 week period. This table provides the fitting parameters resulting from the fitting the nanosheet thickness and nanosheet lateral width with a normal distribution, as presented in figure 5.10.

of the deposited nanosheets to decrease with the increasing age of the solution. Although the aliquot taken at a solution age of 1.5 weeks does not support the trend, the lateral width of the deposited nanosheets are fairly invariant, with an average lateral width of 230 nm width across the three samples. It is possible that the smaller lateral widths found for the sample prepared from the solution at the age of 1.5 weeks is an artefact of the AFM sampling method (strongly dependent on drying conditions) which may distort the results, but it should be noted that the range of lateral widths recorded for all samples is similar even though the mean width differs.

5.2.3.3 Solution Age: $K_{0.8}.Bi_2Te_3$ Solutions

The results of the investigation into nanosheets deposited from aliquots removed from a $K_{0.8}.Bi_2Te_3$ NMP solution at timed intervals over a 18 week period are summarised in figure 5.11. Aliquots were removed from the high liquid level at 2 weeks, 6 weeks, and 18 weeks after initial solution preparation. Each dataset has been fitted with a normal distribution and the resulting fitting parameters, along with the measure of goodness of fit, χ^2/υ, are displayed in table 5.5.

The collected data suggests that the average thickness of the nanosheets deposited decreases with the increasing age of the solution. The data may also suggest that the average lateral width of the nanosheets deposited is variable with the age of the solution, with a general trend of increasing over time as a result of gradual diffusion of larger material to the high liquid level. However, more data should be collected before these trends can be confirmed.

Sample Properties		Normal Fit Properties					
		Nanosheet Lateral Width			Nanosheet Thickness		
Solution Age / weeks	Number of nanosheets measured	Mean (μ) / nm	Std. Dev (σ) / nm	χ^2/υ	Mean (μ) / nm	Std. Dev (σ) / nm	χ^2/υ
2	176	596	192	9.182	4.44	1.17	1.115
6	91	907	250	0.778	4.24	0.56	4.678
18	100	864	241	1.787	3.26	0.50	4.240

Table 5.5: AFM study of nanosheets deposited from high liquid level aliquots removed from a $K_{0.8}.Bi_2Te_3$ NMP solution at timed intervals over a 18 week period. This table provides the fitting parameters resulting from the fitting the nanosheet thickness and nanosheet lateral width with a normal distribution, as presented in figure 5.11.

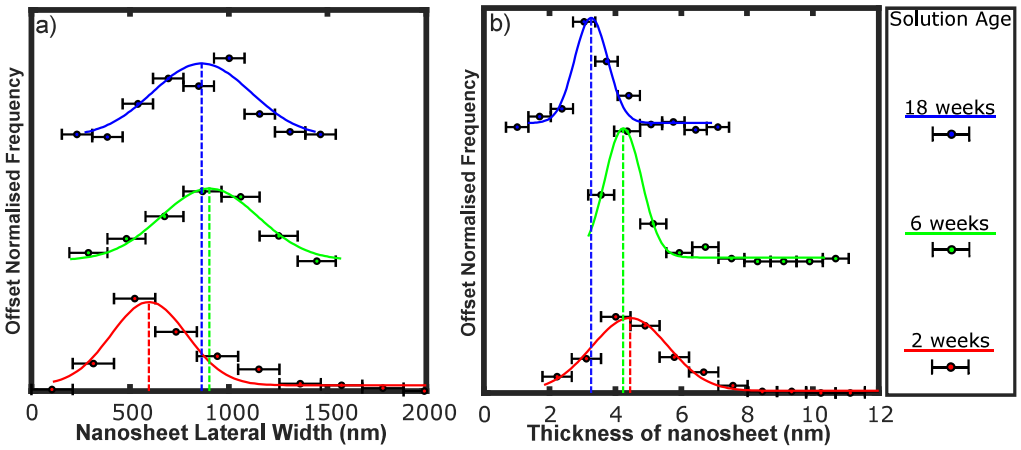

Figure 5.11: Datasets collected during the AFM study of the nanosheets deposited from a high liquid level aliquots removed from a $K_{0.8}.Bi_2Te_3$ NMP solution at timed intervals over a 18 week period. The binned data, both thickness of nanosheet and lateral width of nanosheet, have been fitted with a normal distribution and their mean values, μ, are marked by a broken line.

5.2.3.4 Liquid Depth: $K_{0.2}.Bi_2Te_3$ Solutions

The results of the investigation into nanosheets deposited from aliquots removed from the low liquid level and the high liquid level of a $K_{0.2}.Bi_2Te_3$ NMP solution, aged 6 weeks, are summarised in figure 5.12. Each dataset has been fitted with a normal distribution and the resulting fitting parameters, along with the measure of goodness of fit, χ^2/υ, are displayed in table 5.6. A study of the stirred solution, analogous to the TEM study of section 5.1, was attempted but could not be replicated due to the increased presence of large particles of undissolved powder, leading to unfavourable conditions for AFM analysis.

The average lateral width of nanosheets deposited from the high and low liquid level aliquots were found to be in agreement, with little difference between the distribution of the data. Although there was a small difference found between the thickness of the deposited nanosheets from the different liquid levels this difference cannot be considered statistically significant. Thus this study seems to find the nanosheets distributed throughout the liquid volume of the 6 week old $K_{0.2}.Bi_2Te_3$ NMP solution to be fairly invariant. Invariance of nanosheet lateral width is in agreement with the invariance in lateral width of the nanosheets collected in the age study of the $K_{0.2}.Bi_2Te_3$ NMP solution.

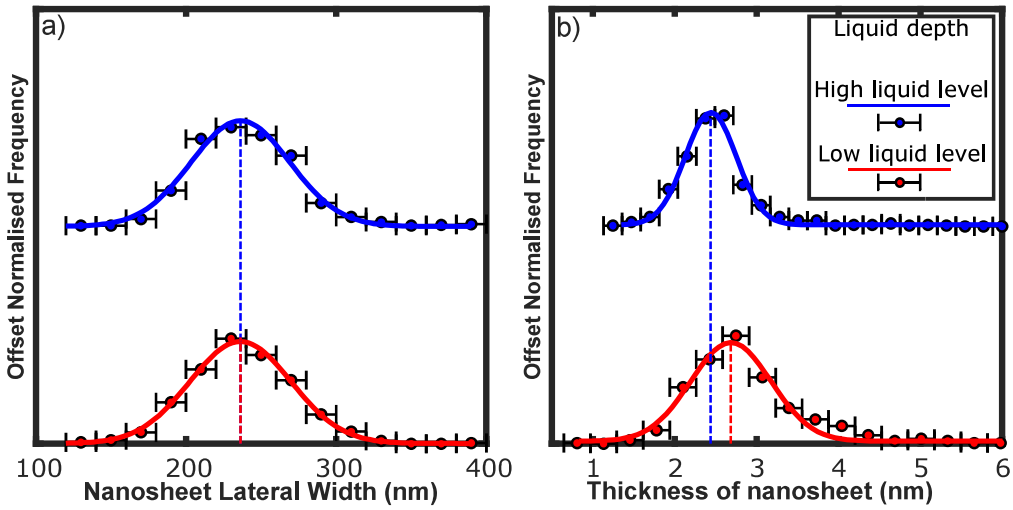

Figure 5.12: Datasets collected during the AFM study of the nanosheets deposited from aliquots removed from the low liquid level and the high liquid level of a $K_{0.2}.Bi_2Te_3$ NMP solution, aged 6 weeks. The binned data, both thickness of nanosheet and lateral width of nanosheet, have been fitted with a normal distribution and their mean values, μ, are marked by a broken line.

Sample Properties		Normal Fit Properties					
		Nanosheet Lateral Width			Nanosheet Thickness		
Sampling Depth	Number of nanosheets measured	Mean (μ) / nm	Std. Dev (σ) / nm	χ^2/υ	Mean (μ) / nm	Std. Dev (σ) / nm	χ^2/υ
High	596	236	32.9	7.850	2.42	0.33	8.133
Low	608	236	34	0.444	2.70	0.51	11.078

Table 5.6: AFM study of nanosheets deposited from aliquots removed from the low liquid level and the high liquid level of a $K_{0.2}.Bi_2Te_3$ NMP solution, aged 6 weeks. This table provides the fitting parameters resulting from the fitting the nanosheet thickness and nanosheet lateral width with a normal distribution, as presented in figure 5.12.

5.2.3.5 Liquid Depth: $K_{0.8}.Bi_2Te_3$ Solutions

The results of the investigation into nanosheets deposited from aliquots removed from the low liquid level and the high liquid level of a $K_{0.8}.Bi_2Te_3$ NMP solution, aged 2 weeks, are summarised in figure 5.13. Each dataset has been fitted with a normal distribution and the resulting fitting parameters, along with the measure of goodness of fit, χ^2/υ, are displayed in table 5.7.

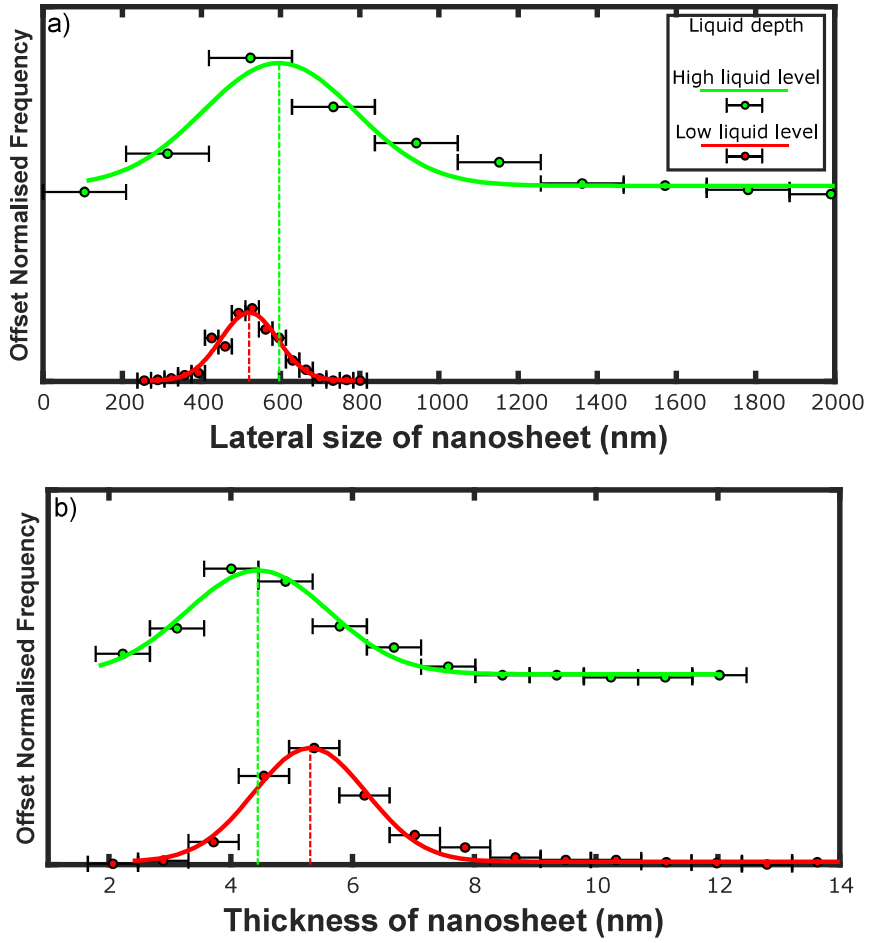

Figure 5.13: Datasets collected during the AFM study of the nanosheets deposited from aliquots removed from the low liquid level and the high liquid level of a $K_{0.8}.Bi_2Te_3$ NMP solution, aged 2 weeks. The binned data, both thickness of nanosheet and lateral width of nanosheet, have been fitted with a normal distribution and their mean values, μ, are marked by a broken line.

Whilst there is a difference found between the data collected for the lateral width and thickness of deposited nanosheets from the different aliquot sampling depths, considering the standard deviation of the data, these differences are not significant. In particular the distribution of the lateral widths found with the high liquid level aliquot sample, includes that of the narrower distribution for the low liquid level sample. This data is not in agreement with the distinct depth dependence of lateral width found within the TEM study (section 5.1).

Sample Properties		Normal Fit Properties					
		Nanosheet Lateral Width			Nanosheet Thickness		
Sampling Depth	Number of nanosheets measured	Mean (μ) / nm	Std. Dev (σ) / nm	χ^2/υ	Mean (μ) / nm	Std. Dev (σ) / nm	χ^2/υ
High	176	596	192	9.182	4.44	1.17	1.115
Low	482	521	72	2.179	5.30	0.93	7.349

Table 5.7: AFM study of nanosheets deposited from aliquots removed from the low liquid level and the high liquid level of a $K_{0.8}.Bi_2Te_3$ NMP solution, aged 2 weeks. This table provides the fitting parameters resulting from the fitting the nanosheet thickness and nanosheet lateral width with a normal distribution, as presented in figure 5.13.

5.2.3.6 Influence of Air Exposure on Observed Nanosheet Thickness

Sample Properties		Normal Fit Properties					
		Nanosheet Lateral Width			Nanosheet Thickness		
Sample Air Exposure / hours	Number of nanosheets measured	Mean (μ) / nm	Std. Dev (σ) / nm	χ^2/υ	Mean (μ) / nm	Std. Dev (σ) / nm	χ^2/υ
3	91	907	250	0.778	4.24	0.56	4.678
24	111	914	224	0.208	8.18	2.10	1.901

Table 5.8: AFM study of nanosheets deposited from aliquots removed from the high liquid level of a $K_{0.8}.Bi_2Te_3$ NMP solution, aged 6 weeks. One sample had air exposure limited to the duration of AFM measurement, whereas the other sample was exposed to air for 24 hours before measurement. This table provides the fitting parameters resulting from the fitting the nanosheet thickness and nanosheet lateral width with a normal distribution, as presented in figure 5.14.

An investigation into the influence of air exposure on the prepared AFM sample was completed and the results are summarised in figure 5.14. The collected data was compared to a sample prepared from the same solution ($K_{0.8}.Bi_2Te_3$ in NMP, high liquid level, 6 weeks old) but with air exposure limited to the duration of AFM measurement. Each dataset has been fitted with a normal distribution and the

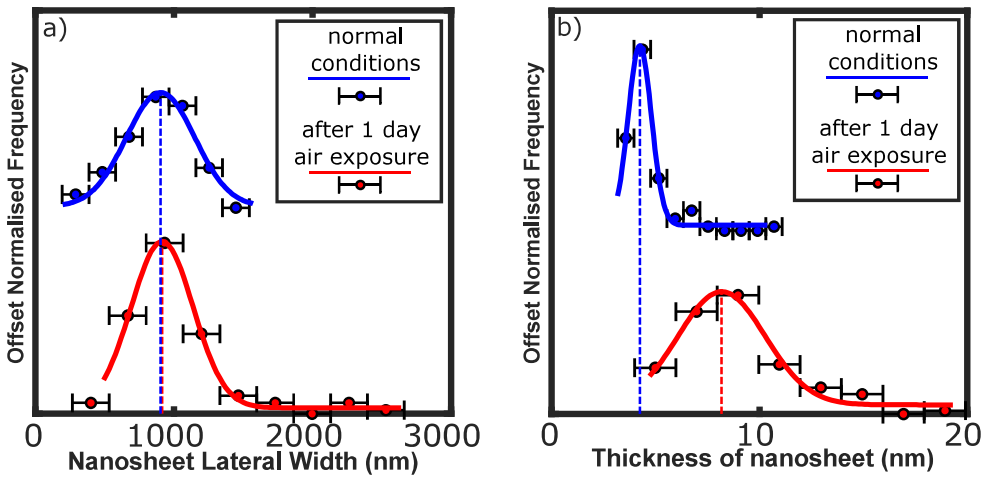

Figure 5.14: Datasets collected during the AFM study of the nanosheets deposited from a aliquots removed from the high liquid level of a $K_{0.8}.Bi_2Te_3$ NMP solution, aged 6 weeks. One sample had air exposure limited to the duration of AFM measurement (normal conditions), whereas the other sample was exposed to air for 24 hours before measurement. The binned data, both thickness of nanosheet and lateral width of nanosheet, have been fitted with a normal distribution and their mean values, μ, are marked by a broken line.

resulting fitting parameters, along with the measure of goodness of fit, χ^2/υ, are displayed in table 5.8. It was found that the mean nanosheet diameter was not significantly affected by 24 hours of air exposure but the measured nanosheet thickness was greatly increased due to the influence of air exposure.

5.2.4 Discussion of Experimental Results

One of the most distinct trends across the AFM study was the difference in the size of nanosheets collected from the $K_{0.2}.Bi_2Te_3$ solutions and the $K_{0.8}.Bi_2Te_3$ solutions. It can be seen that the nanosheets deposited from $K_{0.2}.Bi_2Te_3$ solutions were both smaller in average lateral width and thickness but also displayed little variation in mean nanosheet width and thickness with respect to liquid depth and solution age, unlike the nanosheets deposited from $K_{0.8}.Bi_2Te_3$.

Figure 5.15 includes two scatter plots summarising the AFM data collected for $K_{0.2}.Bi_2Te_3$, $K_{0.8}.Bi_2Te_3$ and $K_{1.5}.Bi_2Te_3$ solution samples (specifically high liquid level aliquots) across the solution age. The scatter plot shows the the average dimension, μ, calculated from fitting each dataset to a normal distribution with the

complete length of error bars representing the spread of data, using 2σ derived from fitting (equivalent to ~68 % confidence interval).

Although the increase in metal intercalant ratio seems to increase the average width of the deposited nanosheets, there is a limit to this effect. It is likely that the pnictogen chalcogenide layered compounds have a limited intercalation stoichiometry, related to their chemical character[155], and if the metal concentration present in metal ammonia solution exceeds this maximal ratio it will lead to reduction of the layered material. The extensive AFM results were consistent with this hypothesis, explored in section 4.3.2, that intercalation powders produced with metal ratios of 1.5 or greater led to nanosheets displaying appreciable degradation. This loss of structural integrity resulted in smaller average lateral width of the nanosheets deposited from the $K_{1.5}.Bi_2Te_3$ NMP solution.

To the best of the author's knowledge, there is no published data dedicated to determination of the maximum intercalation stoichiometry or intercalation chemistry of the pnictogen chalcogenide layered compounds. However, the discussion and interpretation of the experimental differences found between the nanosheets collected from the $K_{0.2}.Bi_2Te_3$ solutions and the $K_{0.8}.Bi_2Te_3$ solutions depends upon understanding of the intercalation chemistry of Bi_2Te_3. It is possible that the pnictogen chalcogenide layered compounds may exhibit a continuous interlcalation phase or perhaps preferred stoichiometries, known as staging; these two possibilities will be discussed in relation to the observed trends in the data.

Determining whether the pnictogen chalcogenide layered compounds exhibit a continuous interlcalation phase or stoichiometric phases is no trivial matter, and it is complicated further by the lack of discernible influence of intercalation on the XRD patterns of these materials [149][150] (unlike GICs or intercalated TMDs). Featureless discharge curves, with no plateau, found during the electrochemical lithium intercalation of Bi_2Te_3 [156][157], indicates that electrochemical study of the intercalation of the pnictogen chalcogenide layered compounds may not provide the desired insight into intercalation phase either.

Despite the lack of literature surrounding the intercalation chemistry of the pnictogen chalcogenide layered compounds, the results of this work seem to suggest that potassium intercalated Bi_2Te_3 compounds demonstrate a continuous intercalation phase. If this is the case, low alkali metal concentration during intercalation should lead to the same volume ratio of intercalated powder to unintercalated powder but with a lower density of intercalant and thus lower charge density compared to the high alkali metal ratio compounds. Spontaneous dissol-

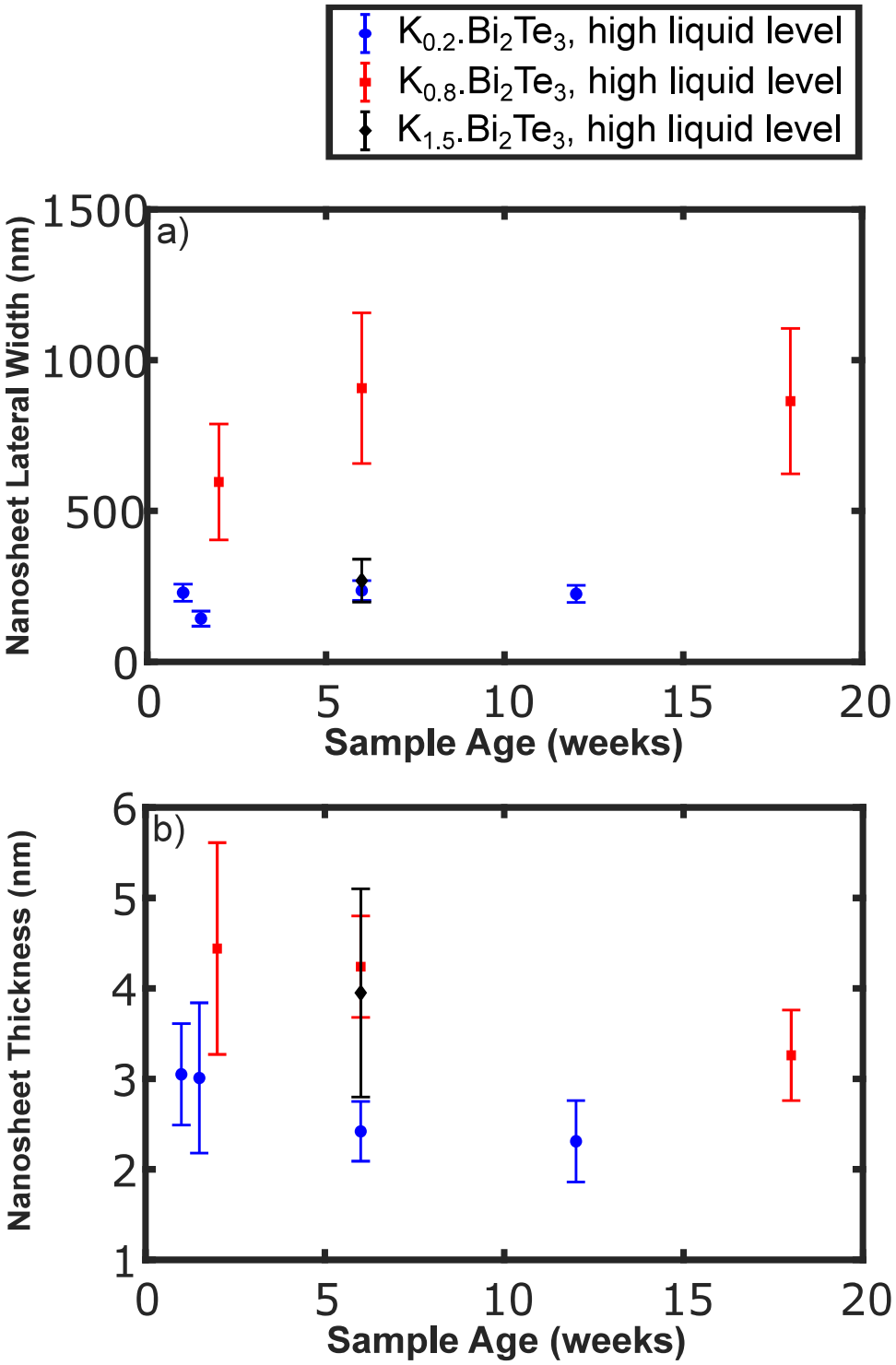

Figure 5.15: The average lateral width and thickness of the deposited nanosheets derived from the AFM study of $K_{0.2}.Bi_2Te_3$, $K_{0.8}.Bi_2Te_3$, and $K_{1.5}.Bi_2Te_3$ NMP solutions. Each data point represents the average dimension, μ, calculated from fitting the original dataset to a normal distribution. The complete length of error bars represent the spread of data and are equal to 2σ, as derived from fitting.

ution of nanosheets with a large width may not be favourable in the case of low charge density and this may be the reason that there is an observed lack of wider nanosheets in the $K_{0.2}.Bi_2Te_3$ samples. In summary, a continuous intercalation phase may lead to the restriction of lateral width of nanosheets deposited from solutions of lower intercalant ratio powders due to energetics of dissolution.

It should be reiterated that for the solution of the low metal intercalation compound, $K_{0.1}.Bi_2Te_3$, no nanomaterial was found within TEM or AFM study of the solution deposits. This is significantly different to the example of the $K_{0.2}.Bi_2Te_3$ deposits, although the nanosheets were limited in width there where large numbers of deposited nanosheets seen in these samples. This seems to further support the hypothesis that pnictogen chalcogenide layered compounds follow a continuous intercalation phase and that the charge density of $K_{0.1}.Bi_2Te_3$ may be too low for dissolution of nanosheets of any size.

If however, there was a preferred or fixed intercalation stoichiometry for the pnictogen chalcogenide layered compounds, similar to the staging found in GICs, then it would be expected that all intercalated material should share the same select intercalation stoichiometry with the difference in concentration of metal in the metal ammonia solution leading to a greater or lesser ratio of intercalated powder to unintercalated powder. If the intercalation of pnictogen chalcogenide layered compounds proceeds in this way this would lead to smaller grains of intercalated material within the $K_{0.2}.Bi_2Te_3$ powder compared to the $K_{0.8}.Bi_2Te_3$ powder and thus a smaller average size of solvated nanosheets for the $K_{0.2}.Bi_2Te_3$ solutions, as seen in the AFM study. Inductively coupled plasma mass spectrometry (ICP-MS) could be used in future experiments to investigate the true intercalant to material ratio of the intercalated powders and to test this hypothesis.

The AFM studies of the deposited nanosheets found that the nanosheets deposited from the $K_{0.2}.Bi_2Te_3$ solutions had a smaller average thickness than the nanosheets deposited from the $K_{0.8}.Bi_2Te_3$ solutions. If staging were to occur in these compounds where only some Bi_2Te_3 van der Waals gaps were filled, as in the case of higher GIC stages, it might be expected that the lower metal ratio compounds would produce thicker nanosheets [76]. However, this observed result may not be simply used to strengthen the argument for a continuous intercalation phase. Due to the observed influence of air exposure on the measured nanosheet thickness, it is believed that the increased thickness of the nanosheets deposited from the $K_{0.8}.Bi_2Te_3$ solutions may be related to their increased charge density and thus reactivity in air, along with the increased prevalence of contam-

inants in the case of the higher metal ratio compounds, which may also add to the measured thickness. Therefore making it difficult to confirm the possible trend.

It is interesting to note that the marked depth dependency of the nanosheet lateral widths observed in TEM studies was not reproduced in these AFM studies. There are a number of possible reasons for the lack of depth dependency in the AFM samples. The inability to effectively study the lower liquid depth samples (and complete inability to study the stirred liquids) due to the prevalence of tall features contributed by the undissolved powder will have affected the results. It is believed that this might have distorted the AFM results by restricting the sampling to the few areas where favourable drying conditions lead to sparse arrangements of isolated sheets. Whilst sheets could be measured even in the case of layering or presence of larger undissolved particles when using TEM this is not true for AFM.

It should also be noted the original TEM study was conducted using solutions aged only 5 days, compared to the low level aliquot removal from 2 and 6 week old solutions in the AFM study. It is possible that the the observed depth dependency of nanosheet size relates to the time taken for the solution to reach equilibration, determined by the size dependent kinetics of the exfoliation mechanism and the size dependence of nanosheet diffusion throughout the liquid volume. Whilst the same intercalation compounds and mass-to-volume ratio were used in the solution preparation for TEM and AFM studies, the solution volume was smaller in the TEM studies, 3 mL compared to 5 mL solutions for the AFM study. This is another reason why the datasets should not be directly compared.

These experimental differences were investigated by measuring the lateral width of nanosheets present in TEM samples prepared from 5 mL solutions, this data is compared in the plot in figure 5.16. Although the data only represents samples prepared from high liquid level aliquots, the TEM data from the 5 mL volume solutions was found to be in fair agreement with the lateral widths determined by the AFM data. Thus it was concluded that the depth dependency of lateral width is dependent on the age of solution, although further studies are required to confirm this.

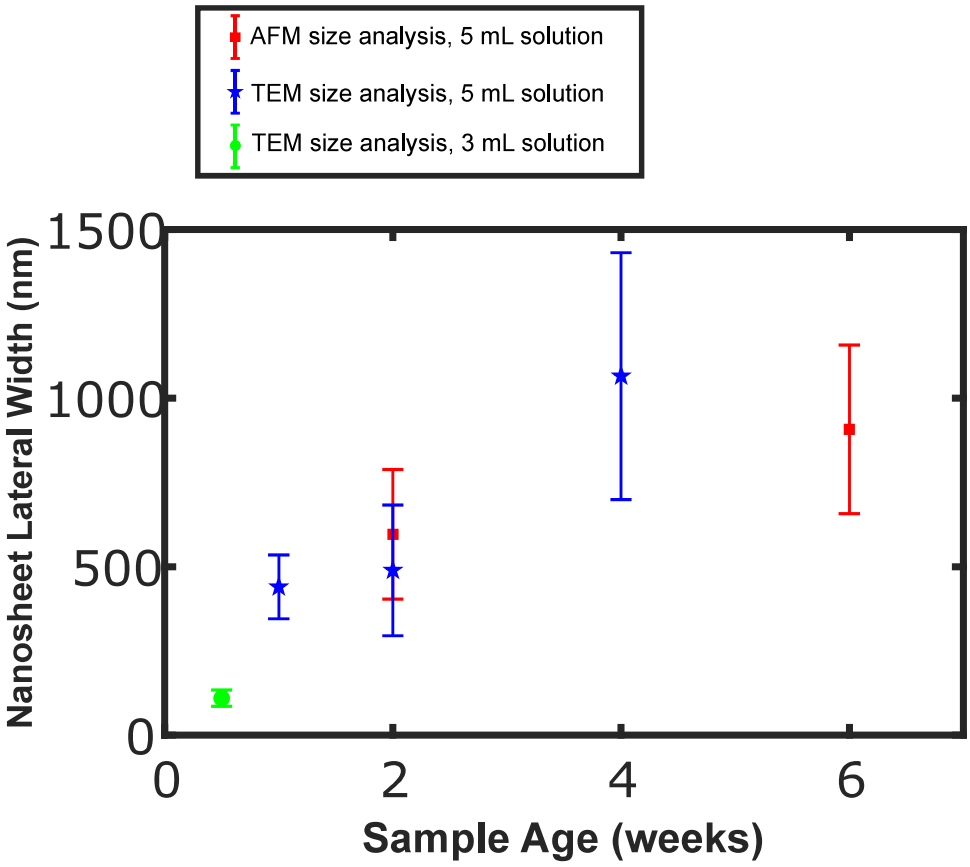

Figure 5.16: The average lateral width of the deposited nanosheets derived from the AFM and TEM study of $K_{0.8}.Bi_2Te_3$ NMP solutions. Each data point represents the average dimension, μ, calculated from fitting the original dataset to a normal distribution. The complete length of error bars represent the spread of data and are equal to 2σ, as derived from fitting.

5.3 Observing Nanosheets *in situ*: Liquid TEM

Whilst AFM and TEM provide great insight into the produced nanomaterial, the data suffers from drying artefacts. In contrast, liquid TEM allows visualisation of individual nanoparticles within their liquid environment, described as *in situ* observation. This technique has seen much advancement in recent years but even with improved micro-fabrication of the liquid cell components this is still a notoriously complicated and demanding experimental technique.

5.3.1 Insights from Preliminary Liquid TEM Experiments

Despite successfully assembling the liquid cell, flowing the nanosheet solution into the cell (without bursting the delicate silicon nitride windows) and observing the captured liquid using TEM numerous times, Bi_2Te_3 nanosheets were not observed during the liquid TEM experimental studies. Nor was any material found deposited on the cell components when investigated using with TEM and SEM after disassembling and drying the cell.

Although no nanomaterial was observed *in situ*, insight gained from these studies can inform future experimental design. It was noted that the solvent of choice, NMP, was highly electron absorbing leading to poor image resolution and difficultly in initially achieving focus (despite changing cell configuration to minimise liquid volume within the cell). The solutions were also found to be sensitive to beam damage, minimisation of the beam current was imperative as high beam currents or lingering on a small area of the cell would lead to complete irrecoverable loss of electron transparency (thought to be a result of beam induced chemical reaction).

During the studies there was concern about the introduction of contaminants or destabilisation of the solution due to the cleanliness of the liquid cell apparatus. Whilst the micro-fabricated liquid cell components were plasma cleaned and chemically resistant o-rings were used to seal the cell, the method of introducing the solution into the cell (comprising of a syringe connected to a length of ~30 cm capillary type plastic tubing) presented high probability of sample contamination. It should be noted that the introduction of solution via pipette prior to assembling the cell components, all within the inert atmosphere of a glovebox, was not possible due to the difficulty of chip alignment in the presence of liquid surface tension (only complicated further by wearing thick rubber gloves).

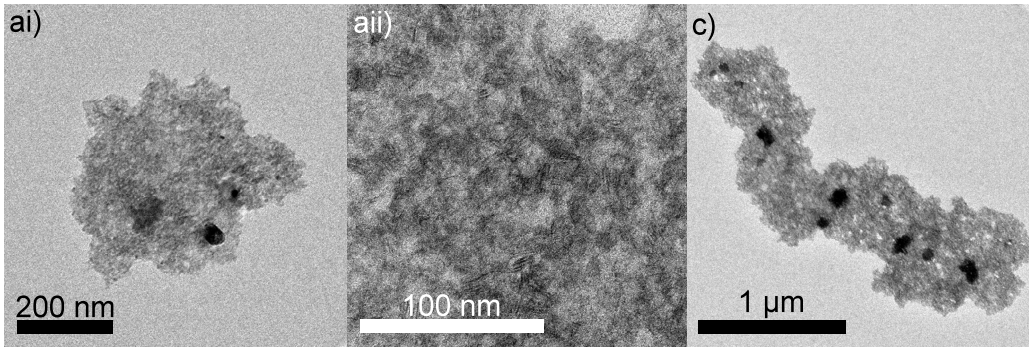

Figure 5.17: TEM images presenting material collected and dropcast from a $K_{0.8}.Bi_2Te_3$ / NMP solution after passing through the liquid TEM flow lines. Image ai) shows an amorphous particle, with further detail given in image aii). Image b) shows a chain-like aggregate of amorphous particles. Scale bars are provided and labelled accordingly.

Solution degradation, as a result of flowing liquid through the capillary tubes, was investigated by collecting the solution after its journey through the flow lines and dropcasting it onto a TEM grid. The only material found in this liquid was amorphous and aggregated, as shown in figure 5.17, which presents the amorphous material collected from the flow lines of the liq TEM holder after a $K_{0.8}.Bi_2Te_3$ in NMP solution was passed through the assembly. The particles did not give a diffraction pattern, although closer detail shows evidence of some structure to the particles. It is assumed that the degradation of the nanoparticles was the primary reason for lack of nanosheet observation. Further improvement of the liquid cell sample preparation is required before this becomes a viable technique for observing these nanosheet solutions.

5.4 Obtaining an Average Description of the Solution: SAXS

Scattering studies can provide an average description of the scattering material and therefore provide characterisation that is representative of the sample as a whole. In this study, SAXS has been employed to characterise the solution samples *in situ*. The detection of scattered x-rays can be used to indirectly determine the dimensions of nanosheets present in solution. Scattering studies were performed on a range of nanosheet solutions. Interpretation of this SAXS data relies upon the dimensional analysis conducted previously, using AFM data to substantiate a model of the scattering data. The complementary nature of the

in situ SAXS data and the *ex situ* AFM data also allows the impact of drying artefacts to be assessed.

5.4.1 Optimising SAXS Sample Preparation

Although multiple SAXS studies were completed, there is a limited body of useful scattering data due to initial difficulty in achieving appreciable scattering intensities from the prepared samples.

A variety of sample preparation methods were explored before appreciable sample scattering was achieved. Initial sample preparation involved the transfer of pre-made solutions to a capillary using a stainless steel needle and glass syringe, before wax sealing the capillary and measuring the sample scattering. Modifications to this preparation method included decanting higher concentration solutions; stringent cleaning of all equipment; sealing the capillary with a glue gun; and use of hot-wire to melt, fuse and seal the capillary within the glovebox. However, it was found that scattering data collected for the decanted solution samples was not greater than the solvent background and the solutions appeared to sediment within the capillaries over a period of days. It is possible that despite stringent sample preparation and cleaning of equipment (heating under vacuum for days) the solutions were destabilised during preparation due to the presence of contaminants and thus sample aggregation followed.

Instead an alternative, perhaps unorthodox, preparation method was used for the SAXS samples. Solutions were prepared directly within the capillary by placing a weighed mass of intercalated powder in the capillary before addition of solvent using a stainless steel needle and glass syringe. Such samples include undesirable, larger scatterers (the undissolved powder grains) as well as increased particle polydispersity due to the preparation of solution *in situ* rather than selection of a sample fraction via decanting. However, for the samples produced using this method, the scattering intensity was appreciable and, more crucially, interpretable.

Although the issue of weak scattering was overcome, there are still improvements to be made in finding the optimum sample concentration, allowing for appreciable scattering and individualised nanosheets. Only one of six capillary samples prepared by direct dissolution within the capillary demonstrated in the expected fractal dimension, D_f, for disc-shaped, two dimensional scatterers.

5.4.2 Modelling of SAXS Data

Analysis of the gradient found within the low Q region of the log(I)/log(Q) plot of SAXS data and application of the power law allows the fractal dimension to be determined. A fractal dimension, D_f, of 2 is expected for individualised disc-like objects, such as a dilute solution of nanosheets [131]. Whereas a D_f value greater than two may indicate aggregation of the particles. The determination of the fractal dimension was used to interpret the scattering data and determine which datasets were suitable for further analysis.

Only one sample displayed scattering data with a fractal dimension near the expected value (D_f = 2), all other samples displayed a fractal dimension of 3.5 or greater. The sample which produced the expected behaviour was a low concentration $K_{0.2}.Bi_2Te_3$ /NMP solution. Figure 5.18 shows the scattering data collected for both the low and high concentration $K_{0.2}.Bi_2Te_3$ /NMP solutions. From these plots the difference in gradient in the low Q region, related to fractal dimension, may be clearly seen.

As shown in plot a) of figure 5.18, the scattering data collected from the low concentration $K_{0.2}.Bi_2Te_3$ /NMP solution was fitted to a model. The scatterers were modelled as cylindrical particles, with aspect ratio of discs, using SASview software. The model was informed by using the data collected from dimensional analysis of AFM data of a 1 week old $K_{0.2}.Bi_2Te_3$ /NMP solution. The details of the fitting parameters and scattering length densities (SLD) (which were calculated assuming solvent and particle material density of 1.03 g /cm^3 and 7.7 g /cm^3, respectively) are given in table 5.9. Although the model could be modified to include the influence of a dense solvation shell or even the inclusion of other nanoparticles (such as telluruim nanorods), reasonable agreement was found for the simple model, as shown by the χ^2/N_{pts} value for this data fit.

Although the interpretable scattering data is limited, these studies demonstrate the importance of concentration upon nanosheet dissolution, as well as suggesting the importance of understanding the chemical stability of these solutions. The agreement of these results with the AFM dimensional analysis of the drop cast nanosheets supports the use of TEM and AFM to describe the nanosheets present in solution. These results suggest that further investigation and sample optimisation would be fruitful and that SAXS would be a suitable technique for future *in situ* solution characterisation.

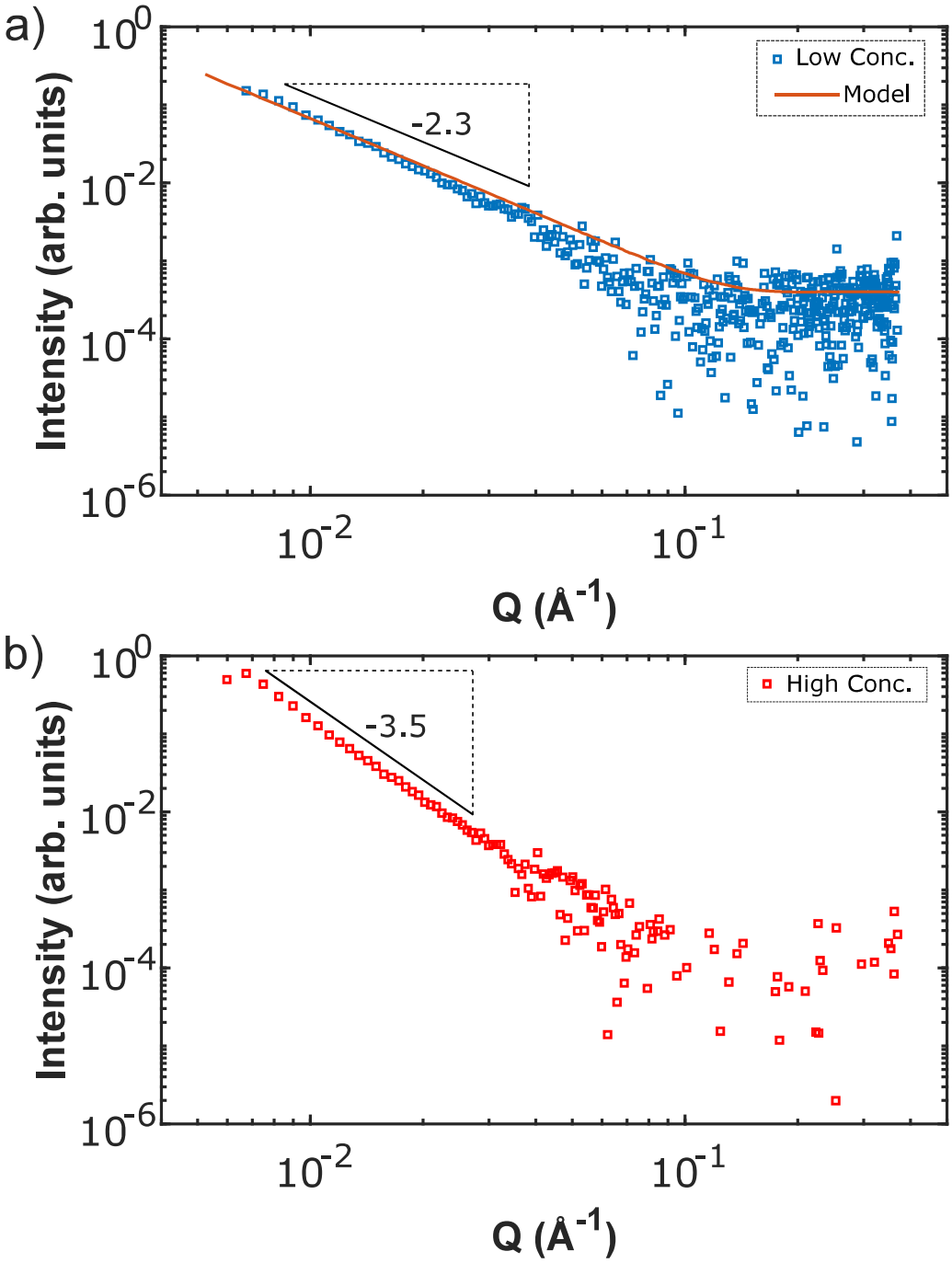

Figure 5.18: Small angle x-ray scattering data collected for $K_{0.2}.Bi_2Te_3$ in NMP. Plot a) shows (background subtracted) scattering data collected from low concentration solution sample with D_f = 2.3 and plot b) shows (background subtracted) scattering data collected for high concentration solution sample D_f = 3.5. The data in a) has been fitted using a model for disc-like scattering particles.

Fit Parameters				
Cylinder Diameter / Å	Cylinder Length / Å	Particle SLD (x 10^{-6} Å^{-2})	Solvent SLD (x 10^{-6} Å^{-2})	χ^2/N_{pts}
2290	30.5	51.3	9.5	0.00072622

Table 5.9: Modelling of SAXS data collected for the low concentration solution of $K_{0.2}.Bi_2Te_3$ in NMP. This table provides the fitting parameters used to fit the scattering data, as well as corresponding χ^2/υ values for this fit. The data and fit are presented in figure 5.18 plot a).

5.5 Conclusions

The primary focus of this chapter was to progress from the point of the successful demonstration of a nanomaterial production method, to build a more general description of the nanosheet solution and gain understanding of the factors which impact nanosheet production. This information is essential to transition to industrial scale production the of nanomaterial, but the knowledge gained may also be used to enable material manipulation and nanomaterial size selection.

The data presented in this work included the analysis of thousands of nanosheets, which greatly exceeds the sample sizes (typically tens of nanosheets) used in the particle analysis found within published literature relating to liquid phase exfoliation of layered materials [27][28]. In this work it was shown that the lateral width of deposited nanosheets was influenced by intercalant stiochiometry as well as solution age and was dependent on the liquid depth of aliquot removal, suggesting that each of these factors could be used to tune the nanomaterial properties and even be used to isolate large numbers of nanosheets with specific aspect ratios, without the need for non-scalable techniques such as centrifugation.

The data in this report allows for robust discussion of the nanomaterial properties and demonstrates the ability of this method to produce large number of nanosheets, as is necessary for mass production.

Preliminary SAXS data suggests agreement between the data collected from deposited nanosheets and the nanosheets present in their liquid environment. Visualisation of individual nanohseets *in situ* was attempted with the use of liquid TEM but improvement of the apparatus is required for the future success of this study. In both cases, it is important to note that, to the best of the author's knowledge, this is the first example of SAXS or liquid TEM study of solutions of this kind. Thus all the technical knowledge gained in attempting this complex technique presents an advancement of this field and will contribute to the successful

experimental execution in future.

Chapter 6

Results III: Chemical Stability of Nanosheet Solution and Origin of Tellurium Impurities

One of the distinctive qualities of the exfoliation method utilised in this work is that it requires the doping of the layered material and results in a nanomaterial which is charged. This manipulation of the material's electronic character necessitates careful consideration of the difference made to the material's chemical reactivity.

Much of the early work within the field of layered material intercalation concerns that of graphite, with the first alkali metal graphite intercalation compound (GIC) reported in 1926 [95]. Since then, structural properties have been explored [158] as well as a wide variety of possible graphite intercalation compounds [96], demonstrating that this carbon allotrope can intercalate both electron donors and acceptors. By expanding the scope of research concerning layered material intercalation compounds to that of less chemically stable materials (such as Bi_2Te_3 and Sb_2Te_3), it is required that the discussion must now also include that of chemical reactivity. In particular, limited chemical stability may render the technique impractical whilst the presence of impurities, resulting from highly reactive materials, may limit the applicability of the nanomaterial solutions.

Therefore, the motivation behind this chapter is to explore the implications

of doping a reactive layered material. It will explore the chemical stability of the nanosheet solutions and will determine the origin of tellurium based impurities as well as discussing possible ways to limit the presence of impurities in the nanosheet solutions.

6.1 Chemical Stability of the Nanosheet Solutions

There are many methods of liquid phase exfoliation, the specifics of each method and the choice of layered material will determine the limits of chemical stability of the nanoparticles in the liquid. The solutions produced by the exfoliation method utilised in this work are usually held within the inert atmosphere of an argon filled glovebox, with efforts made to reduce their exposure to conditions which may destabilise and degrade them.

Whilst it is evident that exposing the solution to air causes the solution to fundamentally change, the reaction of the solution with air is one of practical importance and it worth exploring further. In this section the boundaries of chemical stability of both the intercalated powder and the nanosheet solutions are explored in relation to three key factors: air, water and increased temperature.

6.1.1 Affect of Air Exposure on the Nanosheet Solutions

All stages within the production of the nanosheet material, from the intercalation of the layered material to the preparation of the solution, require strict air-free conditions. It is known that the layered materials, Bi_2Te_3 and Sb_2Te_3, are air-sensitive (reacting in air to form pnictogen oxides)[159][160], and so is the metal-ammonia solution used for their intercalation [126]. However, very little is understood about the impact of air exposure on intercalated material or their associated nanosheet solutions, despite its fundamental importance to the study and application of these nanomaterials.

When removing a nanosheet solution from the inert atmosphere of a glovebox and opening it to the atmosphere a distinct, visible change occurs. Over a period of hours, the dark coloured, opaque solution will change to a colourless, transparent solution with a dark, swollen sediment. It has been suggested that the nanosheets aggregate due to loss of charge upon oxidation when exposed

to air [6], as reported for solutions of charged carbon nanotubes [146][104]. The impact of air exposure on the nanosheet solutions was studied with a range of techniques, including TEM, UV-Vis absorption spectroscopy and dynamic light scattering (DLS) accompanied by zeta potential measurement.

6.1.1.1 Experimental Details

The nanosheet solutions were prepared by addition of 5 mL of dried NMP solvent to 0.0080 g of the chosen intercalated powder within a glass vial. The chosen powders were $Li_{0.8}.Sb_2Te_3$, $K_{0.8}.Sb_2Te_3$, $Li_{0.8}.Bi_2Te_3$, and $K_{0.8}.Bi_2Te_3$, therefore 4 solutions were produced in total for each technique. The solutions were left unperturbed in an argon filled glovebox for 10 days before any solutions were removed from the glovebox to complete the studies.

TEM samples were prepared from solutions which had been removed from glovebox and exposed to air for 1 week and preparation followed the typical drop-cast method (described in section 3.2.3). The prepared solutions were decanted into quartz cuvettes and UV-Vis absorption spectroscopy was conducted before opening the cuvette to air and recording the absorption spectra at regular time intervals thereafter. DLS and zeta potential measurements were conducted in a similar manner but the prepared solutions were instead decanted into appropriate glass cuvettes (with dip cell for zeta potential measurements).

6.1.1.2 Results of TEM Characterisation

It was found that all the solutions formed a dark sediment with clear, colourless supernatant within hours of being removed from the glovebox and exposed to air.

The visible difference between the dark-coloured solution held in the inert atmosphere of the glovebox and the colourless solution, the result of removing the solution from the glovebox and holding it in atmospheric conditions for 1 week, can be seen in figure 6.1 alongside the result of the TEM and SAED characterisation of the NMP solutions. The only consistent feature found during the TEM analysis of all the solutions were dense networks of amorphous particles, often rod-shaped, with tellurium signal detected during EDX analysis.

Whilst no hexagonal nanosheets were found in the other solutions following air exposure, the hexagonal-shaped particle as shown in image bii) in figure 6.1

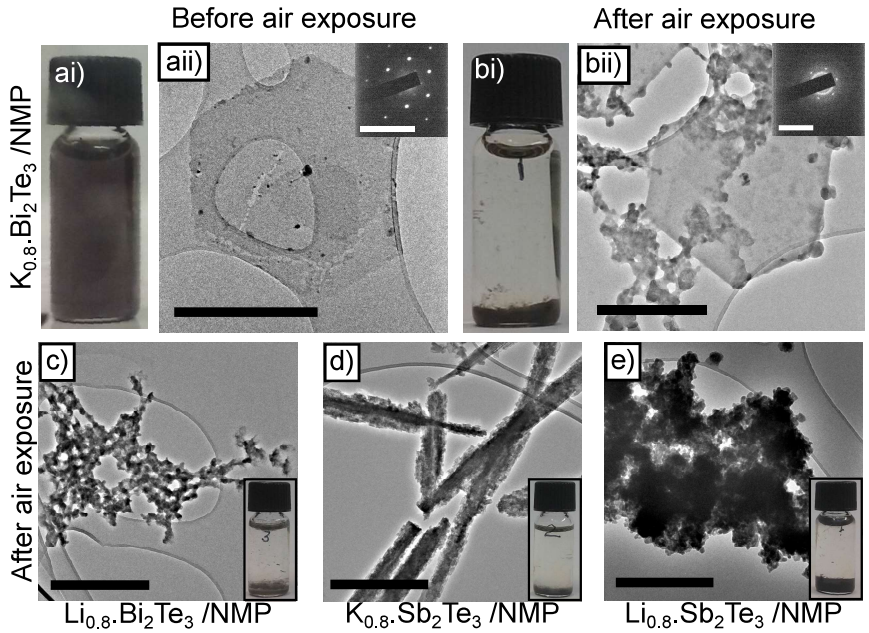

Figure 6.1: The influence of air exposure on the nanosheet solutions as studied by TEM. Images ai) and bi) are images of the $K_{0.8}.Bi_2Te_3$ / NMP solution before air exposure and after air exposure, respectively, with TEM images aii) and bii) of the nanoparticles deposited from solution before air exposure and after air exposure, respectively. A photograph of the air exposed solution and TEM image of deposited particles are given for c) $Li_{0.8}.Bi_2Te_3$ / NMP solution, d) $K_{0.8}.Sb_2Te_3$ / NMP solution , and e) $Li_{0.8}.Sb_2Te_3$ / NMP solution. The scale bars for TEM images are 500 nm and the scale bars for inset SAED are 10 1/nm.

was found for the air exposed $K_{0.8}.Bi_2Te_3$ / NMP solution. The hexagonal particle shown in the figure was one of many similar particles held within a dense network of amorphous particles, and it is believed to be an example of nanosheet aggregate formation. The EDX spectra of these possible aggregates displayed high levels of oxygen and low levels of tellurium, as well as weak diffraction patterns which were rapidly lost due to the extreme beam sensitivity of the particles. This difference in behaviour of these particles compared to the pristine nanomaterial found in glovebox stored solutions suggests that the air exposure and aggregation process is linked to oxidation of the nanosheets.

6.1.1.3 Results of Solution Characterisation

The affect of air exposure on the nanosheet solutions was studied using UV-Vis absorption spectroscopy and it was found that the absorption of the solution decreased with air exposure until the solution spectra matched that of the solvent

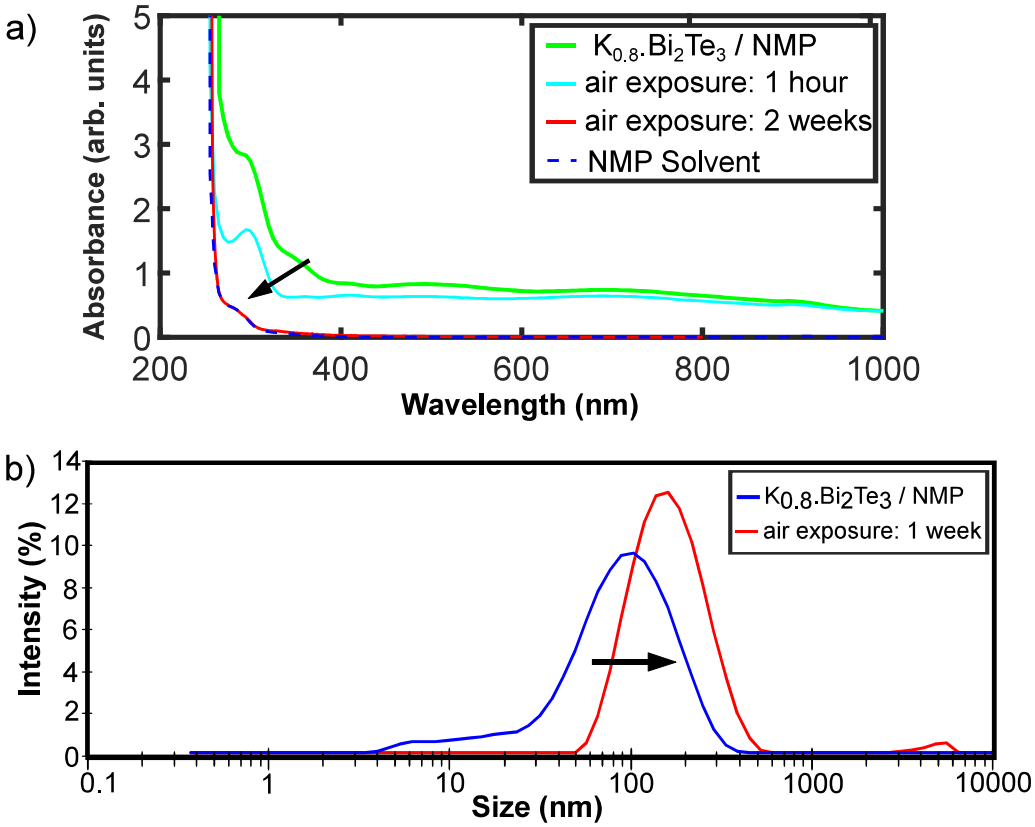

Figure 6.2: The influence of air exposure on the nanosheet solutions by using data collected from a $K_{0.8}.Bi_2Te_3$ / NMP solution as the example. Plot a) is a plot of the UV-Vis absorbance spectra collected for the solution, before and after air exposure, with comparison to the solvent spectra. Plot b) is the intensity particle size distribution collected using DLS, for the the solution, before and after air exposure.

spectra, as would be expected following sedimentation. The exemplar UV-Vis absorption spectra, shown in figure 6.2, shows the light absorption of the $K_{0.8}.Bi_2Te_3$ / NMP solution before air exposure, following 1 hour of air exposure, 2 weeks of air exposure, and compares this with the spectra of the pure NMP solvent.

The aggregation of particles within solution following exposure to air was investigated using DLS. The plot of particle size distribution given by the DLS measurement, as shown in figure 6.2, illustrates the aggregation of nanoparticles initiated by air exposure, forming large aggregates after 1 week of air-exposure. It may be seen that the general trend is the increase in size of the scatterers following air exposure of the solution, confirming aggregation.

The zeta potential was also measured for the solutions before and after air exposure. The zeta potentials for each of the solutions before air exposure, aver-

aged across three measurements, are given in table 6.1. However, no comparative data can be given for the air exposed solutions as the zeta potential could not be reliably determined from the phase shift of light scattered from these samples. The noise present in the phase analysis of scattered light may be due to the limited number of charged particles present or due to the nature of scattering from the large aggregates.

Whilst the zeta potentials measured for the NMP nanosheet solutions were all approximately -30 mV, which suggests that they are stable solutions as precipitation is expected to occur for zeta potentials smaller than ±10 mV [111]. It may be concluded that there are an appreciable number of charged particles present in solution before air exposure (giving a measurable zeta potential) and it is evident that exposing the solutions to air causes the solution to fundamentally change, so that the zeta potential measurement is no longer appropriate.

Solution	Average Zeta Potential, ζ mV
$K_{0.8}.Bi_2Te_3$ / NMP	-30.3
$Li_{0.8}.Bi_2Te_3$ / NMP	-29.0
$K_{0.8}.Sb_2Te_3$ / NMP	-30.1
$Li_{0.8}.Sb_2Te_3$ / NMP	-35.3

Table 6.1: Zeta potentials recorded for the prepared nanosheet solutions before air exposure. The average zeta potential values were calculated using three separate measurements.

In summary, the tests confirmed the loss of pristine nanomaterial, decrease in light absorption, and increase in average particle size, suggesting aggregation of the nanomaterial upon exposure of the solution to air.

6.1.2 Affect of Air Exposure on the Intercalated Material

A small portion of each of the intercalated powders ($Li_{0.8}.Sb_2Te_3$, $K_{0.8}.Sb_2Te_3$, $Li_{0.8}.Bi_2Te_3$, and $K_{0.8}.Bi_2Te_3$) was exposed to air and evaluated with respect to its ability to produce nanomaterial when added to the chosen solvents. The intercalated powders were held outside the glovebox for 10 minutes before being added to DMF and NMP, following the standard solution preparation method (addition of 5mL of dried solvent to 0.0080 g of the intercalated powder). The solutions were left for 10 days before TEM samples were prepared via the typical dropcast method (described in section 3.2.3). It was noted that the solutions remained clear and colourless with black powder at the base of the vial.

No hexagonal nanosheets were found during the characterisation of the TEM samples, nor was any bismuth or antimony detected using EDX. However, tellurium nanorods were found to be a consistent feature of each TEM sample. Even with air exposure amounting to only 10 minutes the effect is significant, demonstrating that air exposure of the intercalated powder limits the ability to produce the nanomaterial.

6.1.3 Use of Water as a Solvent

Whilst water exposure is avoided in this work, the addition of water to intercalated layered materials has been utilised by some to produce nanomaterial suspensions [44][161]. However, using water as a solvent for liquid phase exfoliation comes at the cost of nanomaterial quality and stability, with suspensions, stable for up to 1 week, containing damaged platelets of varying sizes, such that only small portion of the particles are thin enough to exhibit the desired properties.

The exfoliation and solvation of the layered material within this work depends upon the use of aprotic solvents and it is crucial that any solvent used must have its water content minimised. Whilst the solvents used are described as 'anhydrous', it was found that production of stable solutions with pristine nanosheets required the solvents to be further dried with the addition of zeolites to the solvent bottle. To avoid this problem, the water content of the solvents were monitored with the use of Karl Fischer titration and solvents were only used if the water content was $\leq$ 20 ppm, which was typically achieved within one week of solvent storage in the presence of zeolites (whilst held in the glovebox).

There was a noticeable difference in solution properties when employing a solvent with higher water content, the initially, dark, opaque solution would become transparent, purple/brown in colour, with swollen black sediment over the course of a week. TEM characterisation of material deposited from a 7 day old $K_{0.8}.Bi_2Te_3$ / NMP solution preprepared using NMP solvent (detected concentration of water: 60 ppm), can be seen in figure 6.3. The analysis showed that the solution which once displayed nanosheets had aggregated and the individualised nanosheets where no longer present, as a result of the higher water content of the solvent.

The reaction of intercalated material was further investigated to better understand the chemical stability of the material with respect to water and to contextual-

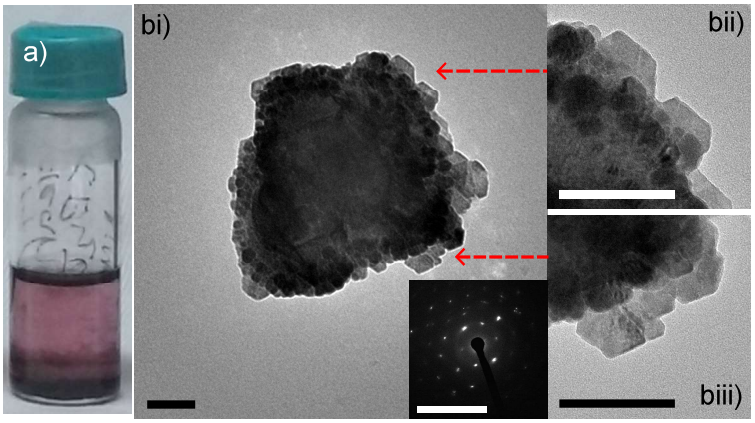

Figure 6.3: Features found in TEM study of solutions prepared using 'wet' solvents. Image a) is a photograph of the $K_{0.8}.Bi_2Te_3$ / NMP solution prepared with anhydorus solvent which had not been dried further with zeolites. TEM image bi) shows a typical feature found when characterising these solutions, the thick particle appears to comprise of smaller hexagonal platelets as seen in detail in the higher magnfication TEM images, bii) and biii). The scale bars for TEM images are 100 nm and the scale bars for inset SAED are 10 1/nm.

ise this work with respect other research using aqueous suspensions. The reaction of water with intercalated materials was studied by the addition of $Li_{0.8}Sb_2Te_3$ to deionised water and deionised water following a degassing process, the suspensions were then investigated using TEM. The distinction between deionised water and degassed, deionised water must be made as it is possible that the presence of dissolved gases within water may significantly influence the exfoliation and stabilisation of layered materials. This has been of interest in other works concerning aqueous nanosheet suspensions which claim improved colloidal stability by degassing water before using it as a solvent [162][163].

6.1.3.1 Experimental Details

Two suspensions were created by addition of 10 mL of either deionised water or deionised water which had been subjected to a degassing procedure, to 0.2500 g of $Li_{0.8}.Sb_2Te_3$ powder.

The deionised water was degassed by completing 5 freeze-thaw cycles (each cycle lasting for 30 minutes) with the use of a Schlenk line, with the water placed under vacuum when frozen to slowly remove the dissolved gases. In the case of the degassed water sample, the water was added to the intercalated powder (which was held under argon gas in a Schlenk tube) via metal cannula and sealed with a rubber septum for the lifetime of the solution, following typical handling of

an air-sensitive sample on a Schlenk line. In the case of the deionised water sample, the deionised water was added to the intercalated powder, which was held in an argon filled vial and sealed with a rubber septum, using a syringe.

TEM samples were prepared 7 days after the initial solvent addition and again after 7 weeks had elapsed. TEM preparation followed the typical dropcast method (described in section 3.2.3), but were dried outside the glovebox environment.

6.1.3.2 Experimental Results

Both of the aqueous $Li_{0.8}Sb_2Te_3$ suspensions prepared presented as a black, opaque liquid immediately following addition of water to the powder. Both of the solutions remained opaque black for one week, after which they became increasingly transparent and after a matter of weeks they were both clear colourless solutions with a black sediment present. The first TEM samples were taken after 1 week to avoid collection of larger thicker particles which are not suitable for TEM analysis and the second samples were collected after 7 weeks, at which point both suspensions were colourless and the sedimentation process was assumed complete. Whilst the deionised water suspension took 3 weeks to become colourless, the degassed, deionised water suspension took 7 weeks to sediment.

Figure 6.4 shows TEM images representative of particles deposited from the solutions seven days after initial water addition and seven weeks after initial water addition. From the TEM images it can be seen that the deionised water sample contained hexagonal nanaoparticles as well as tellurium nanorods. The hexagonal nanoparticles found in this sample were highly beam sensitive, so that no diffraction pattern could be recorded. This behaviour is significantly different from the hexagonal nanosheets typically collected from the NMP and DMF nanosheet solutions. The difference in the nanomaterial chemical character was confirmed by EDX which showed a strong oxygen signal, moderate antimony signal and weak tellurium signal, suggesting that the Sb_2Te_3 material had been oxidised.

There was no hexagonal material seen during the TEM characterisation of the deionised, degassed water suspension. Instead, clustered structures with confirmed chemical signatures of antimony and oxygen were found, as well as separate tellurium nanorods, suggesting chemical degradation of the bulk material with no preservation of the hexagonal nanosheet structure.

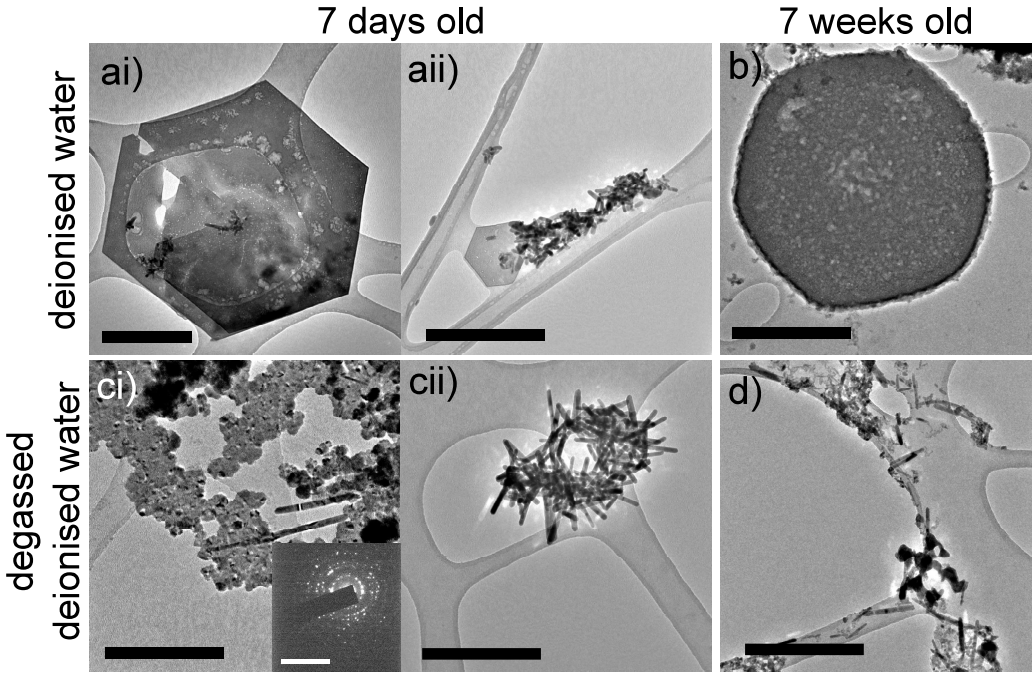

Figure 6.4: TEM study of solutions prepared using water as a solvent. The results of adding deionised water to $Li_{0.8}.Sb_2Te_3$, TEM images ai) and aii) show particles deposited from the suspension 7 days after its creation and TEM image b) shows a particle deposited from the suspension 7 weeks after its creation. The results of adding degassed, deionised water to $Li_{0.8}.Sb_2Te_3$ are shown in TEM images ci) and cii) which show particles deposited from the suspension 7 days after its creation and TEM image d) which shows a particle deposited from the suspension 7 weeks after its creation. The scale bars for TEM images are 500 nm and the scale bar for the SAED is 10 1/nm.

The suspensions were characterised again after 7 weeks had elapsed. At this point, the deionised water solution still contained large particles which EDX showed had a chemical signature of antimony and oxygen, although no longer distinctly hexagonal in shape they are assumed to be related to the hexagonal nanosheets found earlier in the sample. For the suspension made with deionised, degassed water the features found with TEM were very similar to the earlier study of the sample, no hexagonal nanosheets were found but a large number of tellurium nanorods were still present. Thus demonstrating the instability, towards oxidation and sedimentation, of the suspensions produced using both degassed water and water with dissolved gases still present.

6.1.4 Solvent Dependent Instability Towards Prolonged Heating

Heating of the nanosheet solution is an integral part of preparing dropcast samples for AFM and TEM investigation, and therefore the possibility of introducing artefacts through heating deserves careful consideration. Heating of the solutions is also of interest as it is possible that heating may provide insight into the thermodynamic balance of the dissolution mechanism, perhaps even allowing the yield of nanosheets to be increased.

6.1.4.1 Experimental Details

The solutions were prepared by addition of 5mL of dried solvent (either NMP or DMF) to 0.0080 g of $Li_{0.8}.Sb_2Te_3$ powder within a glass vial. The two solutions were left unperturbed in an argon filled glovebox for 7 days before the first TEM samples were prepared.

The two nanosheet solutions were characterised with TEM following the typical dropcast TEM preparation method (described in section 3.2.3). The solutions were then heated to 80°C for 1 hour, without stirring, from which a second TEM sample was prepared following the typical dropcast TEM preparation method. The two solutions were then removed from the hotplate, allowed to cool and a third TEM sample was prepared 1 week later. All preparation was conducted in the inert, argon atmosphere of a glovebox.

6.1.4.2 Experimental Results

It was found that the NMP solvent based solution displayed no perceivable difference immediately following heating or after the cooling period, considering visual inspection of the solution as well as TEM characterisation of the deposited material. The lateral width of the deposited nanosheets were measured for each TEM sample and there was no significant deviation found in the particle size distribution across the three NMP samples. These results are illustrated in figure 6.5.

However, the DMF based solution displayed significant nanosheet degradation following heating, with the effects being especially pronounced 1 week after heating. The nanoparticles deposited following heating, assumed to be derived

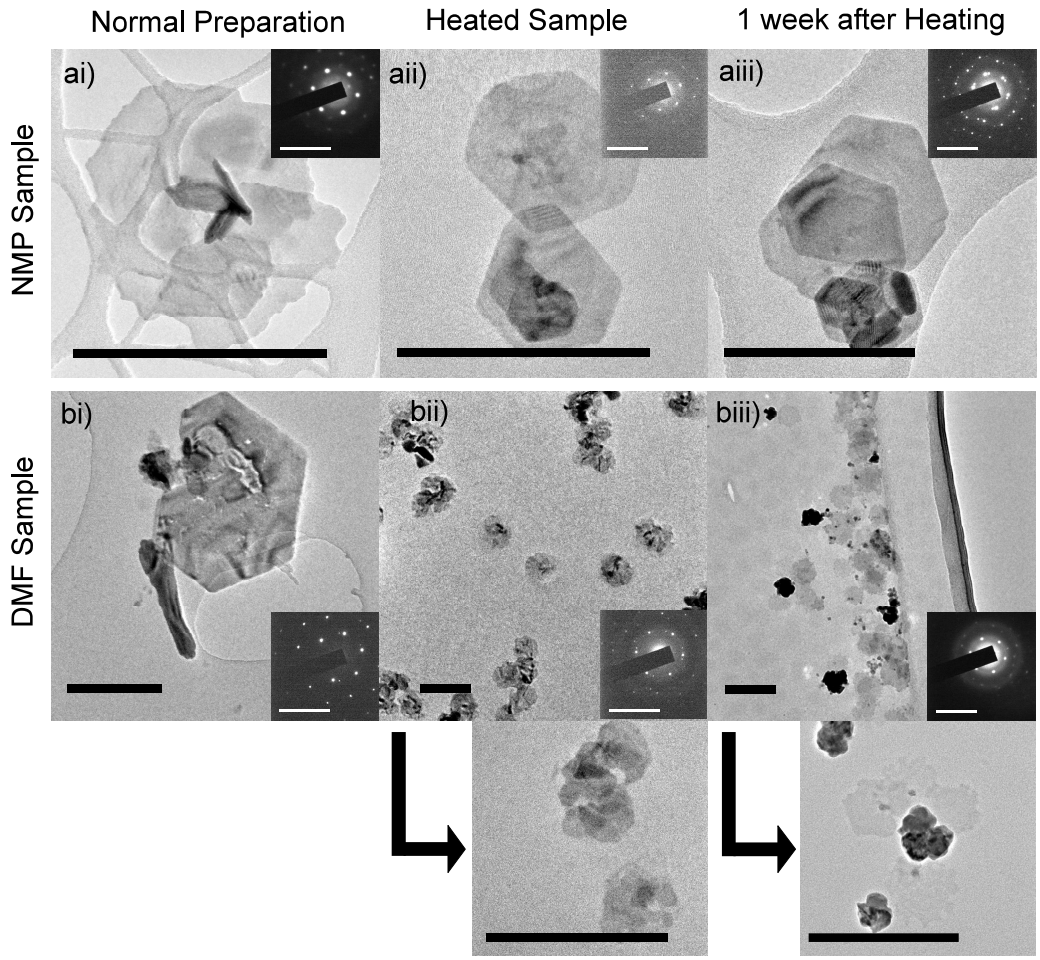

Figure 6.5: Heating a nanosheet solution for an extended period of time. The exemplar data given is derived from $Li_{0.8}.Sb_2Te_3$ in NMP and in DMF. TEM images ai-aiii) represent TEM samples which were created by dropcasting the NMP solution ai) before heating, aii) immediately after heating the solution for a prolonged period, and aiii) 1 week later. TEM images bi-biii) represent TEM samples which were created by dropcasting the DMF solution bi) before heating, bii) immediately after heating the solution for a prolonged period, and biii) 1 week later. TEM images bii) and biii) are connected to additional images showing further detail of the features found. All TEM images have associated SAED inset and all SAED are in agreement with the [001] for Sb_2Te_3. Scale bars in all TEM images equal 200 nm, scale bars in all SAED equal 10 1/nm.

from the original hexagonal nanosheets, were found to have irregular edges and multiple crystalline domains. The reduced contrast of the particles found in the sample prepared 1 week later suggests further degradation and possible thinning of the sheets. Whilst there were many tellurium nanorods present in the TEM sample of the heated DMF solution, there was a large increase in number of Te nanorods present in the TEM sample prepared from the solution 1 week after heating.

6.2 Characterisation and Synthesis of Tellurium Based Impurities

Although their production is not the primary motivation of this project, tellurium nanorods were found to be a frequent feature in the study of the nanosheet solutions. This highly anisotropic nanoparticle deserves further investigation, not only because the presence of impurities could undermine the practical application of nanosheet solutions, but also because their chemical character suggests that they may be related to the chemical instability of the desired nanomaterial. In particular, are these nanoparticles present in the bulk layered material, are they produced as a result of the intercalation process or are they formed within the liquid environment of the nanosheet solution? Since it is understood that these tellurium nanoparticles are an undeniable and common feature of the nanosheet solutions it is clear that their origins must be explored.

Figure 6.6 provides an introduction to the tellurium nanorods found within the nanosheet solutions. The figure displays the configuration of tellurium atoms found within the crystallographic unit cell, as well examples of Te nanorods as seen in TEM with their related diffraction pattern (SAED) and the XRD pattern of powdered tellurium.

SEM was used to investigate the dried powders to pinpoint at which stage of the chemical process tellurium nanorods become apparent. From the SEM results a hypothesis for impurity production was developed and tested through contaminant synthesis and characterisation using TEM and SAED.

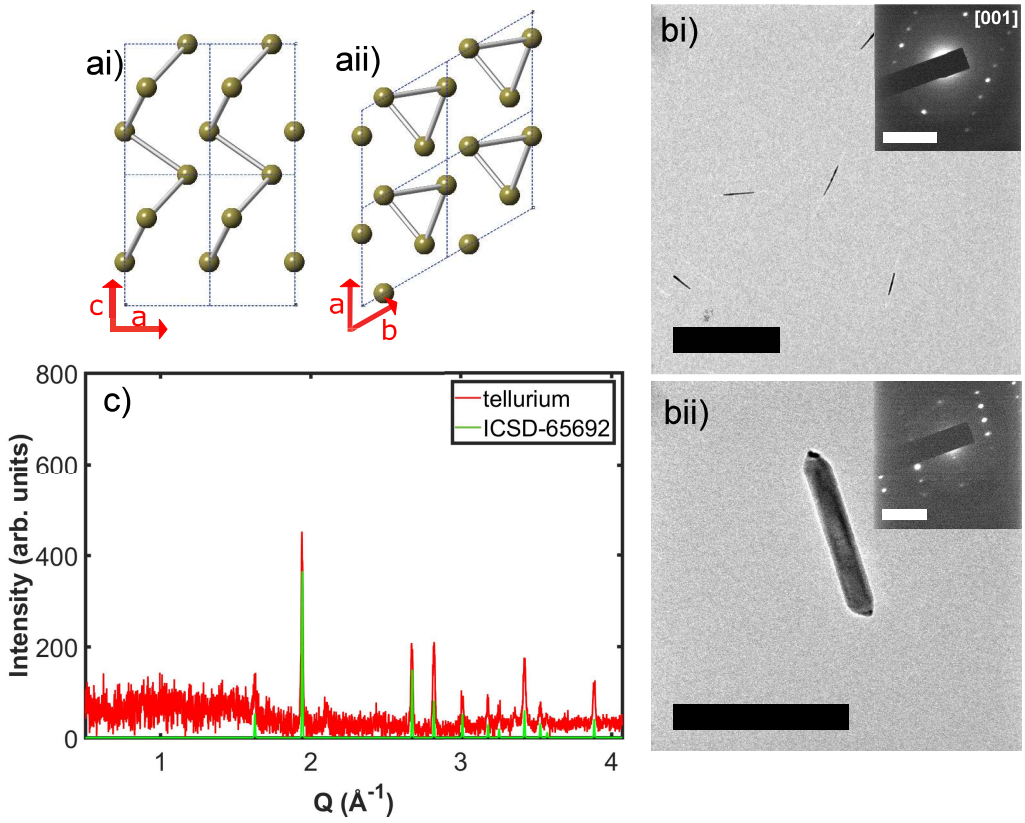

Figure 6.6: A summary of some physical properties of the tellurium nanorods found within the nanosheet solutions. The bonding and configuration of Te atoms within their crystallogrpahic unit cell is shown, as seen from the [100] direction in image ai) and the [001] direction in image aii). Images bi) and bii) are examples of Te nanorods as seen in TEM of dropcast nanosheet solutions, with their associated SAED. Scale bar in TEM image bi) is 500 nm and the scale bar in image bii) is 200 nm, the scale bars in the both SAED are 5 1/nm. Image c) shows a powder x-ray diffraction pattern collected for telluruim powder and is in agreement with solid Te (ICSD-65692) [164].

6.2.1 Determining the Origin of Te nanorods

Due to the distinct rod-like shape of the tellurium contaminants, SEM was used to study the dry powders, looking for evidence of the particle presence at each step in the material processing to determine the origin of such impurities. This approach has proved useful in identifying tellurium nanorods in $Bi_xSb_{2-x}Te_3$ powders [165].

6.2.1.1 Experimental Details

The powders investigated using SEM were the Sb_2Te_3 and Bi_2Te_3 powders (purchased from Sigma Aldrich), these same powders following outgassing, and the intercalated powders ($K_{0.8}.Bi_2Te_3$, $Li_{0.8}.Bi_2Te_3$, $K_{0.8}.Sb_2Te_3$, and $Li_{0.8}Sb_2Te_3$). Undissolved powder present in 3 week old NMP solutions of these intercalated powders (prepared following the typical method: 5mL of dried NMP solvent to 0.0080 g of the chosen intercalated powder within a glass vial) was also investigated. To isolate the undissolved powders, the liquid was removed using a pipette and the sediment was slowly heated to dryness at 80°C for 2 hours.

The SEM samples were prepared following the typical SEM sample preparation method, as described in section 3.2.4. All samples were prepared in the inert atmosphere of an argon glovebox. Effect of air exposure on the imaging of samples was investigated by exposing a duplicate $K_{0.8}.Bi_2Te_3$ SEM sample to air for 24 hours, although there was no perceivable difference between the size and shape of features present in these samples, image quality was limited in the air exposed sample due to charging effects during SEM imaging (indicative of insulating behaviour) and thus air exposure was minimised for all other samples during sample exchange.

6.2.1.2 Experimental Results

From the SEM investigation it was found that rod-shaped particles, as well as flake-like features, were present in the powdered sample following the intercalation step and were not present in the original starting powder. These rod-like particles are assumed to be tellurium based compounds, and it is interesting to note that their rod-like structure is present before the powder is introduced to the liquid environment. Similar flake-like and rod-like features were found in the solid

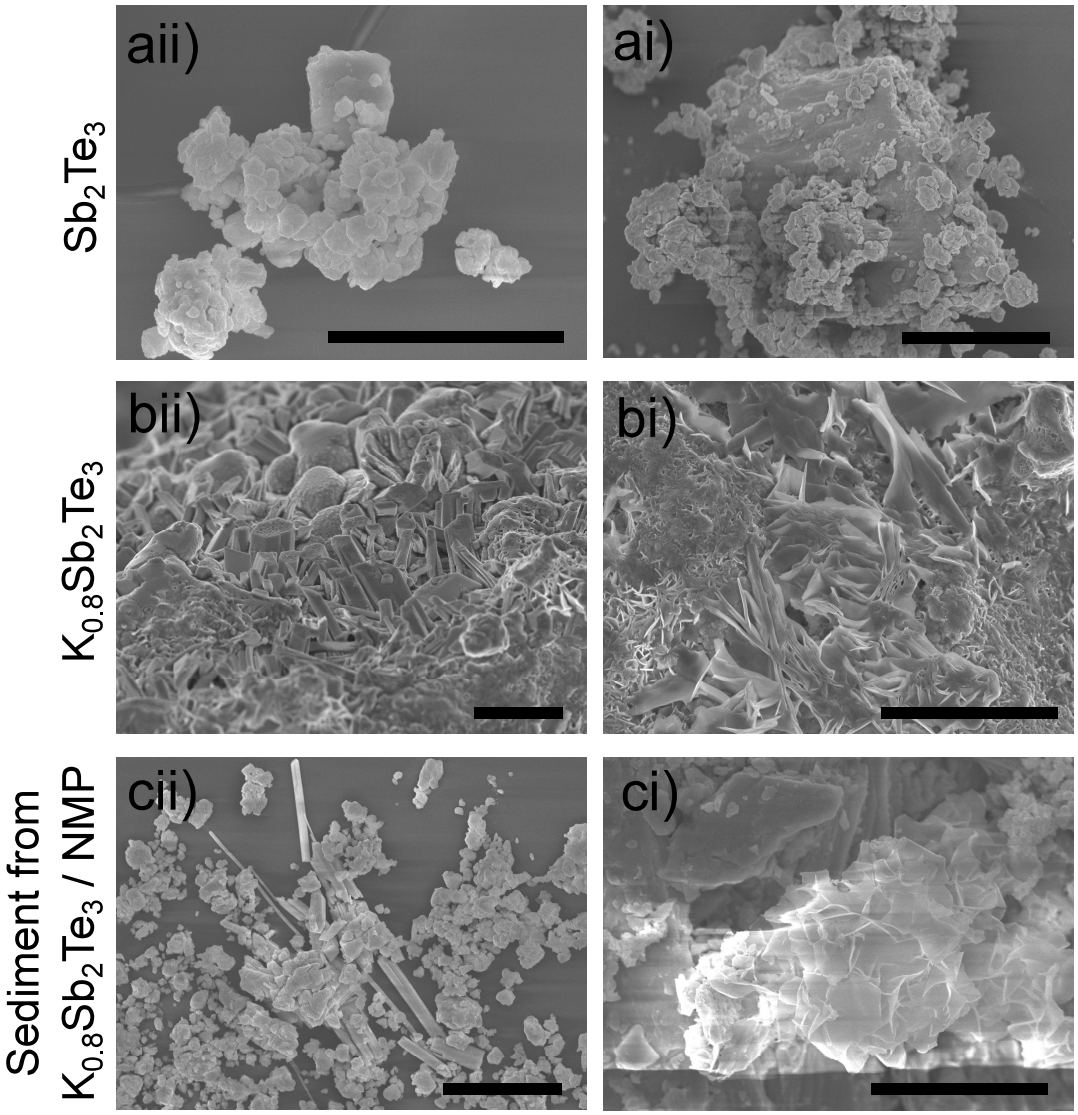

Figure 6.7: SEI-SEM images collected from various pnictogen chalcogenide powders. Images ai) and aii) show smaller and bigger particles present in the as received, Sb_2Te_3 powder. Images bi) and bii) show the flake-like and rod-like features found in the intercalated powder, $K_{0.8}.Sb_2Te_3$. Images ci) and cii) show the flake-like and rod-like features found in the dried sediment collected from the $K_{0.8}.Sb_2Te_3$ / NMP solution. All scale bars represent 5 µm.

material collected and dried from the NMP solutions for each intercalated powder. It is believed that the flake-like features are a result of swelling of the layered material as well as delamination.

These observations have been summarised in figure 6.7, where images collected of Sb_2Te_3 powder, $K_{0.8}.Sb_2Te_3$ powder and $K_{0.8}.Sb_2Te_3$ / NMP sediment have been used as the example. Representative SEM images collected for the Te powder, the potassium telluride (K_xTe_y) powder and the lithium telluride (Li_xTe_y) powder may be seen in figure 6.8 and act as reference for the rod-shaped features. The variety of larger and smaller sized particles, plate-like but otherwise irregular in shape, are expected features of a layered material powder which has been subjected to ball milling. No difference was found between the as received powders or outgassed powders and no appreciable difference was found between the particles of Sb_2Te_3 powder and Bi_2Te_3 powder.

6.2.2 Replicating the Production of Tellurium Impurities

It was identified from the SEM study that the rod-shaped impurities were appearing following the metal ammonia intercalation step and they were assumed to be related to the rod-shaped tellurium nanoparticles frequently found in dropcast TEM samples of the nanosheet solutions. The low solubility of elemental tellurium in both polar and non-polar solvents [166] suggests that it is unlikely that rod-shaped impurities are purely tellurium, instead it is likely that these particles comprise of a tellurium compound which is soluble in polar solvents, thus explaining their prevalence throughout the nanosheet solutions.

By surveying the related literature it was discovered that alkali metal polytellurides (A_xTe_y, A= alkali metal: Li, Na , K...) with a range of possible stoichiometries are produced when tellurium is in the presence of an alkali metal in ammonia solution [167][168][169]. Another A_xTe_y synthesis method, requires the heating of the alkali metal and tellurium (or more generally the chosen chalcogenide) in an aprotic polar solvent (NMP and DMF) at high temperatures (110°C) [170]. Although the presence of crystalline tellurium is not detectable in the x-ray diffraction patterns of the layered materials, it is possible that tellurium is available for reaction due to lattice defects present in these materials which are known to deviate from their given stoichiometry [171]. Whilst it is possible that the two synthesis routes may be involved in the introduction of soluble tellurium impurities in the nanosheet solutions, the prolonged heating and higher temperatures required

for synthesis of polytellurides in the aprotic solvent is not relevant to the standard conditions required for dropcast sample heating and drying, therefore only the metal ammonia synthesis route will be discussed further.

It was decided to further investigate the hypothesis that alkali metal polytellurides were related the formation of tellurium based impurities present in the nanosheet solutions and so the alkali metal polytellurides were synthesised using a metal-ammonia solution. The two synthesised powders will be referred to as potassium polytelluride (K_xTe_y) and lithium polytelluride (Li_xTe_y), encompassing the possible mixture of compounds with differing stoichiometry. The powders were investigated using SEM and XRD and solutions were made from the synthesised powders which were then characterised using TEM.

6.2.2.1 Experimental Details

Actions were taken to replicate the conditions of layered material intercalation during which it is proposed that this reaction may be present. Powdered tellurium was outgassed and then reacted with either lithium or potassium by following the same conditions applied to the outgassing and intercalation (via ammonia route) as described for the layered materials in section 3.1. However, it is not known what the ratio of elemental tellurium to alkali metal may be if this reaction is present during the intercalation of the layered materials. It was decided that any elemental tellurium present was likely to be present in small amounts and thus the alkali metal was in excess during the reaction (molar ratio of Te:alkali metal given as 2:3). The synthesised alkali metal polytelluride powders were characterised using PXRD.

The alkali metal polytelluride solutions were prepared by addition of 5 mL of dried NMP solvent to 0.0100 g of the chosen synthesised powder within a glass vial. The solutions were left undisturbed for 1 week and were then characterised using TEM following the typical dropcast TEM preparation method (described in section 3.2.3). All samples were prepared in the inert atmosphere of an argon glovebox.

6.2.2.2 Characterisation of Synthesised Alkali Metal Polytellurides

The powder diffraction patterns were collected for the synthesised lithium telluride (Li_xTe_y) and potassium telluride (K_xTe_y) powders, they are presented in figure

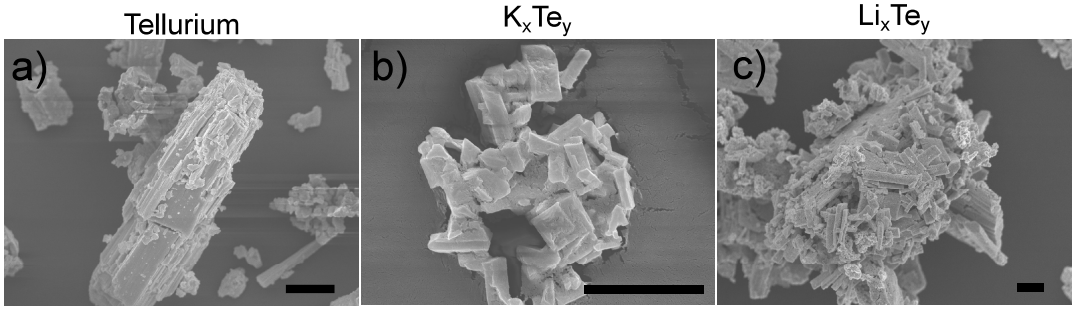

Figure 6.8: SEI-SEM images collected of the synthesised alkali metal polytellurides. Images a), b) and c) show the Te powder, the potassium polytelluride (K_xTe_y) powder and the lithium polytelluride (Li_xTe_y) powder, respectively. All scale bars represent 5 µm.

6.9. It can be seen that the synthesised lithium polytelluride is in agreement with the known structures: Li_2Te (ICSD-60434)[172] and $LiTe_3$ (ICSD-935) [173] . Whereas, K_2Te (ICSD-60441) [172] and K_2Te_2 (ICSD-73178) [174] were identified in the potassium polytelluride diffraction pattern.

Although the alkali polytellurides are not detectable in the x-ray diffraction pattern of the layered material when intercalated with lower alkali metal ratios, the XRD pattern collected for $K_5.Bi_2Te_3$ presents additional peaks characteristic of the potassium polytelluride K_2Te (ICSD-60441) and K_2Te_2 (ICSD-73178), as well as Bi_2Te_3 (ICSD-184631) as shown in figure 6.9. This result further supports the argument that alkali metal polytellurides are a contaminant present following intercalation.

SEM-SEI images were collected for the Te powder, the potassium telluride (K_xTe_y) powder and the lithium telluride (Li_xTe_y) powder and may be seen in figure 6.8.

6.2.2.3 Characterisation of Polytelluride Solutions

The TEM characterisation of the dropcast alkali metal polytelluride solutions showed many similarities to the contaminant features found during the TEM analysis of dropcast nanosheet solutions. The wide variety of features seen in TEM analysis of the polytelluride solutions are shown in figure 6.10, where the structures have been generally grouped as dendritic, rod-like and polygons. Unfortunately, not all of the crystalline diffraction patterns collected via SAED could be identified, with difficulty related to the polycrystallinity of material, high density of overlapping particles and rapid change of these patterns due to extreme beam sensitivity of

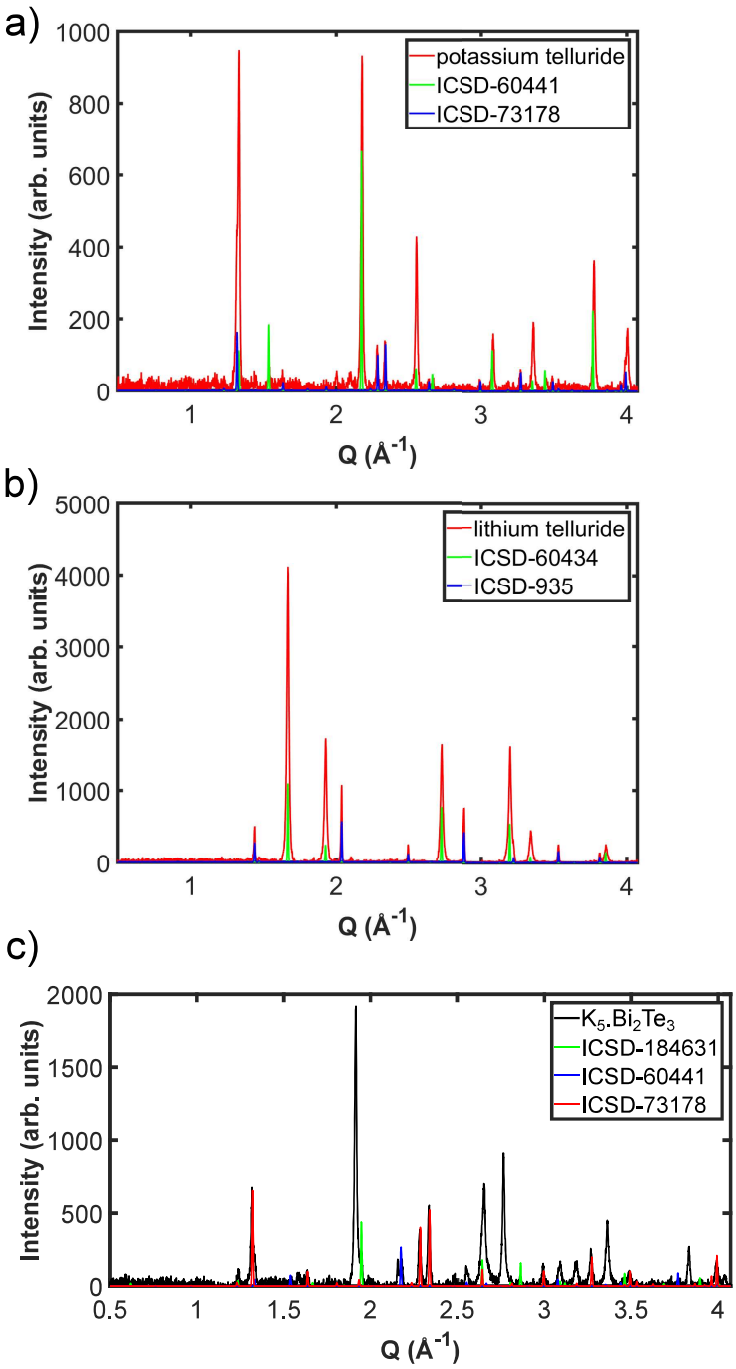

Figure 6.9: Powder x-ray diffraction patterns collected for the synthesised potassium polytelluride (K_xTe_y) powder (seen in a) and the lithium polytelluride (Li_xTe_y) powder (seen in b). The potassium polytelluride diffraction pattern has peaks which are in agreement with K_2Te (ICSD-60441)[172] and K_2Te_2 (ICSD-73178) [174]. The lihtium polytelluride diffraction pattern has peaks which are in agreement with Li_2Te (ICSD-60434) [172] and $LiTe_3$ (ICSD-935) [173]. Shown as an example of the presence of these polytellruides in the intercalated material, the XRD pattern collected for $K_5.Bi_2Te_3$, plot c), displays peaks characteristic of Bi_2Te_3 (ICSD-184631) as well as the potassium polytelluride K_2Te (ICSD-60441) and K_2Te_2 (ICSD-73178).

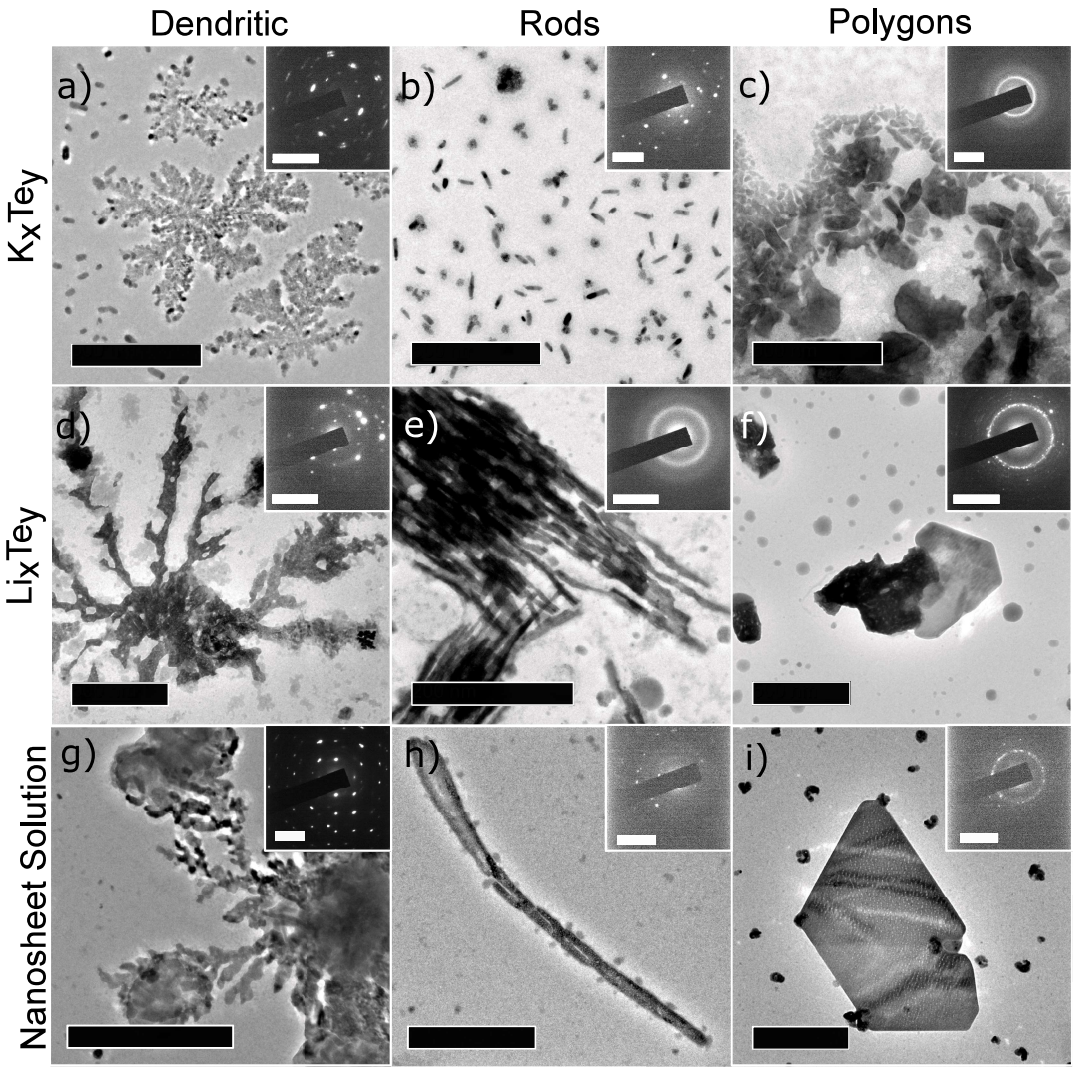

Figure 6.10: Features found in the TEM study of solutions created from potassium tellurides (K_xTe_y) and lithium telluride (Li_xTe_y) in NMP and DMF, comparing them to similar features found from dropcast nanosheet solutions. TEM images a), b) and c) show the dendritic, rod-like, and polygon structures found deposited from the K_xTe_y solutions. TEM images d), e) and f) show the dendritic, rod-like, and polygon structures found deposited from the Li_xTe_y solutions. TEM images g), h) and i) show examples of the similar dendritic, rod-like, and polygon structured contaminants found deposited from the nanosheet solutions (specifically $Li_{0.8}.Sb_2Te_3$ / NMP, $K_5.Bi_2Te_3$/ NMP and $K_4.Bi_2Te_3$/ NMP solutions, respectively). The crystalline diffraction patterns collected via SAED could not be identified. Scale bars for all TEM images represent 500 nm and scale bars for all SAED patterns represent 5 1/nm.

these materials. The features may be directly compared with those found in the TEM of the dropcast nanosheet solutions, where example of these polytellurides were found.

One difference which was observed during characterisation of the solutions was the abundance of nanorods within the deposited DMF solutions compared to the deposited NMP solutions. There appears to be a greater number of nanorod structures in the deposited DMF samples and these structures were found to be more stable in the beam as well as being crystalline. The difference in tellurium nanorod appearance and behaviour has also been noted in the solutions produced using the intercalated layered materials. The difference may be related to the differing solubility of the impurity material in the two solvents or may even be a result of DMF somehow promoting the production of tellurium nanorods in solution.

Whilst the connection between the alkali metal polytellurides and metallic, crystalline tellurium nanorods may not be obvious, it has been shown that alkali metal polytellurides oxidise rapidly to form polytellurides and then metallic tellurium, with the preference for growth along the z-axis, therefore creating tellurium nanorods [175][176][177]. It is likely that this oxidation occurs over time within solution and may explain the prevalence of tellurium nanorods within solution as well as the solution behaviour on exposure to air, moisture and prolonged heating. The results of this investigation support the hypothesis that tellurium contaminants present in nanosheet solutions are derived from alkali metal polytellurides which are formed during the metal ammonia intercalation of the layered materials.

6.3 Limiting the Presence of Impurities

In general, there are two approaches to limiting the presence of impurities: those which circumvent impurity production in the first instance and those which remove impurities at a later stage. Both of these approaches were considered in an attempt to minimise and remove tellurium based contaminants from the nanosheet solutions. The following section will describe these experiments, starting with impurity minimisation through manipulation of the metal intercalation process, followed by discussion of contaminant removal methods including liquid-liquid extraction techniques.

6.3.1 Efforts to Avoid Contaminant Production: Controlling Intercalation

Investigating the production of tellurium based impurities revealed that they were related to the metal intercalation process and that employing larger quantities of alkali metal increased the yield of these alkali metal polytellurides. Thus it was proposed that further manipulation of the intercalation process, through altering the intercalant character may avoid contaminant production completely.

It is known that, as well as the alkali metals, a number of alkaline earth metals (Ca, Sr, Ba) and Yb produce a solution of free electrons when dissolved in liquid ammonia [178]. Whilst the use of alkali metals in ammonia is known to produce alkali metal tellurides, examples of telluride production using alkaline earth metals or lanthanides in ammonia could not be found in the literature. To investigate whether intercalation using alternative metals may alter or avoid the production of tellurium based contaminants or perhaps alter their solubility, Bi_2Te_3 was intercalated using three alternative metals. Intercalation was completed using two alkaline earth metals, barium and calcium, and the lanthanide, ytterbium. Solutions were created and then characterised using TEM.

6.3.1.1 Experimental Details

The intercalated powders, $Ca_{0.8}.Bi_2Te_3$, $Ba_{0.8}Bi_2Te_3$ and $Yb_{0.8}.Bi_2Te_3$ were produced following the standard intercalation method (details given in section 3.1). The powders were all investigated using XRD. Solutions were created by addition of 5 mL of dried solvent (either THF, DMF or NMP) to 0.0080 g of the chosen intercalated powder within a glass vial. The solutions were left undisturbed for 7 days before any liquid was removed to produce TEM samples. TEM preparation followed the typical dropcast method (described in section 3.2.3).

6.3.1.2 Experimental Results

PXRD characterisation of the intercalated powders showed the preservation of crystalline Bi_2Te_3, with no additional peaks observed in any of the intercalated powders. Unlike the alkali metal intercalated powders, when the alternative metal powders were added to the solvents, all solutions remained clear and colourless with black powder present at the base of the vial, and did not exhibit any Tyndall

scattering when irradiated with a laser. Upon investigating the liquids using TEM analysis of the dropcasted solution, no hexagonal nanosheets were found for any of the samples and bismuth was not detected in the dropcast samples when using EDX.

However, in the case of the $Ca_{0.8}.Bi_2Te_3$ and $Yb_{0.8}.Bi_2Te_3$ samples, tellurium was detected using EDX and individual Te nanorods, as well as dense networks of tellurium, were found. Thus it was discovered that the use of alternative metals for intercalation neither minimised the yield of tellurium based contaminants nor did they achieve nanosheet production. These results are summarised in figure 6.11, where the presence of tellurium particles in the calcium and ytterbium samples can be seen alongside the SEI-SEM investigation of the ytterbium intercalated powder, which shows dense nanoparticle coverage but no evidence of appreciable swelling or exfoliation of the material's layered structure.

6.3.2 Contaminant Removal: Liquid-Liquid Extraction

The principle of liquid-liquid extraction is frequently applied post chemical synthesis to remove contaminants or to isolate desired products. The process exploits the difference in polarities of the various chemical products to segregate them, based on thermodynamics of solvation, between two liquid phases: a polar solvent and a non-polar solvent. For example, this concept may be applied to the removal of non-polar chemicals by washing of the original liquid (mother liquor) with a non-polar solvent.

It was proposed that the Te nanorods and tellurium based impurities often found in samples could be removed by employing this liquid-liquid extraction technique and exploiting the possible difference in polarity between the impurities and nanosheets. Interestingly, the difference in polarity of the two phases and the resulting liquid boundary has also been utilised in nanoparticle solutions to form a thin film of self-assembled nanoparticles [179][180]. It was decided that this technique would also be explored.

Solvent polarity is considered a sliding scale and so numerous solvent pairings may be used and carefully tailored to meet the specific post processing needs, with other physical properties such as the solvents' relative densities and their boiling points informing the decision on the most appropriate solvent pairing. The choice of solvent for the non-polar phase was informed by the needs of the impur-

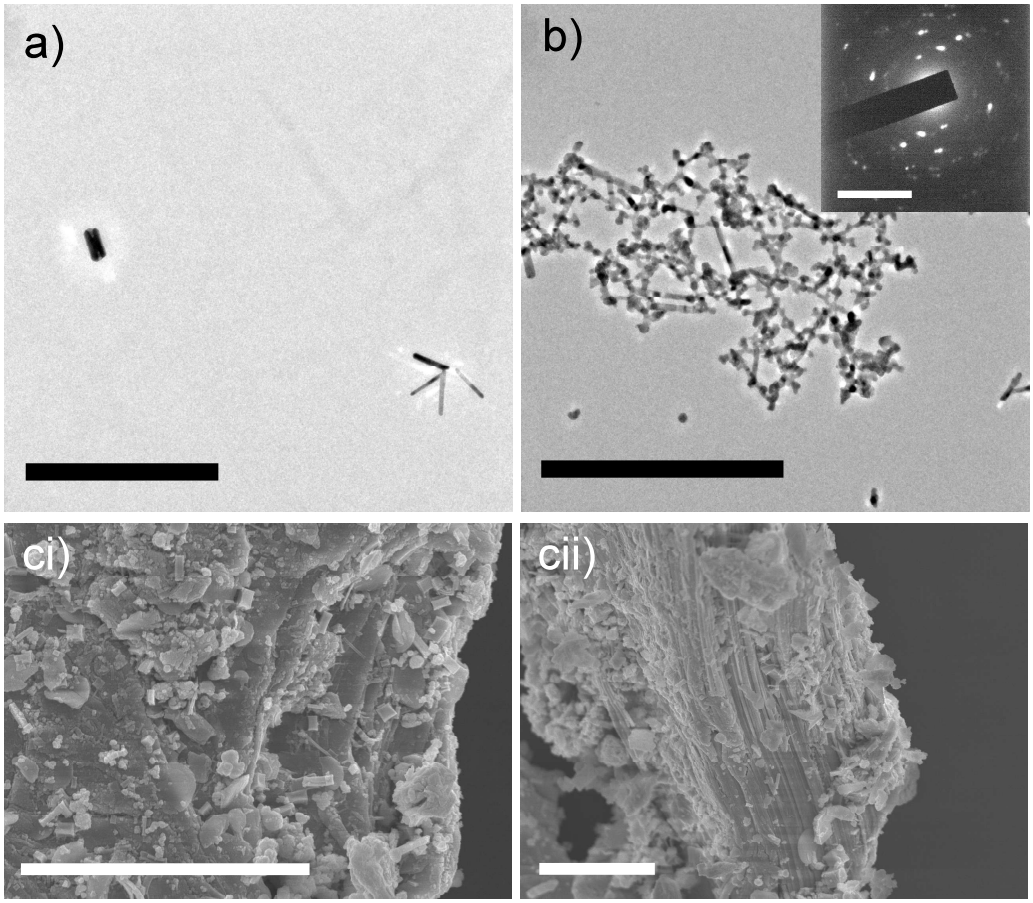

Figure 6.11: TEM study of the alternative metal intercalation experiments. TEM images a) and b) show the telluruim nanorod structures found within the deposits of the $Ca_{0.8}.Bi_2Te_3$/ NMP and $Yb_{0.8}Bi_2Te_3$/ NMP solutions, repectively. SEI-SEM images ci) and cii) were collected of the $Yb_{0.8}Bi_2Te_3$ powder. Scale bars for all TEM images represent 500 nm, the scale bar for the SAED represents 5 1/nm and the scale bars for the SEM images equal 5 µm.

ity extraction experiment as well as the nanoparticle film formation. However, this induces a high specificity in solvent properties, requiring low polarity, high density, high boiling point, (relative to the properties of DMF and NMP). As well as these factors, it was decided that the non-polar solvent should not contain any labile oxygen or hydroxide groups in case of reaction with the nanosheet solution, as well as excluding the use of highly toxic or carcinogenic solvents.

The three non-polar solvents chosen are listed in table 6.2 with their density, dielectric constant, melting points and boiling points. Dielectric constant has been given as an indication of solvent polarity, with the general distinction that non-polar solvents have a dielectric constant below 15. As shown in table 6.2, biphenyl and diphenyl ether both have a higher density than the two aprotic polar solvents (NMP and DMF), making it possible to carry out the experiments with the non-polar phase held at the bottom of the vial. However, both solvents have a high melting point with biphenyl (melting point of 69.2°C) requiring heating during its use. As an alternative to diphenyl ether and biphenyl, hexane is a low density and low melting point solvent, which would not be suitable for possible nanoparticle thin film formation but was included in the study as it avoids the difficulties associated with the higher melting point solvents whilst still providing the possibility of impurity extraction.

Solvent name	Density (g cm^{-3})	Dielectric Constant	Melting Point (°C)	Boiling Point (°C)
NMP (N-Methyl-2-pyrrolidone)	1.028	32.2	-24	202
DMF (Dimethyl-formamide)	0.944	36.7	-61	153
Diphenyl Ether	1.08	3.90	25	121
Biphenyl	1.04	20	69.2	255
Hexane	0.655	1.88	-96	68.7

Table 6.2: Solvents used for liquid-liquid extraction and their solvent properties [181][182].

6.3.2.1 Experimental Details

The solutions were prepared by addition of 5 mL of dried solvent (either NMP or DMF) to 0.0080 g of the chosen intercalated powder within a glass vial. The chosen powders were $Li_{0.8}.Sb_2Te_3$, $K_{0.8}.Sb_2Te_3$, $Li_{0.8}.Bi_2Te_3$, and $K_{0.8}.Bi_2Te_3$, therefore 8 solutions were produced in total. The solutions were left unperturbed in an

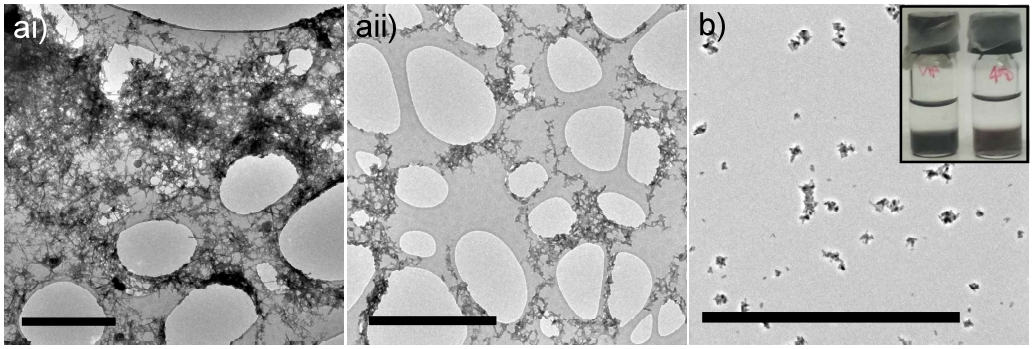

Figure 6.12: Liquid-liquid extraction experiments. TEM images ai) and aii) show the features found from sampling the polar layer of the diphenyl ether extraction experiment for the $Li_{0.8}.Sb_2Te_3$ in DMF and NMP, respectively. TEM image b) shows the similar results found from the polar layer sampling of the hexane extraction experiment, with the $K_{0.8}.Sb_2Te_3$ in NMP. The inset photograph shows two hexane extraction samples, with the clear/colourless, low density, non-polar hexane above the dark $K_{0.8}.Bi_2Te_3$ solution (NMP solution on the left and a DMF solution on the right). Scale bars for all TEM images represent 1 µm.

argon filled glovebox for 7 days before any liquid was removed from the vials.

2 mL of the each of the prepared nanosheet solutions was removed and added to 2 mL of the non-polar solvent (diphenyl ether, biphenyl or hexane) in a vial, therefore 24 liquid mixtures were produced in total. In the case of biphenyl, the solvent was heated to 70 °C to achieve the liquid phase whilst adding the polar liquid (nanosheet solution) and was held at this temperature during the study.

The vials containing the two liquid phases were shaken vigorously by hand for 5 seconds and then left for 4 hours. TEM dropcast samples were then created from the fractions of each liquid mixture.

The first TEM sample was prepared by removing an aliquot from the higher level fraction (low density phase), following the typical dropcast TEM preparation method (described in section 3.2.3). The low density fraction, was then completely removed using pipette, to allow free access of to the lower fraction (higher density phase). TEM samples were then prepared from the remaining lower fraction following the typical dropcast TEM preparation method (described in section 3.2.3).

6.3.2.2 Experimental Results

In the case of the high melting point solvent, biphenyl, the solutions became homogeneous and turned to a grey colour and it is thought that the prolonged heating of the two phases, required to avoid solidification of the biphenyl, caused the decomposition of the nanosheet solutions. For the extraction using diphenyl ether, the two liquid layers remained distinctly separate and the nanosheet solution became clear and colourless over a matter of hours, with black sediment collecting at the bottom of the vial rather than the liquid-liquid interface. As discovered from the TEM, neither of the high density, non-polar solvents were able to remove tellurium impurities. Nanoparticle thin film creation was not possible due to complication of homogenisation of the liquid (in the case of biphenyl) and sedimentation of the nanosheet material (in the case of diphenyl ether).

For the hexane based liquid-liquid extraction study it was found that no colour change occurred and there was no visible change suggesting exchange of material into the non-polar phase. It was also seen that the two phases separated rapidly when shaken.

Beyond this visual inspection, the particulate content of the phases were checked using TEM. None of the solvent pairings trials was able to achieve the removal of tellurium impurities, in fact it was found that the introduction of the non-polar solvents increased the amount of tellurium seen on the dropcast TEM samples and nanosheets were no longer detected in the samples. The TEM showed amorphous mesh with large numbers of Te nanorods, this is summarised in figure 6.12.

6.3.3 Considering Other Contaminant Removal Methods

There are a number of other contaminant removal methods which are typically employed within colloidal dispersions which may be used as inspiration for contaminant removal in the system employed in this work. Whilst the application of such methods are not feasible for this system it is worth briefly mentioning why they are inappropriate methods.

One method frequently used, which could be developed to manipulate the decomposition reactions and electrostatic stabilisation, are dialysis and ion exchange [183][184]. Typically these methods use membranes which have small

holes through which ions may pass, with their diffusion from original solution into solvent driven by a concentration gradient (sustained by their removal through replenishment of clean solvent). However, there is no known dialysis membrane with appropriate properties and solvent resistance which would allow it to be employed in the nanosheet solutions produced in this work. Simple filtration cannot be used either, this is due to the similar size of the nanosheets and tellurium based nanoparticles. Difference between the contaminants and the desired nanomaterial needs to be further studied, so that the knowledge may be exploited to allow for effective isolation of the desired product.

6.4 Conclusions

The results of the studies in this chapter reassert the importance of air free conditions both during the material production and handling of nanosheet solutions, to preserve the material properties and promote exfoliation. Exposure of the nanosheet solutions to air or water results in aggregation and sedimentation of the material as well as oxidation. Prolonged periods of heating have been shown to degrade the nanosheets present in DMF solvent. These points relate to the the production and preservation of pristine nanosheets and are therefore critically important to the possible industrial application of the materials and should be used as guidance for appropriate handling of such solutions in the future.

It was discovered that tellurium based impurities frequently found in the samples are related to alkali metal polytelluride production during the metal ammonia interclaltion process. These alkali polytellurides gradually oxidise to metallic tellurium and are observed as rod-shaped, tellurium nanoparticles in the deposits of the nanosheet solutions. Due to the lower electronegativity of tellurium (with respect to the other chalcogenides), tellurides may be considered more reactive and are more easily decomposed to elemental tellurium [185]. Thus the chemistry of tellurium significantly shapes the nanosheet solution stability and so dominates the studies reported in this chapter.

The reactivity of the tellurides also leads to the oxidation of Sb_2Te_3 in water [147]. During the investigation of water as a solvent for the exfoliation of the intercalated material ($Li_{0.8}.Sb_2Te_3$), a meta-stable suspension of amorphous, oxygenated nanosheets was produced. Whilst this demonstrates the necessity of using aprotic solvents for the exfolaition of these materials it also provides a pos-

sible route to material manipulation, with other examples of controlled oxidation of Sb_2Te_3 nanosheets being used to create porous structures useful for templating [186].

Impurity extraction is a particularly complex problem as the impurities display complex chemistry and gradual change in solution. With increased understanding of the contaminants present and their origin, a better understanding of the solution can be achieved, and with greater understanding comes the ability to optimise and manipulate the solution for greater gain. Liquid-liquid extraction was investigated as a possible tool for impurity removal, but the non-polar solvents chosen were unsuccessful in achieving contaminant removal. Although the impurity levels were not reduced by employing alternative metal intercalants, lowering the metal intercalant ratio can provide a simple control over impurities.

These studies have shown that the presence of impurities and chemical instability, although often ignored in the field of liquid phase exfoliation, must be addressed for these solutions to be introduced to industrial scale fabrication.

Chapter 7

Conclusion

The objective of this work was to produce stable solutions of pristine 2d nanomaterials from the thermoelectric materials Bi_2Te_3 and Sb_2Te_3, by using a scalable technique. This work demonstrates an ability to produce the desired nanosheets and has succeeded in addressing the pertinent questions surrounding application of this liquid phase exfoliation technique to these materials. The results of this work will now be summarised. This will then follow into a discussion of the findings in an overview of the thesis. Finally, interesting points of further exploration which have been discovered as a result of this work will be discussed in the future work section.

7.1 Summary of Results

A brief summary of the results of this work will be given and will follow the chronology of the results chapters presented in this thesis.

7.1.1 Summary of Results I

The first results chapter has shown that the chosen technique is capable of nanosheet generation using quintuple layer pnictogen chalcogenide compounds. The bulk layered materials were intercalated using alkali metals via a metal-ammonia solution, and then the intercalated powders were successfully dissolved in aprotic solvents (NMP and DMF) to produce dark-coloured, air-sensitive, solutions of 2d

nanosheets.

X-ray diffraction patterns collected for the intercalated material were found to be consistent with existing diffraction data on the intercalation compounds and also shows the material is crystallographically intact. Characterisation of the deposited nanosheets by use of TEM and AFM confirmed that the nanomaterial was crystalline and had nanoscale thickness as well as the expected chemical identity. The spontaneous dissolution and diffusion of nanosheet throughout solution was monitored over a period of days and the stability of solutions was demonstrated by the presence of pristine nanosheets in a 16 month old solution. It was shown that solvent choice and alkali metal-to-material intercalation ratio has a significant impact on the nanosheet production, with an optimum intercalation ratio of $0.1 < x > 1.5$ for $K_x.Bi_2Te_3$ for production of pristine nanomaterial with limited impurity level.

7.1.2 Summary of Results II

A more robust, extensive, and insightful description of the nanomaterial present in solution was built from the results of this second chapter, which included both *ex situ* and *in situ* techniques to investigate the range of nanosheets present in solution.

The preliminary investigation into the size distribution of nanosheets was completed with TEM as the technique allows the nanosheet crystallinity and chemical character to be confirmed. The TEM analysis of nanosheet dimensions revealed the polydispersity of the sheets present in the liquid samples and the distribution of material of different lateral width throughout the solution volume. Following this, AFM studies were conducted, where the lateral width and thickness of thousands of nanosheets were measured. This data was analysed to determine the distribution of nanosheets present, with respect to certain influencing factors such as liquid depth, age of solution and intercalant stoichiometry. This data provided insight into time dependence of the distribution of nanosheets throughout solution as well as intercalant stoichiometry as a route to controlling lateral width of dissolved nanosheets. The distribution of sheet sizes through solution presents an interesting question of dissolution kinetics and demonstrates the suitability of this method for scalable production.

To complement the TEM and AFM measurements, *in situ* measurement of the

nanomaterial dimensions were explored and scattering data presented. Agreement was found between SAXS data and the dimensional analysis of the low metal ratio material, thus supporting the use of AFM and TEM to describe the nanomaterial present in solution. Whilst SAXS has proved to be a promising technique for nanosheet solution characterisation, experimental adjustments must be made before liquid TEM may be successfully used to analyse these solutions whilst preserving their chemical stability.

7.1.3 Summary of Results III

The final results chapter was dedicated to the exploration of nanosheet solution chemical stability. Characteristic of their reactivity, tellurium nanoparticles were a common contaminant of the solutions and so they were investigated and their origin determined, with efforts made to eliminate their presence in solution. In particular, the reactivity of nanosheet solutions were tested in relation to certain conditions (air exposure, water, and prolonged heating at high temperatures) that were of importance to understanding their compatibility with ambient conditions and common processing techniques.

An investigation was made into the hypothesis that the presence of the common contaminant, tellurium nanorods, was a result of an reaction during the metal-ammonia intercalation process. SEM and TEM characterisation of powders and deposited material indicates that tellurium impurities present in nanosheet solutions are a result of the production of alkali metal polytellurides during intercalation. Armed with this knowledge, different approaches were conceived to eliminate the tellurium production and also remove the tellurium at a later stage in the solution lifetime. Alternative guest metals were investigated and liquid-liquid extraction applied but it was concluded that fine tuning metal stoichiometry provided the best control over tellurium impurities.

7.2 Thesis Overview

Perhaps the biggest barrier to the widespread incorporation of nanomaterials into everyday technology is the ability to repeatably produce and then manipulate these materials in ways that can be industrially scaled. Liquid phase exfoliation (LPE) of layered materials can potentially achieve this, though there are significant

problems associated with many LPE methods. These problems include damage caused to the material from use of sonication and use of non-scalable techniques for their manipulation (such as centrifugation). An alternative, emerging technique relies upon the charging of material to allow spontaneous dissolution of pristine 2d nanomaterials. This thesis encompasses the study of nanosheets produced via this spontaneous liquid phase exfoliation method, focusing on unanswered questions relating to the practicality of the method.

This thesis focuses on the exfoliation of thermoelectric pnictogen chalcogenide layered materials, Sb_2Te_3 and Bi_2Te_3, via the method of alkali metal intercalation and subsequent delamination of the negatively charged host structure and cationic guest species in anhydrous aprotic solvents (NMP and DMF). The work demonstrates the ability to produce large quantities of undamaged nanomaterials stabilised within liquid whilst also providing a route to size selection without reliance upon non-scalable techniques such as centrifugation. This liquid based manipulation of two dimensional nanomaterials is of particular interest for development of thermoelectic devices, as well as efficient, scalable nanomaterial transfer techniques, such as inkjet printing or spray coating.

Nanosheets deposited from solution were characterised using transmission electron microscopy (TEM) and atomic force microscopy (AFM), in combination with *in situ* small angle x-ray scattering (SAXS) and liquid TEM studies. A robust and representative description of the 2d nanomaterial, as confirmed by agreement with SAXS data, was derived from the analysis of thousands of nanosheets. It was found that gradual diffusion of nanosheets as a result of their spontaneous, unperturbed, exfoliation (unique to this method) lead to fractionation of nanosheets of differing lateral width throughout the liquid volume without need for centrifugation.

It was discovered, through adjusting the intercalant stoichiometry of Bi_2Te_3, that there is an optimum ratio ($0.1 < x < 1.5$ for $K_x.Bi_2Te_3$) for production of undamaged hexagonal nanosheets and that nanosheet lateral dimension could also be influenced by stoichiometry of the intercalant metal. Through the characterisation of these materials it was found that intercalant stoichiometry played a significant role in determining the prevalence of tellurium nanoparticles in the solutions. It was concluded that alkali polytellurides were produced during the intercalation of the layered material in the metal-ammonia solution, with their yield increased when higher metal concentrations were employed. It is believed that oxidation of these polytellurides result in the tellurium nanorods which are observed alongside

the nanosheets in the analysis of dropcast solutions.

In bridging the gap between the extensively studied graphite intercalation compounds (GICs), to the relatively under studied intercalation compounds of the pnictogen chalcogenide layered materials it has become apparent how important the recognition of their differences are. The chemistry and reactivity of the quintuple pnictogen chalcogenide layered materials are distinctly different from the GICs and this necessitates the consideration of impurity production (tellurium nanorods in this case), as well as careful handling of materials. It is possible that the intercalation compounds of the pnictogen chalcogenide layered material present a continuous intercalation phase, unlike the staging present in GICs, which may play a critical role in the stoichiometric dependency of nanosheet lateral widths. It is clear that this work has a wider relevance to other layered inorganic materials and how they are considered with respect to their reactivity and chemistry.

Although impurities are present, their prevalence can indicate a deviation from optimal conditions, therefore the knowledge of tellurium impurities can be used to inform suitable solution handling conditions. When adhering to prescribed solution handling conditions (specifically: minimising air exposure, water content of solvents and heating of the solutions) then the solutions are capable of demonstrating long term stability, with one example including nanosheets present within a 16 month old solution.

Together these results shed light on the delicate balance of factors which contribute to the spontaneous dissolution of these nanomaterials. In particular, the layered material must be intercalated to exfoliate in this way but also the identity of the intercalant (e.g. Alkali metal versus alkaline earth metal) and stoichiometry of the intercalant (concentration should not be too low or too high) play a significant role in achieving exfoliation. The choice of solvent is crucial, as demonstrated by inability to produce nanosheets when using a solvent with lower dielectric constant (THF), and also shown by the aggregation and oxidation that occurs when attempting to use water as a solvent. These points add weight to the argument that these liquids are true thermodynamic solutions and present an interesting subject for advancing the discussion of colloidal theory with respect to low dimensional materials in liquid.

The thesis addresses key issues of nanomaterial characterisation and chemical stability and it demonstrates the suitability of the chosen technique to produce 2d nanomaterials from Bi_2Te_3 and Sb_2Te_3 layered materials in a scalable manner. The intention of this work was to achieve stable solutions of pristine 2d nanoma-

terials by using a scalable technique, so that the properties of materials produced and the methods employed surpass that of others reported in the literature. This aim has been met and it has even exposed new avenues for exploration.

7.3 Future Work

Whilst many questions have been addressed in this work, as a result of the fruitful investigation new questions have arisen and new avenues of exploration have been exposed.

It has become evident in this work that the intercalation chemistry of the pnictogen chalcogenide layered materials deserve more attention and exploration. In particular, it would be useful to find a method of monitoring intercalation of these materials. Unlike other intercalated materials such as GICs, intercalation of the pnictogen chalcogenide layered materials does not cause appreciable swelling of the crystal structure and so intercalation cannot be monitored using PXRD. It is possible that electrochemical techniques may provide some insight and may even allow elucidation of the nature of the intercalation phase (continuous phase intercalation or stoichiometric intercalation phases). ICP-MS could also be used to examine exact metal content of each intercalated material and may help further understanding of the intercalation stoichiometry.

It would be interesting to further optimise the production of solution samples for SAXS analysis to strengthen the *in situ* characterisation of these nanosheet solutions, in particular exploring the compatibility of conventional colloidal theories with these anisotropic nanoparticles. With advancement of experimental design or even use of SANS (with possibility of isotopic substitution of the solvent), scattering techniques could be applied to investigation of the solvent structure immediately surrounding the nanosheets or even used to indirectly observe the delamination, dissolution and diffusion processes present in solution in real time.

It has been noted that conducting AFM measurements in ambient conditions lead to the likely over estimation of nanosheet thickness and so it would be of interest to conduct further AFM measurements in an argon atmosphere to measure nanosheet height as well as surface roughness without effects of air exposure.

The results have also highlighted that stirring might be used in future to rapidly homogenise the solution and perhaps aid exfoliation of the nanosheets in

a way which still scalable and gentle enough to avoid nanosheet destruction (in contrast to sonication). Achieving exfoliation through stirring may also provide insight into the energetic balance which determines the favourability of exfoliation. Calorimetry experiments may be a useful for observing the energy transfer during exfoliation, although care should be taken as the reaction of telluride species may obscure results of the such experiments.

Demonstration of colligative properties would also be useful in defining these solutions. Future experiments could include investigation of their behaviour with temperature variation, determining whether they exhibit boiling point elevation and freezing point depression (relative to the phase behaviour of the pure solvent). Such experiments require strict control over experimental conditions as their results are greatly affected by the presence of contaminants, and in the case of the materials used here such experiments would have to be conducted within an inert atmosphere. It is also worth considering how the presence of tellurides within the solutions may affect these results. Such studies are of great importance; they deserve careful consideration and rigorous experimental design.

Determining the thermoelectric figure of merit of the deposited nanosheets is also of great importance to evaluating this method with regards to its ability to produce thermoelectric nanomaterials. Future work could include the measurement of the material properties of these nanosheets. Control of the starting layered material with regards to the layered material stoichiometry (with the intention of minimising lattice defects, interstitials and vacancies) is likely to impact thermoelectric properties but may also lower the production of alkali metal polytellurides. Therefore control of the starting material properties may reduce prevalence of tellurium impurities in the nanosheet solutions and should be explored further.

The charged nature of the nanosheets is yet to be fully exploited. Future studies could include electrophoresis and chronoamperometry to analyse nanosheet diffusion and to probe the charged character of the nanosheets. Such methods may also be used to explore nanosheet deposition and decharging for possible application in thin film creation. The production of a nanomaterial thin film is likely to be of practical use for determining the material's thermoelectric properties.

The results of this thesis have highlighted the areas of interest with regards to these nanosheet solutions and in turn this will inspire and shape the future research within this field. There are two main avenues of exploration, these concern the in-depth investigation of the nature of these liquids and also the optimisation of these solutions with respect to improved handling and manipulation so that they

might achieve commercialisation.

Chapter 8

Appendix

8.1 Metal Ammonia Solutions

Ammonia's desirable properties are due to the large dipole moment which is a result of the free electron pairs present in the molecule and leads to hydrogen bonding networks within the solvent. These properties enable the solvation of certain metallic atoms within ammonia, forming so called metal-ammonia solutions ($M\text{-}NH_3$). Metal-ammonia solutions may be formed with alkali metals, (Li,Na, K, Cs), a number of alkaline earth metals (Ca, Sr, Ba) as well as the lanthanide Yb [178].

The solvation of metals within ammonia, to give separated metal cations and electrons, presents an interesting physical system of study as well as a useful source of electrons for employment in further chemical reactions [187]. The formation of $M\text{-}NH_3$ solutions can be represented as shown in equation 8.1, which demonstrates that the anion and electron are separate species and that the ammonia does not undergo a chemical change.

$$M + NH_3 = M^+ + e^- + NH_3 \tag{8.1}$$

Much of the interest in $M\text{-}NH_3$ solutions stems from their rich phase behaviour present over a wide range of metal concentrations as well as temperatures. When describing metal ammonia solutions, the concentration of metal is often given in mole percent metal (m.p.m.) which is related to the mole fraction of metal as

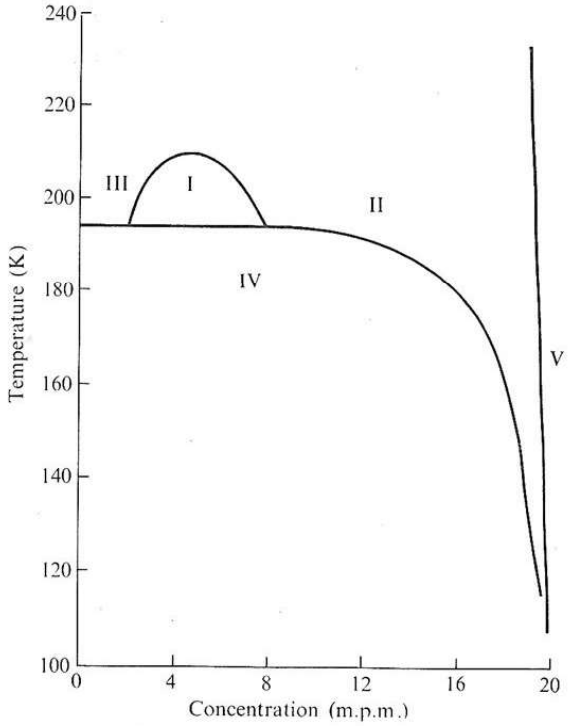

Figure 8.1: Phase diagram of lithium in ammonia. Figure reproduced from [126].

shown in equation 8.2.

$$(\text{m.p.m.}) = 100 * \frac{\text{molesofmetal}}{\text{molesofmetal} + \text{molesofsolvent}} \tag{8.2}$$

By careful control of the metal concentration of the metal ammonia solution, very different properties may be encountered, including those analogous to electrolyte solutions and even metallic liquids. This can be exemplified by the phase diagram of lithium-ammonia given in figure 8.1. The two regions of interest are region II and region III, which represent the respective phase area over which the non-metallic liquid and metal liquid are stable. Between these two regions is region I, leaving region IV and region V which represent excess solid ammonia and excess metal or metal amine, respectively. Whilst the extent of the area of stability for each of the described regions differ for each metal-ammonia solution, the phase diagrams are broadly similar. The greatest difference in phase diagram can be seen between the alkali metals and the alkaline earth metals due to their difference in valency, in particular the alkali metals prefer to donate a single electron into solution whilst the alkaline earth metals donate two electrons in the solution.

The presence of the metallic and non-metallic regions are attributed to the different behaviour of the solvated electrons associated with the increase in their concentration and resulting change in ion arrangement and solvent organisation. The physical properties of the two phases differ in many ways, the most immediately obvious is their difference in physical appearance with the non-metallic liquid being dark blue in colour and the metallic liquid being bronze colour. This visible differentiation is true of the M-NH_3 solutions irrespective of the identity of the metal solute. The origin of the solution colour is due to the behaviour of the electron in solution, in the dilute regime the electron is associated with the ammonia molecules whereas in the concentrated regime the electron may be treated as a free electron [188][189]. The dark blue colour of the low concentration M-NH_3 solution is due to the presence of an electron in a solvent cavity of approximately 3 Å, bounded by 4-8 ammonia molecules [190].

Although there are many similarities between metal ammonia solutions with differing metal solutes, there are some slight differences that effect their application. It has been shown that the ammonia surrounding smaller ions such as lithium are bound more tightly compared to the case of other alkali metal cations [126]. By using hard-sphere approximations it can be shown that the number of coordinated ammonia molecules surrounding Li, Na, K, Cs and Ca are 4, 4, 6, 8 and 6, respectively.

There are many experimental difficulties associated with working with metal ammonia solutions and certain steps must be made to ensure their stability. The decomposition reaction of metal ammonia solutions is a chemical equilibria present within the system at all times resulting in the production of the associated metal amide and hydrogen gas, as given in equation 8.3.

$$M^+ + e^- + NH_3 \rightleftharpoons MNH_2 + \frac{1}{2}H_2 \tag{8.3}$$

This equilibria can be pushed to either the right or the left by promoting certain reaction conditions. By lowering the temperature the preference for decomposition is lessened [126], whilst contamination will encourage the decomposition. Contaminant species may be introduced by unclean glasswear as well as unclean reagents. Ammonia of high purity is essential to the production of a stable metal ammonia solution, the accepted cleaning procedure for purification of ammonia uses the property of the metal-ammonia solution to react with and sediment out most contaminants via the decomposition reaction [191]. Storage of the metal

and ammonia in air free conditions is also essential, but is assisted by modern development of high vacuum pump systems and purpose built leak tight stainless steel systems which have superseded Schlenk line alternatives.

Practically the use of metal ammonia solution to intercalate layered materials requires precise control over experimental conditions. However, this demanding technique allows low temperature, controllable intercalation which makes this the technique of preference.

8.2 Probability Density Functions

Probability density functions are used to describe the distribution of a continuous random variable and the probability of the observation of the variable for particular values. The two distributions which will be introduced are the normal distribution and the log-normal distribution. The difference between the two distributions may be understood by the relationship between the independent variables that contribute to the measured variable, in the case of the normal distribution these variables are added and in the case of the log-normal distribution these variables are multiplied.

8.2.1 Normal Distribution

The normal probability density function of continuous random variable, x, is given in equation 8.4 and relates to the arithmetic mean, μ, the standard deviation σ of the data.

$$p(x) = \frac{1}{\sigma\sqrt{2\pi}}\exp[\frac{-(x-\mu)^2}{2\sigma^2}] \tag{8.4}$$

The main features of this function is that it is symmetrical, the mean, mode and median are all equal and the distribution of data on either side of the mean value.

8.2.2 Log-Normal Distribution

The log-normal distribution function is given in equation 8.5. For a continuous random variable, x, which is log-normally distributed, the natural logarithm of the

measured variable, ln(x), will have a normal distribution. It is the mean and standard deviation of underlying normal distribution which μ_* and σ_* within equation 8.5 describe.

$$p(x) = \frac{1}{x\sigma_*\sqrt{2\pi}}\exp[\frac{-(\ln(x) - \mu_*)^2}{2(\sigma_*)^2}] \tag{8.5}$$

The standard deviation, σ, of the log-normally distributed measured variable, x, is related to the variance, V, which is calculated using equation 8.6:

$$V = \sigma^2 = \exp(2\mu_* + (\sigma_*)^2).[\exp((\sigma_*)^2) - 1] \tag{8.6}$$

The mean, μ, of the log-normally distributed measured variable, x, is calculated using equation 8.7

$$\mu = \exp(\mu_* + \frac{(\sigma_*)^2}{2}) \tag{8.7}$$

The geometric mean, which is equal to the median, of the log-normal distribution is given by equation 8.8

$$\mu_g = \exp(\mu_*) \tag{8.8}$$

Whilst the mean of the normal distribution is easy to interpret and serves as an intuitive representation of the data, along with the standard deviation, it is not quite as simple to find two analogous parameters for the log-normal distribution that provide an intuitive representation of the data. This is because the log-normal distribution is skewed, so that the majority of the data is less than the mean value of the distribution.

8.3 Test of Goodness of Fit: Chi-Squared Test

The chi-squared test is a method of determining the goodness of fit. The formula for the χ^2 value is given in 8.9, where the sum is taken over the difference between each empirical data point, n_i, and expected value ,Np_i, divided by the expected value.

$$\chi^2 = \sum \frac{(n_i - Np_i)^2}{Np_i} \tag{8.9}$$

The χ^2 value is then divided by the degree of freedom, υ, to give a goodness of fit. In the case of the normally distributed histogram, the degree of freedom is equal to the number of bins minus the number of fixed degrees of freedom, which is three (N, μ, and σ). The fit is considered good if the χ^2/υ value is equal to 1 and

the fit is considered unacceptable if $\chi^2/\upsilon \gg 1$ or $\chi^2/\upsilon \ll 1$.

Bibliography

[1] R. P. Feynman. There's plenty of room at the bottom. *Caltech Engineering and Science*, 23:22, 1960.

[2] K. S. Novoselov, A. K. Geim, S. V. Morozov, D. Jiang, Y. Zhang, S. V. Dubonos, I. V. Grigorieva, and A. A. Firsov. Electric field effect in atomically thin carbon films. *Science*, 306(5696):666–669, 2004.

[3] A. K. Geim and K. S. Novoselov. The rise of graphene. *Nat Mater*, 6: 183–191, 2007.

[4] L. D. Hicks and M. S. Dresselhaus. Effect of quantum-well structures on the thermoelectric figure of merit. *Phys. Rev. B*, 47:12727–12731, 1993.

[5] F. J. DiSalvo. Thermoelectric cooling and power generation. *Science*, 285: 703–706, 1999.

[6] P. Cullen, K. Cox, M. Bin Subhan, L. Picco, O. Payton, D. Buckley, T. Miller, S. Hodge, N. Skipper, V. Tileli, and C. Howard. Ionic solutions of 2-dimensional materials. *Nature Chemistry*, 9:244, 2017.

[7] C. Silvera Batista, R. Larson, and N. Kotov. Nonadditivity of nanoparticle interactions. *Science*, 350:1242477, 2015.

[8] J. Pu, Y. Yomogida, K. Liu, L. Li, Y. Iwasa, and T. Takenobu. Highly flexible MoS_2 thin-film transistors with ion gel dielectrics. *Nano Letters*, 12:4013–4017, 2012.

[9] F. Withers, H. Yang, L. Britnell, A. Rooney, E. Lewis, A. Felten, C. Woods, V. Romaguera, T. Georgiou, A. Eckmann, Y. Kim, S. Yeates, S. Haigh, A. Geim, K. Novoselov, and C. Casiraghi. Heterostructures produced from nanosheet-based inks. *Nano Letters*, 14:3987–3992, 2014.

[10] P. Miro, M. Audiffred, and T. Heine. An atlas of two-dimensional materials. *Chemical Society Reviews*, 43:6537–6554, 2014.

[11] A. Laursen, S. Kegnaes, S. Dahl, and I. Chorkendorff. Molybdenum sulfides-efficient and viable materials for electro - and photoelectrocatalytic hydrogen evolution. *Energy Environ. Sci.*, 5:5577–5591, 2012.

[12] J. Yang, D. Voiry, S. Ahn, D. Kang, A. Kim, M. Chhowalla, and H. Shin. Two-dimensional hybrid nanosheets of tungsten disulfide and reduced graphene oxide as catalysts for enhanced hydrogen evolution. *Angewandte Chemie International Edition*, 52:13751–13754, 2013.

[13] Z. Sun, S. Liufu, X. Chen, and L. Chen. Controllable synthesis and electrochemical hydrogen storage properties of Bi_2Se_3 architectural structures. *Chemical Communications*, 46:3101–3103, 2010.

[14] F. Withers, O. Del Pozo-Zamudio, A. Mishchenko, A. P. Rooney, A. Gholinia, K. Watanabe, T. Taniguchi, S. J. Haigh, A. K. Geim, A. I. Tartakovskii, and K. S. Novoselov. Light-emitting diodes by band-structure engineering in van der Waals heterostructures. *Nat Mater*, 14:301–306, 2015.

[15] X. Duan, C. Wang, J. Shaw, R. Cheng, Y. Chen, H. Li, X. Wu, Y. Tang, Q. Zhang, A. Pan, J. Jiang, R. Yu, Y. Huang, and X. Duan. Lateral epitaxial growth of two-dimensional layered semiconductor heterojunctions. *Nat Nano*, 9:1024—-1030, 2014.

[16] H. Peng, W. Dang, J. Cao, Y. Chen, D. Wu, W. Zheng, H. Li, Z. Shen, and Z. Liu. Topological insulator nanostructures for near-infrared transparent flexible electrodes. *Nat Chem*, 4:281–286, 2012.

[17] L. E. Bell. Cooling, heating, generating power, and recovering waste heat with thermoelectric systems. *Science*, 321:1457–1461, 2008.

[18] Y. Q. Cao, X. B. Zhao, T. J. Zhu, X. B. Zhang, and J. P. Tu. Syntheses and thermoelectric properties of Bi_2Te_3-Sb_2Te_3 bulk nanocomposites with laminated nanostructure. *Applied Physics Letters*, 92:143106, 2008.

[19] F. Zahid and R. Lake. Thermoelectric properties of Bi_2Te_3 atomic quintuple thin films. *Applied Physics Letters*, 97:212102, 2010.

[20] J. Maassen and M. Lundstrom. A computational study of the thermoelectric performance of ultrathin Bi_2Te_3 films. *Applied Physics Letters*, 102:093103, 2013.

[21] J. Zhang, H. Liu, L. Cheng, J. Wei, J. Shi, X. Tang, and C. Uher. Enhanced thermoelectric performance of qunituple layer Bi_2Te_3. *Journal of Applied Physics*, 116:023706, 2014.

[22] X. Li, W. Cai, J. An, S. Kim, J. Nah, D. Yang, R. Piner, A. Velamakanni, I. Jung, E. Tutuc, S. Banerjee, L. Colombo, and R. Ruoff. Large-area synthesis of high-quality and uniform graphene films on copper foils. *Science*, 324(5932):1312–1314, 2009.

[23] C. Tusche, H. Meyerheim, and J. Kirschner. Observation of depolarized ZnO(0001) monolayers: Formation of unreconstructed planar sheets. *Physical Review Letters*, 99:026102, 2007.

[24] S. Xu, Di. Li, and P. Wu. One-pot, facile, and versatile synthesis of monolayer MoS_2/WS_2 quantum dots as bioimaging probes and efficient electrocatalysts for hydrogen evolution reaction. *Advanced Functional Materials*, 25:1127–1136, 2015.

[25] M. Choucair, P. Thordarson, and J. Stride. Gram-scale production of graphene based on solvothermal synthesis and sonication. *Nat Nano*, 4: 30–33, 2009.

[26] A. Shmeliov, M. Shannon, P. Wang, J. Kim, A. Okunishi, P. Nellist, K. Dolui, S. Sanvito, and V. Nicolosi. Unusual stacking variations in liquid-phase exfoliated transition metal dichalcogenides. *ACS Nano*, 8:3690–3699, 2014.

[27] K. Paton et al. Scalable production of large quantities of defect-free few-layer graphene by shear exfoliation in liquids. *Nat Mater*, 13:624–630, 2014.

[28] E. Varrla, C. Backes, K. Paton, A. Harvey, Z. Gholamvand, J. McCauley, and J. Coleman. Large-scale production of size-controlled MoS_2 nanosheets by shear exfoliation. *Chemistry of Materials*, 27:1129–1139, 2015.

[29] D. Dreyer, S. Park, C. Bielawski, and R. Ruoff. The chemistry of graphene oxide. *Chem. Soc. Rev.*, 39:228–240, 2010.

[30] G. Guan, s. Zhang, S. Liu, Y. Cai, M. Low, C. Teng, I. Phang, Y. Cheng, K. Duei, B. Srinivasan, Y. Zheng, Y. Zhang, and M. Han. Protein induces layer-by-layer exfoliation of transition metal dichalcogenides. *Journal of the American Chemical Society*, 137:6152—6155, 2015.

[31] M. Lotya, Y. Hernandez, P. King, R. Smith, V. Nicolosi, L. Karlsson, F. Blighe, S. De, Z. Wang, I. McGovern, G. Duesberg, and J. Coleman. Liquid phase production of graphene by exfoliation of graphite in surfactant/water solutions. *Journal of the American Chemical Society*, 131:3611–3620, 2009.

[32] Y. Liang and M. Hersam. Highly concentrated graphene solutions via polymer enhanced solvent exfoliation and iterative solvent exchange. *Journal of the American Chemical Society*, 132:17661–17663, 2010.

[33] S. B. Hendricks. Lattice structure of clay minerals and some properties of clays. *The Journal of Geology*, 50:276–290, 1942.

[34] R. Ma and T. Sasaki. Nanosheets of oxides and hydroxides: Ultimate 2d chargebearing functional crystallites. *Advanced Materials*, 22:5082–5104, 2010.

[35] D. Arivuoli, F. D. Gnanam, and P. Ramasamy. Growth and microhardness studies of chalcogneides of arsenic, antimony and bismuth. *Journal of Materials Science Letters*, 7:711–713, 1988.

[36] N. W. Tideswell, F. H. Kruse, and J. D. McCullough. The crystal structure of antimony selenide, Sb_2Se_3. *Acta Crystallographica*, 10:99–102, 1957.

[37] J. Grigas, E. Talik, and V. Lazauskas. X-ray photoelectron spectra and electronic structure of Bi_2S_3 crystals. *physica status solidi (b)*, 232:220–230, 2002.

[38] D. Teweldebrhan, V. Goyal, and A. Balandin. Exfoliation and characterization of bismuth telluride atomic quintuples and quasi-two-dimensional crystals. *Nano Letters*, 10(4):1209–1218, 2010.

[39] T. L. Anderson and H. B. Krause. Refinement of the Sb_2Te_3 and Sb_2Te_2se structures and their relationship to nonstoichiometric $Sb_2Te_{3-y}Se_y$ compounds. *Acta Crystallographica Section B*, 30:1307–1310, 1974.

[40] R. Sehr and L. Testardi. The optical properties of p-type Bi_2Te_3 Sb_2Te_3 alloys between 2–15 microns. *Journal of Physics and Chemistry of Solids*, 23:1219–1224, 1962.

[41] J. Black, E. M. Conwell, L. Seigle, and C. W. Spencer. Electrical and optical properties of some $M_2^{vb}N_3^{vib}$ semiconductors. *Journal of Physics and Chemistry of Solids*, 2:240–251, 1957.

[42] M. H. Francombe. Structure-cell data and expansion coefficients of bismuth telluride. *British Journal of Applied Physics*, 9:415, 1958.

[43] H. Goldsmid, A. Sheard, and D. Wright. The performance of bismuth telluride thermojunctions. *British Journal of Applied Physics*, 9:365, 1958.

[44] Z. Ding, S. Bux, D. King, F. Chang, T. Chen, S. Huang, and R. Kaner. Lithium intercalation and exfoliation of layered bismuth selenide and bismuth telluride. *Journal of Materials Chemistry*, 19:2588–2592, 2009.

[45] W. Zhang, R. Yu, H. Zhang, X. Dai, and Z. Fang. First-principles studies of the three-dimensional strong topological insulators Bi_2Te_3, Bi_2Se_3 and Sb_2Te_3. *New Journal of Physics*, 12:065013, 2010.

[46] M. Z. Hasan and C. L. Kane. *Colloquium* : Topological insulators. *Rev. Mod. Phys.*, 82:3045–3067, 2010.

[47] A. R. Akhmerov, J. Nilsson, and C. W. J. Beenakker. Electrically detected interferometry of majorana fermions in a topological insulator. *Physical Review Letters*, 102:216404, 2009.

[48] D. A. Wright. Thermoelectric properties of bismuth telluride and its alloys. *Nature*, 181:834, 1958.

[49] G. J. Snyder. Small thermoelectric generators. *Electrochemical Society Interface*, 17:54–56, 2008.

[50] M. Gupta, M. Sayer, Mukhopadhyay S., and S. Kumar. Ultrathin thermoelectric devices for on-chip peltier cooling. *IEEE Transactions on Components, Packaging and Manufacturing Technology*, 1:1395–1405, 2011.

[51] W. Xie, X. Tang, Y. Yan, Q. Zhang, and T. M. Tritt. High thermoelectric performance BiSbTe alloy with unique low-dimensional structure. *Journal of Applied Physics*, 105:113713, 2009.

[52] C. Chiritescu1, C. Mortensen, D. G. Cahill, D. Johnson, and P. Zschack. Lower limit to the lattice thermal conductivity of nanostructured Bi_2Te_3-based materials. *Journal of Applied Physics*, 106:073503, 2009.

[53] R. Yang, G. Chen, and M. Dresselhaus. Thermal conductivity of simple and tubular nanowire composites in the longitudinal direction. *Physical Review B*, 72:125418, 2005.

[54] D. A. Broido and N. Mingo. Theory of the thermoelectric power factor in nanowire-composite matrix structures. *Physical Review B*, 74:195325, 2006.

[55] Y. Min, J. W. Roh, H. Yang, M. Park, S. I. Kim, S. Hwang, S. M. Lee, K. H. Lee, and U. Jeong. Surfactant-free scalable synthesis of Bi_2Te_3 and Bi_2Se_3 nanoflakes and enhanced thermoelectric properties of their nanocomposites. *Adv. Mater.*, 25:1425—-1429, 2013.

[56] J. S. Son, M. K. Choi, M. Han, K. Park, J. Kim, S. J. Lim, M. Oh, Y. Kuk, C. Park, S. Kim, and T. Hyeon. n-type nanostructured thermoelectric materials prepared from chemically synthesized ultrathin Bi_2Te_3 nanoplates. *Nano Lett.*, 12:640—-647, 2012.

[57] D. A. Wright. Nanograined thermoelectric $Bi_2Te_{2.7}Se_{0.3}$ with ultralow phonon transport prepared from chemically exfoliated nanoplatelets. *J. Mater. Chem. A*, 1:12791–12796, 2013.

[58] S. Li, C. Xin, X. Liu, Y. Feng, Y. Liu, J. Zheng, F. Liu, Q. Huang, Y. Qiu, J. He, J. Luo, and F. Pan. 2d hetero-nanosheets to enable ultralow thermal conductivity by all scale phonon scattering for highly thermoelectric performance. *Nano Energy*, 30:780—-789, 2016.

[59] J. Coleman. Liquid-phase exfoliation of nanotubes and graphene. *Advanced Functional Materials*, 19:3680–3695, 2009.

[60] G. Cunningham, M. Lotya, N. McEvoy, G. Duesberg, Pa. van der Schoot, and J. Coleman. Percolation scaling in composites of exfoliated MoS_2 filled with nanotubes and graphene. *Nanoscale*, 4:6260–6264, 2012.

[61] H. Tsai, J. Schindler, C. Kannewurf, and M. Kanatzidis. Plastic superconducting polymer $NbSe_2$ nanocomposites. *Chemistry of Materials*, 9:875–878, 1997.

[62] D. Finn, M. Lotya, G. Cunningham, J. Smith, D. McCloskey, J. Donegan, and J. Coleman. Inkjet deposition of liquid-exfoliated graphene and MoS_2 nanosheets for printed device applications. *J. Mater. Chem. C*, 2:925–932, 2014.

[63] F. Torrisi, T. Hasan, W. Wu, Z. Sun, A. Lombardo, T. Kulmala, G. Hsieh, S. Jung, F. Bonaccorso, P. Paul, D. Chu, and A. Ferrari. Inkjet-printed graphene electronics. *ACS Nano*, 6:2992–3006, 2012.

[64] C. Backes, B. Szydłowska, A. Harvey, S. Yuan, V. Vega-Mayoral, B. Davies, P. Zhao, D. Hanlon, E. Santos, M. Katsnelson, W. Blau, C. Gadermaier, and J. Coleman. Production of highly monolayer enriched dispersions of liquid-exfoliated nanosheets by liquid cascade centrifugation. *American Chemical Society*, 10:1589–1601, 2016.

[65] R. Smith, P. King, M. Lotya, C. Wirtz, U. Khan, S. De, A. O'Neill, G. Duesberg, J. Grunlan, G. Moriarty, J. Chen, J. Wang, A. Minett, V. Nicolosi, and J. Coleman. Large-scale exfoliation of inorganic layered compounds in aqueous surfactant solutions. *Advanced Materials*, 34:3944–3948, 2011.

[66] G. Cunningham, M. Lotya, C. Cucinotta, S. Sanvito, S. Bergin, R. Menzel, M. Shaffer, and J. Coleman. Solvent exfoliation of transition metal dichalcogenides: Dispersibility of exfoliated nanosheets varies only weakly between compounds. *ACS Nano*, 6:3468–3480, 2012.

[67] Y. Hernandez, M. Lotya, D. Rickard, S. Bergin, and J. Coleman. Measurement of multicomponent solubility parameters for graphene facilitates solvent discovery. *Langmuir*, 26:3208–3213, 2010.

[68] U. Khan, A. O'Neill, M. Lotya, S. De, and J. Coleman. High concentration solvent exfoliation of graphene. *Small*, 6:864–871.

[69] W. Hummers and R. Offeman. Preparation of graphitic oxide. *Journal of the American Chemical Society*, 80:1339–1339, 1958.

[70] Y. Si and E. Samulski. Synthesis of water soluble graphene. *Nano Letters*, 8:1679–1682, 2008.

[71] Y. Geng, S. Wang, and J. Kim. Preparation of graphite nanoplatelets and graphene sheets. *Journal of Colloid and Interface Science*, 336:592–598, 2009.

[72] S. Stankovich, D. Dikin, R. Piner, K. Kohlhaas, A. Kleinhammes, Y. Jia, Y. Wu, S. Nguyen, and R. Ruoff. Synthesis of graphene-based nanosheets via chemical reduction of exfoliated graphite oxide. *Carbon*, 45:1558–1565, 2007.

[73] S. Park and R. Ruoff. Chemical methods for the production of graphenes. *Nature Nanotechnology*, 4:217, 2009.

[74] M.S. Dresselhaus. Intercalation in layered materials. *MRS Bulletin*, 12: 24—-28, 1987.

[75] F. A. Lévy. *Intercalated Layered Materials*. Springer Netherlands, 1979.

[76] A. Vijayaraghavan, R. Krishnan, R. Sharma, J. Han, M. Ham, Z. Jin, S. Lin, G. Paulus, N. Reuel, Q. Wang, D. Blankschtein, and M. Strano. Bi- and trilayer graphene solutions. *Nat Nano*, 6:439–445, 2011.

[77] E. Milner, N. Skipper, C. Howard, M. Shaffer, D. Buckley, K. Rahnejat, P. Cullen, R. Heenan, P. Lindner, and R. Schweins. Structure and morphology of charged graphene platelets in solution by small-angle neutron scattering. *Journal of the American Chemical Society*, 134:8302–8305, 2012.

[78] Francis Levy. *Intercalated Layered Materials*. D. Reidel Publishing Company, 1979.

[79] C. Wan, X. Gu, F. Dang, T. Itoh, Y. Wang, H. Sasaki, M. Kondo, K. Koga, K. Yabuki, G. Snyder, R. Yang, and K. Koumoto. Flexible n-type thermoelectric materials by organic intercalation of layered transition metal dichalcogenide TiS_2. *Nat Mater*, 14:622—-627, 2015.

[80] S. Jeong, D. Yoo, M. Ahn, P. Miró, T. Heine, and J. Cheon. Tandem intercalation strategy for single-layer nanosheets as an effective alternative to conventional exfoliation processes. *Nat Commun*, 6:5763, 2015.

[81] R. A. Gordon, D. Yang, E. D. Crozier, D. T. Jiang, and R. F. Frindt. Structures of exfoliated single layers of WS_2, MoS_2, and $MoSe_2$ in aqueous suspension. *J Physical Review B*, 65:125407, 2002.

[82] R. B. Somoano, V. Hadek, and A. Rembaum. Alkali metal intercalates of molybdenum disulfide. *The Journal of Chemical Physics*, 58:697–701, 1973.

[83] X. Fan, P. Xu, D. Zhou, Y. Sun, Y. C. Li, M. Nguyen, M. Terrones, and T. Mallouk. Fast and efficient preparation of exfoliated 2H MoS_2 nanosheets by sonication-assisted lithium intercalation and infrared laser-induced 1T to 2H phase reversion. *Nano Letters*, 15:5956–5960, 2015.

[84] G. Eda, H. Yamaguchi, D. Voiry, Ta. Fujita, M. Chen, and M. Chhowalla. Photoluminescence from chemically exfoliated MoS_2. *Nano Letters*, 11: 5111–5116, 2011.

[85] D. Murphy, F. Di Salvo, G. Hull, and J. Waszczak. Convenient preparation and physical properties of lithium intercalation compounds of group 4B and 5B layered transition metal dichalcogenides. *Inorganic Chemistry*, 15:17–21, 1976.

[86] J. Morales, J. Santos, and J. L. Tirado. Electrochemical studies of lithium and sodium intercalation in $MoSe_2$. *Solid State Ionics*, 83:57–64, 1996.

[87] K. Kwon, S. Lee, K. Park, D. Seo, J. Lee, B. Kong, K. Kang, and S. Jeon. Simple preparation of high-quality graphene flakes without oxidation using potassium salts. *Small*, 7:864–868, 2011.

[88] J. Zheng, H. Zhang, S. Dong, Y. Liu, C. Nai, H. Shin, H. Jeong, B. Liu, and K. Loh. High yield exfoliation of two-dimensional chalcogenides using sodium naphthalenide. *Nat Commun*, 5:2995, 2014.

[89] A. Pénicaud and C. Drummond. Deconstructing graphite: Graphenide solutions. *Accounts of Chemical Research*, 46:129–137, 2013.

[90] C. Vallés, C. Drummond, H. Saadaoui, C. Furtado, M. He, O. Roubeau, L. Ortolani, M. Monthioux, and A. Pénicaud. Solutions of negatively charged graphene sheets and ribbons. *Journal of the American Chemical Society*, 130:15802–15804, 2008.

[91] A. Catheline, C. Vallés, C. Drummond, L. Ortolani, V. Morandi, M. Marcaccio, M. Iurlo, F. Paolucci, and A. Pénicaud. Graphene solutions. *Chemical Communications*, 47:5470–5472, 2011.

[92] P. Ge and M. Fouletier. Electrochemical intercalation of sodium in graphite. *Solid State Ionics*, 28-30:1172–1175, 1988.

[93] T. Enoki, M. Suzuki, and M. Endo. *Graphite Intercalation Compounds and Applications*. Oxford University Press, 2003.

[94] T. Weller, M. Ellerby, S. Saxena, R. Smith, and N. Skipper. Superconductivity in the intercalated graphite compounds C_6Yb and C_6Ca. *Nature Physics*, 1:39, 2005.

[95] K. Fredenhagen and G Cadenbach. Die bindung von kalium durch kohlenstoff. *Zeitschrift für anorganische und allgemeine Chemie*, 158:249, 1926.

[96] M. S. Dresselhaus and G. Dresselhaus. Intercalation compounds of graphite. *Advances in Physics*, 30:139, 1981.

[97] S. A. Solin and H. Zabel. The physics of ternary graphite intercalation compounds. *Advances in Physics*, 37:87–254, 1988.

[98] M. Stanley Whittingham. Chemistry of intercalation compounds: Metal guests in chalcogenide hosts. *Progress in Solid State Chemistry*, 12:41–99, 1978.

[99] C. Julien, E. Hatzikraniotis, K. M. Paraskevopoulos, A. Chevy, and M. Balkanski. Electrical and optical properties of lithium intercalated III–VI compounds. *Solid State Ionics*, 18 19:859–864, 1986.

[100] B. Silbernagel and M. Whittingham. An nmr study of the alkali metal intercalation phase Li_xTiS_2: Relation to structure, thermodynamics, and ionicity. *The Journal of Chemical Physics*, 64:3670–3673, 1976.

[101] M. Stanley Whittingham. Lithium batteries and cathode materials. *Chemical Reviews*, 104:4271–4302, 2004.

[102] Tjipke Hibma. X-ray study of the ordering of the alkali ions in the intercalation compounds Na_xTiS_2 and Li_xTiS_2. *Journal of Solid State Chemistry*, 34: 97–106, 1980.

[103] C. Howard, H. Thompson, J. Wasse, and N. Skipper. Formation of giant solvation shells around fulleride anions in liquid ammonia. *Journal of the American Chemical Society*, 126:13228–13229, 2004.

[104] E. Anglaret, F. Dragin, A. Pénicaud, and R. Martel. Raman studies of solutions of single-wall carbon nanotube salts. *The Journal of Physical Chemistry B*, 110:3949–3954, 2006.

[105] Robert J. Hunter. *Foundations of Colloid Science*. Oxford University Press, Oxford, 2001.

[106] L. Wheeler, N. Kramer, and U. Kortshagen. Thermodynamic driving force in the spontaneous formation of inorganic nanoparticle solutions. *Nano Letters*, 18:1888–1895, 2018.

[107] T. Miller, T. Suter, A. Telford, L. Picco, O. Payton, F. Russell-Pavier, P. Cullen, A. Sella, M. Shaffer, J. Nelson, V. Tileli, P. McMillan, and C. Howard. Single crystal, luminescent carbon nitride nanosheets formed by spontaneous dissolution. *Nano Letters*, 17:5891–5896, 2017.

[108] D. H. Everett. *Basic Principles of Colloid Science*. Royal Society of Chemistry, 1988.

[109] J. Goodwin. *Colloids and Interfaces with Surfactants and Polymers*. Wiley Sons, 2009.

[110] T. Cosgrove. *Colloid Science Principles, Methods and Applications*. Wiley Sons, 2010.

[111] Richard A. L. Jones. *Soft Condensed Matter*. Oxford University Press, 2002.

[112] E. J. W. Verwey. Theory of the stability of lyophobic colloids. *The Journal of Physical and Colloid Chemistry*, 51:631–636, 1947.

[113] P. Debye and E. Hückel. Zur theorie der elektrolyte. i. gefrierpunktserniedrigung und verwandte erscheinungen. *Physikalische Zeitschrift*, 24: 185–206, 1923.

[114] S. Levine and G. P. Dube. Interaction between two hydrophobic colloidal particles, using the approximate Debye-Huckel theory. I. General properties. *Trans. Faraday Soc.*, 35:1125–1140, 1939.

[115] W. Ducker, T. Senden, and R. Pashley. Direct measurement of colloidal forces using an atomic force microscope. *Nature*, 353:239, 1991.

[116] V. Merk, C. Rehbock, F. Becker, U. Hagemann, H. Nienhaus, and S. Barcikowski. In situ non-DLVO stabilization of surfactant-free, plasmonic gold nanoparticles: Effect of Hofmeister's anions. *Langmuir*, 30:4213–4222, 2014.

[117] D. Talapin, E. Shevchenko, C. Murray, A. Titov, and P. Král. Dipole-Dipole interactions in nanoparticle superlattices. *Nano Letters*, 7:1213–1219, 2007.

[118] I. Sogami and N. Ise. On the electrostatic interaction in macroionic solutions. *The Journal of Chemical Physics*, 81:6320–6332, 1984.

[119] D. Grasso, K. Subramaniam, M. Butkus, K. Strevett, and J. Bergendahl. A review of non-DLVO interactions in environmental colloidal systems. *Reviews in Environmental Science and Biotechnology*, 1:17–38, 2002.

[120] J. N. Murrell and A. D. Jenkins. *Properties of Liquids and Solutions*. John Wiley and Sons, 1994.

[121] E. B. Smith. *Basic Chemical Thermodynamics*. Oxford Science Publications, 1990.

[122] John Burgess. *Ions in Solution: Basic Principles of Chemical Interactions*. Horwood, 1999.

[123] M. Mezger, H. Schröder, H. Reichert, S. Schramm, J. Okasinski, S. Schöder, V. Honkimäki, M. Deutsch, B. Ocko, J. Ralston, M. Rohwerder, M. Stratmann, and H. Dosch. Molecular layering of fluorinated ionic liquids at a charged sapphire (0001) surface. *Science*, 322:424–428, 2008.

[124] M. Zobel, R. Neder, and S. Kimber. Universal solvent restructuring induced by colloidal nanoparticles. *Science*, 347:292–294, 2015.

[125] J. Buha, R. Gaspari, A. Del Rio Castillo, F. Bonaccorso, and L. Manna. Thermal stability and anisotropic sublimation of two-dimensional colloidal Bi_2Te_3 and Bi_2Se_3 nanocrystals. *Nano Letters*, 16:4217–4223, 2016.

[126] J. C. Thompson. *Electrons in liquid ammonia*. Clarendon press, Oxford, 1976.

[127] C. Salzmann, B. Murray, and J. Shephard. Extent of stacking disorder in diamond. *Diamond and Related Materials*, 59:69–72, 2015.

[128] Norbert Stribeck. *X-Ray Scattering of Soft Matter*. Springer, 2007.

[129] D. Yamaguchi, N. Miyamoto, S. Koizumi, T. Nakato, and T. Hashimoto. Hierarchical structure of niobate nanosheets in aqueous solution. *Journal of Applied Crystallography*, 40:s101–s105, 2007.

[130] O. Glatter and O. Kratky. *Small Angle X-ray Scattering*. London : Academic Press, 1982.

[131] J. Teixeira. Small-angle scattering by fractal systems. *Journal of Applied Crystallography*, 21:781–785, 1988.

[132] R. A. Pethrick and J. V. Dawkins. *Modern Techniques for Polymer Characterisation*. Wiley and Sons, 1999.

[133] J. N. Coleman and et al. Two-dimensional nanosheets produced by liquid exfoliation of layered materials. *Science*, 331:568–571, 2011.

[134] F. Haguenau, P.W. Hawkes, J.L. Hutchison, B. Satiat–Jeunemaître, G.T. Simon, and D.B. Williams. Key events in the history of electron microscopy. *Microscopy and Microanalysis*, 9:96–138, 2003.

[135] P. D. Nellist, M. F. Chisholm, N. Dellby, O. L. Krivanek, M. F. Murfitt, Z. S. Szilagyi, A. R. Lupini, A. Borisevich, W. H. Sides, and S. J. Pennycook. Direct sub-angstrom imaging of a crystal lattice. *Science*, 305(5691):1741–1741, 2004.

[136] X. Chen, C. Li, and H. Cao. Recent developments of the in situ wet cell technology for transmission electron microscopies. *Nanoscale*, 7:4811–4819, 2015.

[137] K. Liu, C. Wu, Y. Huang, H. Peng, H. Chang, P. Chang, L. Hsu, and T. Yew. Novel microchip for in situ TEM imaging of living organisms and bio-reactions in aqueous conditions. *Lab on a Chip*, 8:1915–1921, 2008.

[138] H. Zheng, R. Smith, Y. Jun, C. Kisielowski, U. Dahmen, and A. Alivisatos. Observation of single colloidal platinum nanocrystal growth trajectories. *Science*, 324:1309–1312, 2009.

[139] K. L. Klein, I. M. Anderson, and N. De Jonge. Transmission electron microscopy with a liquid flow cell. *Journal of Microscopy*, pages 117–123, 2011.

[140] G. Binnig, C. F. Quate, and Ch. Gerber. Atomic force microscope. *Phys. Rev. Lett.*, 56:930–933, 1986.

[141] X. Xie, H. Chung, C. Sow, and A. Wee. Nanoscale materials patterning and engineering by atomic force microscopy nanolithography. *Materials Science and Engineering: R: Reports*, 54:1–48, 2006.

[142] M. N. Berberan-Santos. Beer's law revisited. *Journal of Chemical Education*, 67:757, 1990.

[143] A. O'Neill, U. Khan, and J. Coleman. Preparation of high concentration dispersions of exfoliated MoS_2 with increased flake size. *Chemistry of Materials*, 24:2414–2421, 2012.

[144] C. Backes, R. Smith, N. McEvoy, N. Berner, D. McCloskey, H. Nerl, A. O'Neill, P. King, T. Higgins, D. Hanlon, N. Scheuschner, J. Maultzsch, L. Houben, G. Duesberg, J. Donegan, V. Nicolosi, and J. Coleman. Edge

and confinement effects allow in situ measurement of size and thickness of liquid-exfoliated nanosheets. *Nat Commun*, 5:4576, 2014.

[145] C. Backes, K. Paton, D. Hanlon, S. Yuan, M. Katsnelson, J. Houston, R. Smith, D. McCloskey, J. Donegan, and J. Coleman. Spectroscopic metrics allow in situ measurement of mean size and thickness of liquid-exfoliated few-layer graphene nanosheets. *Nanoscale*, 8:4311–4323, 2016.

[146] S. Fogden, C. Howard, R. Heenan, N. Skipper, and M. Shaffer. Scalable method for the reductive dissolution, purification, and separation of single-walled carbon nanotubes. *ACS Nano*, 6:54–62, 2012.

[147] A. Volykhov, J. Sánchez-Barriga, A. Sirotina, V. Neudachina, A. Frolov, E. Gerber, E. Kataev, B. Senkovsky, N. Khmelevsky, A. Aksenenko, N. Korobova, A. Knop-Gericke, O. Rader, and L. Yashina. Rapid surface oxidation of Sb_2Te_3 as indication for a universal trend in the chemical reactivity of tetradymite topological insulators. *Chemistry of Materials*, 28: 8916–8923, 2016.

[148] V. Atuchin, T. Gavrilova, K. Kokh, N. Kuratieva, N. Pervukhina, and N. Surovtsev. Structural and vibrational properties of PVT grown Bi_2Te_3 microcrystals. *Solid State Communications*, 152:1119–1122, 2012.

[149] Z. Ding, S. Bux, D. King, F. Chang, T. Chen, S. Huang, and R. Kaner. Lithium intercalation and exfoliation of layered bismuth selenide and bismuth telluride. *Journal of Materials Chemistry*, 19:2588–2592, 2009.

[150] M. Han, K. Ahn, H. Kim, J. Rhyee, and S. Kim. Formation of Cu nanoparticles in layered Bi_2Te_3 and their effect on ZT enhancement. *Journal of Materials Chemistry*, 21:11365–11370, 2011.

[151] A. Mansour, W. Wong-Ng, Q. Huang, W. Tang, A. Thompson, and J. Sharp. Structural characterization of Bi_2Te_3 and Sb_2Te_3 as a function of temperature using neutron powder diffraction and extended x-ray absorption fine structure techniques. *Journal of Applied Physics*, 116:083513, 2014.

[152] David W. Scott. On optimal and data-based histograms. *Biometrika*, 66: 605–610, 1979.

[153] K. Kouroupis-Agalou, A. Liscio, E. Treossi, L. Ortolani, V. Morandi, N. Pugno, and V. Palermo. Fragmentation and exfoliation of 2-dimensional materials: a statistical approach. *Nanoscale*, 6:5926–5933, 2014.

[154] H. Yau, M. Bayazit, J. Steinke, and M. Shaffer. Sonochemical degradation of N-methylpyrrolidone and its influence on single walled carbon nanotube dispersion. *Chemical Communications*, 51:16621–16624, 2015.

[155] L. Ren, X. Qi, Y. Liu, G. Hao, Z. Huang, X. Zou, L. Yang, J. Li, and J. Zhong. Large-scale production of ultrathin topological insulator bismuth telluride nanosheets by a hydrothermal intercalation and exfoliation route. *Journal of Materials Chemistry*, 22:4921–4926, 2012.

[156] Z. Zeng, T. Sun, J. Zhu, X. Huang, Z. Yin, G. Lu, Z. Fan, Q. Yan, H. Hng, and H. Zhang. An effective method for the fabrication of few-layer-thick inorganic nanosheets. *Angewandte Chemie International Edition*, 51:9052–9056, 2012.

[157] J. Chen, Y. Zhu, N. Chen, X. Liu, Z. Sun, Z. Huang, F. Kang, Q. Gao, J. Jiang, and L. Chen. Nano-scaled top-down of bismuth chalcogenides based on electrochemical lithium intercalation. *Journal of Nanoparticle Research*, 13:6569–6578, 2011.

[158] W. Rudorff. Inclusion of base metals in graphite and in metallic chalcogenides of the type MeX_2. *Chimia*, 19:489, 1965.

[159] H. Bando, K. Koizumi, Y. Oikawa, K. Daikohara, V. A. Kulbachinskii, and H. Ozaki. The time-dependent process of oxidation of the surface of Bi_2Te_3 studied by x-ray photoelectron spectroscopy. *Journal of Physics: Condensed Matter*, 12:5607, 2000.

[160] P. Arun, P. Tyagi, A. G. Vedeshwar, and V. Kumar Paliwal. Ageing effect of Sb_2Te_3 thin films. *Physica B: Condensed Matter*, 307:105–110, 2001.

[161] L. Ren, X. Qi, Y. Liu, G. Hao, Z. Huang, X. Zou, L. Yang, J. Li, and J. Zhong. Large-scale production of ultrathin topological insulator bismuth telluride nanosheets by a hydrothermal intercalation and exfoliation route. *Journal of Materials Chemistry*, 22:4921–4926, 2012.

[162] G. Bepete, E. Anglaret, L. Ortolani, V. Morandi, K. Huang, A. Pénicaud, and C. Drummond. Surfactant-free single-layer graphene in water. *Nature Chemistry*, 9:347, 2016.

[163] Ge. Bepete, A. Pénicaud, C. Drummond, and E. Anglaret. Raman signatures of single layer graphene dispersed in degassed water, “eau de graphene”. *The Journal of Physical Chemistry C*, 120:28204–28214, 2016.

[164] C. Adenis, V. Langer, and O. Lindqvist. Reinvestigation of the structure of tellurium. *Acta Crystallographica Section C*, 45:941–942, 1989.

[165] Y. Liu, Y. Zhang, S. Ortega, M. Ibáñez, K. Lim, A. Grau-Carbonell, S. Martí-Sánchez, Ka. Ng, J. Arbiol, M. Kovalenko, D. Cadavid, and A. Cabot. Crystallographically textured nanomaterials produced from the liquid phase sintering of $Bi_xSb_{2-x}Te_3$ nanocrystal building blocks. *Nano Letters*, x(0):xx, 2018.

[166] D. Webber, J. Buckley, P. Antunez, and R. Brutchey. Facile dissolution of selenium and tellurium in a thiol-amine solvent mixture under ambient conditions. *Chemical Science*, 5:2498–2502, 2014.

[167] Charles A. Kraus and C. Y. Chiu. The nature of the complexes formed between sodium and tellurium in liquid ammonia. *Journal of the American Chemical Society*, 44:1999–2008, 1922.

[168] A. Cisar and J. Corbett. Synthesis and crystal structure of a salt containing the tritelluride(2-) anion. *Inorganic Chemistry*, 16:632–635, 1977.

[169] Linda D. Schultz. Synthesis and characterization of potassium polytellurides in liquid ammonia solution. *Inorganica Chimica Acta*, 176:271–275, 1990.

[170] D. Thompson and P. Boudjouk. A convenient synthesis of alkali metal selenides and diselenides in tetrahydrofuran and the reactivity differences exhibited by these salts toward organic bromides. effect of ultrasound. *The Journal of Organic Chemistry*, 53:2109–2112, 1988.

[171] P. Kuznetsov, V. Yapaskurt, B. Shchamkhalova, V. Shcherbakov, G. Yakushcheva, V. Luzanov, and V. Jitov. Growth of Bi_2Te_3 films and other phases of Bi-Te system by MOVPE. *Journal of Crystal Growth*, 455:122–128, 2016.

[172] E. Zintl, A. Harder, and B. Dauth. Gitterstruktur der oxyde, sulfide, selenide und telluride des lithiums, natriums und kaliums. *Zeitschrift für Elektrochemie und angewandte physikalische Chemie*, 40:588–593, 1934.

[173] D. Y. Valentine, O. B. Cavin, and H. L. Yakel. On the crystal structure of $LiTe_3$. *Acta Crystallographica Section B*, 33:1389–1396, 1977.

[174] P. Böttcher, J. Getzschmann, and R. Keller. Zur kenntnis der dialkalimetalldichalkogenide Na_2S_2, K_2S_2, Rb_2S_2, Rb_2S_2, K_2Se_2, Rb_2Se_2, K_2Te_2,

K_2Te_2 und Rb_2Te_2. *Zeitschrift für anorganische und allgemeine Chemie*, 619:476–488, 1993.

[175] J. McAfee, J. Andreatta, R. Sevcik, and L. Schultz. Equilibrium among potassium polytellurides in N,N-dimethylformamide solution. *Journal of Molecular Structure*, 1022:68–71, 2012.

[176] G. Basmadjian, G. Parker, R. Magarian, R. Ice, S. Mills, and A. Kirschner. Synthesis of 123mTe-nucleophiles: Potential use in the synthesis of new 123mTe-radiopharmaceuticals. *The International Journal of Applied Radiation and Isotopes*, 31:517–520, 1980.

[177] F. M. Jaeger and J. B. Menke. Über die binären systeme aus tellur und schwefel, und aus tellur und jod. *Zeitschrift für anorganische Chemie*, 75: 241, 1912.

[178] William L. Jolly. *Metal-Ammonia Solutions*. John Wiley Sons, Inc., 2007.

[179] J. Geuchies, C. van Overbeek, W. Evers, B. Goris, A. de Backer, A. Gantapara, F. Rabouw, J. Hilhorst, J. Peters, O. Konovalov, A. Petukhov, M. Dijkstra, L. Siebbeles, S. van Aert, S. Bals, and D. Vanmaekelbergh. In situ study of the formation mechanism of two-dimensional superlattices from PbSe nanocrystals. *Nature Materials*, 15:1248, 2016.

[180] M. Martin, J. Basham, P. Chando, and S. Eah. Charged gold nanoparticles in non-polar solvents: 10-min synthesis and 2d self-assembly. *Langmuir*, 26:7410–7417, 2010.

[181] S. Rohani, S. Horne, and K. Murthy. Control of product quality in batch crystallization of pharmaceuticals and fine chemicals. part 1: design of the crystallization process and the effect of solvent. *Organic Process Research Development*, 9:858–872, 2005.

[182] D. Lide. *CRC handbook of chemistry and physics. 88th ed.* London: CRC, 2007.

[183] I. Harding and T. Healy. Purification of amphoteric polystyrene latex colloids. *Journal of Colloid and Interface Science*, 89:185–201, 1982.

[184] A. Al-kattan, P. Dufour, and C. Drouet. Purification of biomimetic apatite-based hybrid colloids intended for biomedical applications: A dialysis study. *Colloids and Surfaces B: Biointerfaces*, 82:378–384, 2011.

[185] Y. Takagaki, U. Jahn, and M. Ramsteiner. Incorporation of transition metals in the hot-wall-epitaxy growth of Bi_2Te_3 and Sb_2Te_3. *Semiconductor Science and Technology*, 27:085006, 2012.

[186] H. Zhang, H. Wang, Y. Xu, S. Zhuo, Y. Yu, and B. Zhang. Conversion of Sb_2Te_3 hexagonal nanoplates into three-dimensional porous single-crystal-like network-structured Te plates using oxygen and tartaric acid. *Angewandte Chemie International Edition*, 51:1459, 2012.

[187] E. Zurek, P. Edwards, and R. Hoffmann. A molecular perspective on lithium-ammonia solutions. *Angewandte Chemie International Edition*, 48:8198–8232, 2009.

[188] Charles A. Kraus. Solutions of metals in non-metallic solvents; iv.1 material effects accompanying the pasage of an electrical current through solutions of metals in liquid ammonia. migration experiments. *Journal of the American Chemical Society*, 30:1323–1344, 1908.

[189] W. S. Glaunsinger, S. Zolotov, and M. J. Sienko. Magnetic susceptibility of tetraamminelithium(zero) in the range 1.5–194K. *The Journal of Chemical Physics*, 56(10):4756–4768, 1972.

[190] Joshua Jortner. Energy levels of bound electrons in liquid ammonia. *The Journal of Chemical Physics*, 30:839–846, 1959.

[191] R. Dewald and J. Roberts. Conductance of dilute solutions of sodium in liquid ammonia at -33.9, -45, and -65. C. *The Journal of Physical Chemistry*, 72(12):4224–4229, 1968.